Molecular Dynamics Study of Chemical and Physical Behaviors of Nanometer-Thick Liquid Films for Effective Boundary Lubrication

$$\left(\begin{array}{c} \text{有効な境界潤滑のための} \\ \text{ナノ厚さ液体膜の化学的・物理的挙動に関する} \\ \text{分子動力学研究} \end{array} \right)$$

by

Xingyu Chen

Table of Contents

List of Figures

List of Tables

List of Non-Standard Abbreviations

In Chapter 3

    EEA   End group–End group Association (reaction)

    MEA   Main chain–End group Association (reaction)

    MC   Main Chain

    EG   End Group

In Chapter 4

    DS   Double-Site (adsorption)

    SS   Single-Site (adsorption)

    SA   Stably Adsorbed (molecule)

Chapter 1

Introduction

1.1 Background

Of the key technologies for reducing greenhouse gas emissions in order to limit global warming to 1.5 °C, technologies that improve the end-use energy efficiency are expected to have the largest impact of 38% [1,2]. It is estimated that 23% of the total energy in the world is consumed by friction and wear [2]. Tribology is a research field that studies how to reduce friction and wear. When the surfaces of two mechanical parts contact with each other under normal pressure and undergo lateral relative motion by traction force, friction force is generated. To reduce friction force, one effective method is to separate the two contacted surfaces from each other by adding lubricating oils into the contact area. Lubricating oils consist of base oils and additives. Base oils are the main component which are taken from mineral, vegetable, or synthetic oils, and additives are employed to confer specific properties to the base oils, such as friction-reduction, antioxidation, anti-wear, viscosity stability, and so on.
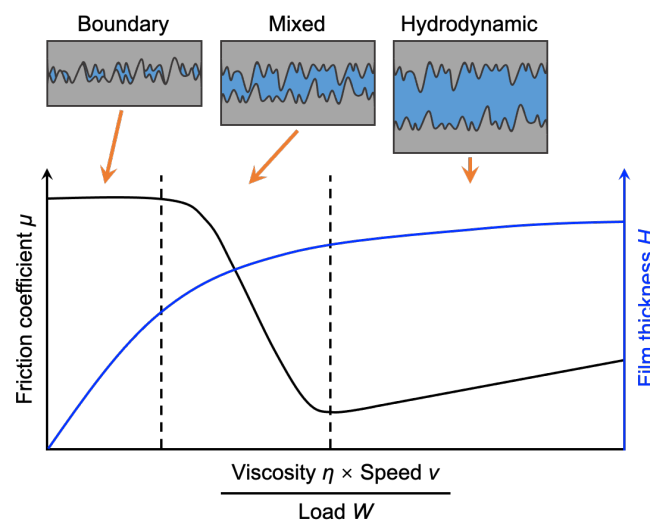
Figure 1-1 Stribeck curve and lubrication regimes.

In oil-based lubricant systems, as illustrated in Figure 1-1 which is known as the Stribeck curve, there are three lubrication regimes, i.e., boundary lubrication regime, mixed lubrication regime, and hydrodynamic lubrication regime. These regimes are determined by the dynamic viscosity of the lubricating oils η, solid–solid relative movement speed v, and applied load W. Friction coefficient μ, defined as the ratio of the lateral force to the normal force, exhibits distinct characteristics in each regime. In the boundary lubrication regime, there is negligible base oils within the contacting area between the two solid surfaces. Some additive molecules in lubricating oils may adsorb on the solid surfaces, forming

boundary films. The applied load is borne by the solid asperities and boundary films. Thus, friction coefficient depends entirely on the properties of the contacted asperities and boundary films, remaining a high value that is independent of η, v, and W. In the mixed lubrication regime, base oils start to enter the solid–solid contact area. The gradually thickening lubricating oil films separate the two solid surfaces, reducing the probability of solid–solid and boundary films contacts. Thus, the load is partially supported by the fluid film and partially by the asperities and boundary films. The friction coefficient decreases as the oil film thickness increases. Finally, in the hydrodynamic lubrication regime, abundant base oils within the contact area generate hydrodynamic films to sufficiently separate the two surfaces, eliminating the contact of any asperities and boundary films. The load is entirely borne by the lubricating oil films, and the friction coefficient increases with $\eta v/W$ because of the increased viscous resistance.

As depicted in Figure 1-1, the friction coefficient in boundary lubrication regime is higher than that in the mixed and hydrodynamic lubrication regimes. Hence, in order to reduce friction, it is essential to design mechanical systems that avoid operating in boundary lubrication regime. However, mechanical systems that involve relative motion across nanoscale gaps have to be operated in the boundary lubrication regime. Examples of such systems encompass hard disk drives (HDDs), nanoimprint lithography (NIL), internal combustion engines (ICEs), and gearboxes. HDDs and NIL are the representative examples of mechanical systems operating at the nanoscale. The nanoscale dimensions of the system restrict the solid–solid gap to the nanometer scale, allowing only for applying nanometer-thick liquid films, thereby leading to the boundary lubrication. ICEs and gearboxes represent mechanical systems operating at the macroscale. However, before startup, there is negligible lubricating oils in the sliding interfaces formed within cylinders and gears, resulting in nanoscale gaps of the sliding interfaces. During startup process, the low relative motion speed and high load impede the entry of lubricating oils into the contact area. Consequently, even with an ample amount of lubricating oils in the mechanical systems, only nanometer-thick liquid films are present in the contact area, resulting in the boundary lubrication. Because boundary lubrication inevitably occurs within nanoscale gaps, to achieve advanced mechanical systems that involve relative motion across nanoscale gaps, it is crucial to establish effective boundary lubrication through nanometer-thick liquid films to reduce friction.

Effective nanometer-thick liquid boundary films require both high stability and high friction-reducing performance. High stability is a prerequisite for the formation of boundary films, encompassing stable adsorption ability and chemical stability. High friction-reducing performance can be dictated by

3

the principle of tribology, which requires boundary films with high load-carrying capacity and low shear strength.

Nevertheless, achieving effective boundary films is challenging due to their extremely thin thickness, typically within a few nanometers, which is greatly influenced by the solid–liquid interactions. Influenced by the salvation force, liquid molecules in the nano-thickness boundary film self-arrange with a layered structure, and strong solid–liquid interactions hinder the flow liquid molecules near the solid surfaces. Thus, the structures and properties of boundary films are different from bulk liquids. Therefore, the lubrication performance of boundary films cannot be adequately described by continuum theory along with bulk properties like density and viscosity. It is essential to develop a comprehensive understanding of the chemical and physical behaviors of nanometer-thick liquid boundary films, as well as their relationship with the chemical structure of the liquid molecules. This understanding, in turn, will enable the optimal design of liquid molecules to achieve effective boundary lubrication.

The following two examples of HDDs and vehicle powertrain systems are presented to illustrate the significance of boundary films and the unresolved challenges associated with them.

1.2 Hard Disk Drives

With the rapid development of digital devices and the Internet, a significant portion of information and data in our daily lives exists, transmits, and processes in digital form. Thus, data storage technology has become particularly crucial. Currently, the data storage devices include HDDs [Figure 1-3(a)], solid-state drives (SSDs), flash drives, and optical disks. Among them, HDDs has significant advantages for the high capacity and low price.

Increasing the capacities of HDDs is an ongoing and perpetual endeavor within the HDDs technology. Currently, HDDs offer a maximum purchasable capacity of approximately 20 TB. HDDs of different capacities are typically applied for distinct purposes, such as low capacities used for personal computers, medium capacities for workstations, and high capacities for large servers. In recent years, the emerging era of artificial intelligence and big data stimulates the need for storage of huge amounts of digital information at low cost. Consequently, it is required to further enhance the data storage density of HDDs. In 2022, Advanced Storage Research Consortium (ASRC) has put forward a technology roadmap that extends to the year 2035 for HDDs (Figure 1-2), aiming to gradually increase the storage
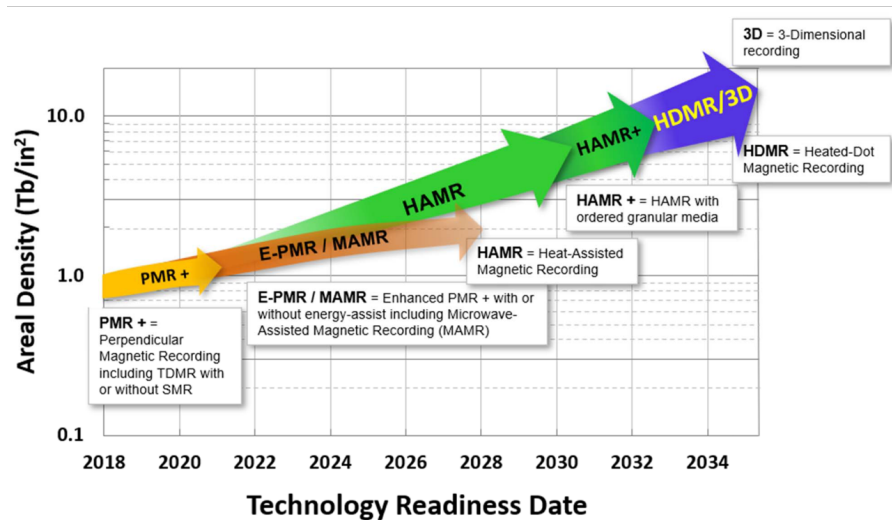
Figure 1-2 Roadmap for new HDD technologies [3]. © 2022 IEEE

density from the current ~1 Tb/in² to over 10 Tb/in² through innovative technologies [3]. These new technologies include microwave assisted magnetic recording (MAMR), heat-assisted magnetic recording (HAMR) [3,4], HAMR with ordered granular media (HAMR+), heated-dot magnetic recording (HDMR), 3-dimensional recording, and so on.

Figure 1-3(a) shows the construction of HDDs. The data are stored on the magnetic disks and written and read by the magnetic head. As shown in Figure 1-3(b), a sequence of magnetic bits is arranged in the magnetic layer on the disk, which is utilized for storing binary data by employing two distinct orientations of the magnetic field. Above the magnetic layer as well as on the surface of head, a carbon overcoat layer, made of diamond-like carbon (DLC), serves as a protective barrier, shielding the surfaces from wear and corrosion. When writing and reading data, the disk rotates at a high-speed reaching up to 50 m/s, and the magnetic head flies over the disk, supported by the pressure generated from air bearing, forming the structure called head–disk interface (HDI). To reduce the friction force within the HDI, as well as protect the disk surface from impacted by the head, a layer of nanometer-
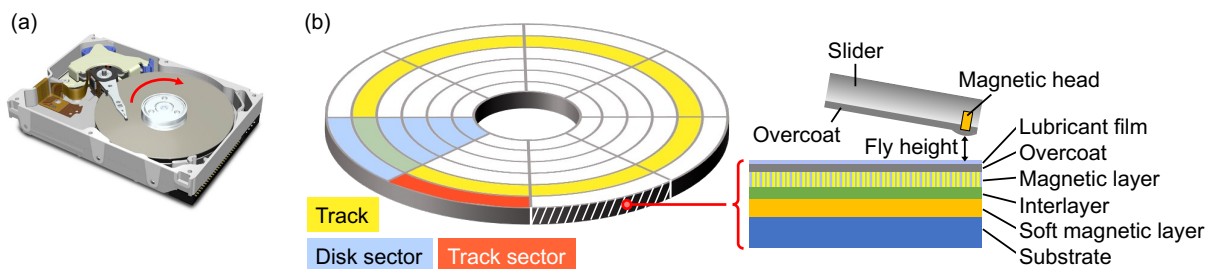
Figure 1-3 (a) Hard disk and (b) the construction of disk and schematic of head–disk interface (HDI).

5

thick lubricating oil film, typically perfluoropolyether (PFPE), is applied on the DLC coating of the disk surface. PFPE molecules have several functional groups that can adsorb onto the DLC. Due to the nanometer thickness of the lubricant films and their lack of flowing ability because of adsorption, PFPEs form boundary films, resulting in the boundary lubrication regime of HDI. To achieve an effective boundary film, high chemical stability is required, because the degradation of the lubricant films can lead to the failure of HDI [5], as explained further below.

To achieve higher data storage density, it is imperative to increase the number of magnetic bits per inch square of the disk [6]. For this purpose, the size of magnetic bits needs to be reduced. However, small magnetic bits present challenges because of weak and unstable magnetic fields. First, the weak magnetic field makes it difficult for the head to detect, thus, the gap of HDI needs to be decreased. To solve this issue, the thickness of PFPE lubricant films is typically restricted to about 1–2 nm [7–9]. And the fly height, which is defined as the clearance between the DLC overcoat of the head and the lubricant surface on the disk, is typically precisely controlled to below 2 nm [10,11]. To realize ultrahigh recoding densities, the flying height should be reduced preferably to zero [8]. However, it will lead to a new problem that intermittent contact sliding between the head and disk occurs inevitably, resulting in confined shear of the PFPE films at shear speeds and shear rates up to 50 m/s and 5×10^{10} s^{-1}. Second, the unstable magnetic fields make the orientations of the magnetic fields susceptible to alter even under room temperatures. Therefore, magnetic media with high coercivity, such as FePt [12,13], are required. But high coercivity makes it challenging to change the orientation of magnetic fields for writing data. HAMR solves this problem by heating the magnetic media above the Curie temperature during data writing process, typically 700–800 K, thereby lowering the coercivity of the media (Figure 1-4).
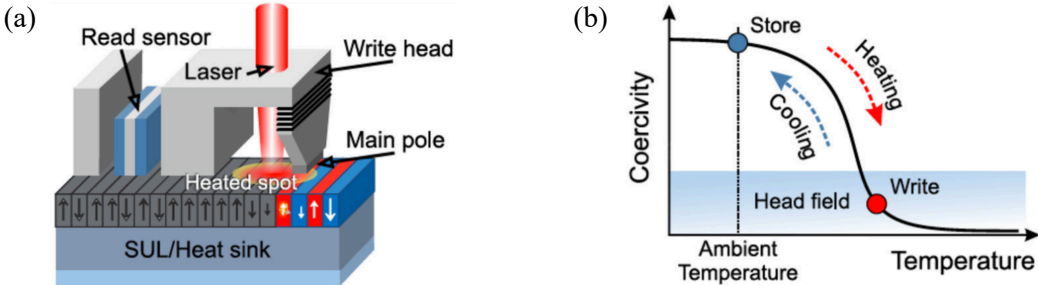
Figure 1-4 (a) Recording image of HAMR and (b) coercivity of FePt media as a function of temperature. Adapted from Ref. [12], with the permission of AIP Publishing.

In HAMR system, such high temperature along with high shear rate make it challenging for ensure the chemical stability of PFPE molecules. The combined impacts of heating and shearing may induce the mechano-chemical decomposition of the PFPEs. Furthermore, the presence of water molecules in the PFPE lubricant films, which cannot be completely removed, could catalyze the reaction of PFPE molecules due to their polarity. Additionally, the DLC overcoat on the disk surface may catalyze the reaction of PFPE molecules. The fragments of PFPE molecules produced by reactions may transfer to the head and become contamination, which is termed as smears in HAMR. Smears may substantially raise the head temperature and affect the media heating process, thereby degrading the long-term reliability and recording performance of HAMR. Hence, in order to achieve effective boundary films in HAMR systems, it is crucial to utilize lubricant molecules with high chemical stability [5,14–17]. To tackle this challenge, the chemical stability of PFPE molecules under HAMR working conditions is needed to be verified, which will facilitate design of lubricant molecules with high chemical stability.

1.3 Vehicle Powertrain Systems

According to the reports from the International Energy Agency (IEA), in 2021, approximately 8% of global direct CO_2 emissions were attributed to cars and vans [18]. In order to achieve the Net Zero Emissions by 2050, it is essential to enhance the energy efficiency of vehicles. Friction is responsible for 33% of the dissipation of fuel energy in fossil-fueled vehicles (FFVs). Within this category, the engine system and transmission system account for 35% and 15% of the total friction, respectively [19]. Thus, it is crucial to reduce the friction force in the vehicle powertrain systems, such as the ICEs in the FFVs, and bearings and gearboxes in any FFVs and electric vehicles (EVs).

As shown in Figure 1-1, in order to reduce friction, low-viscosity lubricating oils are preferred because they lead to low viscous resistance [20–22]. However, at low velocities and high loads, because low-viscosity oils are not able to generate sufficiently high hydrodynamic pressure, the hydrodynamic lubrication regime changes undesirably to the boundary lubrication regime, leading to high friction [23,24]. In order to reducing the friction force by avoiding solid–solid contact, friction modifiers (FMs) are typically added into the base oil, to form a boundary film by adsorbing on the surfaces of the friction pairs (Figure 1-5). FMs include nanoparticles, functionalized polymers, molybdenum disulphide (MoS_2), molybdenum dialkyldithiocarbamate (MoDTC), zinc dialkyldithiophosphates (ZDDP), and so on [20].

They can form physical adsorption or chemical reaction boundary films on solid surfaces to prevent direct solid–solid contact [20,25–31]. For environmental protection, and prevent copper corrosion in the transmission systems of EVs [32], rather than the FMs containing sulfur and phosphorus, organic friction modifiers (OFMs) that are composed only of carbon, hydrogen, oxygen, and nitrogen atoms are essential [20,23,25,33–36].
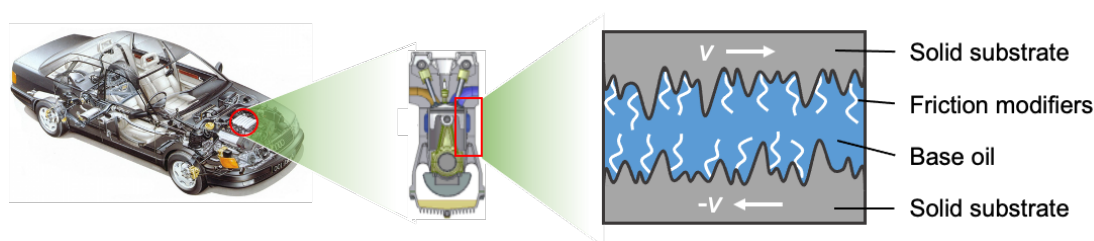
Figure 1-5 Adsorption behavior of friction modifiers in the internal combustion engines.
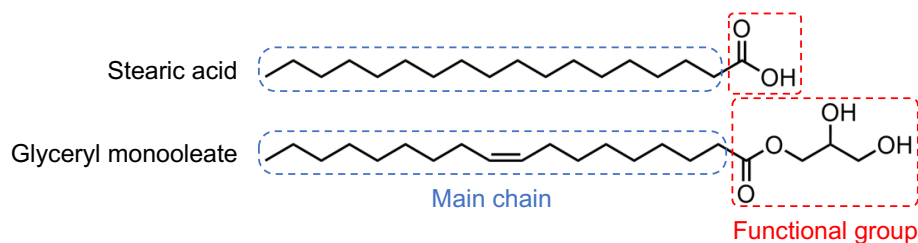
Figure 1-6 Molecular structure for organic friction modifier. Take stearic acid and glyceryl monooleate as examples.

As shown in Figure 1-6, OrFMs are typically amphiphilic molecules with one or more functional groups, such as carboxylate, alcohol, ester, amine, and amide groups, attached to a predominantly linear alkyl chain [20,25,37]. The functional groups adsorb physically and/or chemically onto solid surfaces and the alkyl chains extend into the lubricating oils [20,25,37–42]. It is important to design the molecular structures of OFMs properly because they determine the performance of the boundary films. The requirements for high-performance boundary films and their relationship with OFM molecular properties are explained as follows.

(1) Ability to form boundary films

It is related to the properties of individual OFM molecules. Boundary films formed by the dynamic equilibrium process of adsorption, desorption, and repair behaviors of OFM molecules. To effectively form boundary films, OFM molecules need to own high diffusion ability in the base oils as well as on the solid surfaces. High surface adsorption energy is also important.

(2) High load-carrying capacity

It is related to the properties of the clusters formed by a group of OFM molecules. High load-carrying capacity means the boundary film is difficult to be removed from solid surfaces even under high loads. In general, it requires OFM molecules to form boundary films with high surface density, cohesive and surface adsorption energies.

(3) Low shear strength

It is related to the structure of the boundary films, which can be categorized into two aspects: inner structure of boundary films and inter structure of boundary films–base oils. The former is determined by the inter-molecular interactions between OFM molecules. Forming a multi-layer structure with low shear strength allows for layered sliding, which can reduce the friction force within the boundary films. And the latter is determined by the adsorption status and the conformations of the main chain of OFM molecules. Forming a clear sliding plane at the interface of boundary films–base oils can decrease the shear strength because of less interdigitations between OFM and base oil molecules.

For the conventional OFMs like stearic acid and glycerol monooleate (GMO), experimental studies reveal that they still have limitations in achieving ideal frictional performance of high load-carrying capacity, high wear-reducing effect, and stable friction coefficient over time. In order to improve the frictional performance, it is necessary to design OFM molecules with novel structures that are able to form more effective boundary films.

1.4 Approaches to Study Boundary Films

Both experimental and computer simulations are capable of studying the physical and chemical properties of boundary films.

To measure physical quantities of boundary films, experimental methods such as the fiber wobbling method (FWM), atomic force microscopy (AFM), and pin-on-disk test, can be used. FWM determines the viscoelastic properties of liquid films by moving a vibrating optical fiber across the liquid film through changes in the vibrational state. AFM uses an optical lever to measure the displacement of a probe manipulating the surface, and can measure the force perpendicular to the surface and the force in the scanning direction. Thus, it can be used to evaluate the formation of boundary films. Pin-on-disk test can measure the friction coefficient to evaluate the load-carrying capacity and shear strength of the

boundary films. To study the chemical properties of molecules, pyrolysis-gas chromatography-mass spectrometer (Py-GC/MS) can be used to induce the pyrolysis and thermal oxidative reactions of materials and analyze the products.

The experimental methods, however, face challenges in explaining the relationship between OFM molecular structures and frictional performances of boundary films, as well as directly observing the reaction process under realistic working conditions of HAMR, which is characterized by high temperatures and shear rates. Free of the limitations of experimental methods, computer simulation methods can directly observe the chemical and physical behaviors of molecules and are easily applicable to high temperatures and shear rates.

For computational methods, quantum mechanical (QM) calculations involve solving the Schrödinger equation to obtain the state of system. It can predict molecular configurations, calculate parameters such as energy, polarity, adsorption energy, and determine chemical reaction pathways and derive activation energies. However, the calculations are limited to small systems in terms of time and spatial scales.

In contrast, molecular dynamics (MD) simulations expand the computational capabilities in terms of temporal and spatial scales. In MD simulations, particles that represent atoms and/or molecules are placed within a computational box, and equations of motion of individual particles are formulated. The time evolution of the entire system is described by numerically integrating the equations. The forces acting on the particles are calculated based on their energy interactions, which is known as force field. Force field determines the accuracy of the simulations. Once the calculations are finished, the positions and velocities of individual atoms and molecules can be directly obtained as a function of time. Therefore, MD simulations are particularly useful for analyzing molecular and atomic-scale dynamic phenomena and are selected as the method for this research.

MD simulations can be categorized into non-reactive and reactive simulations. Non-reactive MD simulations do not allow the formation or breakage of covalent bonds. It requires to define the unchangeable molecular topology, such as connections of bonds, angles and dihedrals. Reactive MD simulations allow the formation and breakage of covalent bonds. Compared with density functional theory (DFT), reactive MD simulations can calculate chemical reactions in larger temporal and spatial scales. For example, reactive MD with ReaxFF [43–48] force fields, which is a cost-effective and accurate method providing atomistic-level details of dynamics of systems including chemical reactions,

typically is more than five orders of magnitude less costly than DFT calculations [49]. However, the drawback lies in the limited transferability of the force field, which means that specific materials and reaction pathways often require fitting specific force field parameters. Furthermore, in order to capture the rapidly occurred chemical reactions, the timestep applied in reactive MD simulations is shorter than that used in non-reactive MD simulations, ranging from 0.1 to 0.2 fs, resulting in lower computational efficiency compared to non-reactive MD simulations.

1.5 Objectives and Methods

To propose the guidelines for design molecules that allow for formation of effective nanometer-thick liquid boundary films, it is essential to understand two fundamental aspects. The first is, to identify the vulnerable bonds, and understand the conditions and processes of chemical reactions within the boundary films. The second is, to understand the relationship between the molecular structures, adsorption behaviors, boundary film structures, and friction performance. To achieve these purposes, we employ reactive and non-reactive MD simulations as the primary methods, supplemented by certain QM calculations.

To understand the chemical behaviors of molecules in nanometer-thick liquid boundary films, we take PFPE lubricant films in HAMR as one subject. Reactive MD simulations are used to investigate the reaction rates and pathways for PFPE molecules, at high temperatures and high shear rates, various normal pressures, and with or without water molecules. In order to obtain a high-precision reactive MD force field, QM calculations are used to calculate the energies for bonds and angles of PFPE molecules, and the results are used to fit the parameters for the ReaxFF force field.

To understand the physical behaviors of molecules in nanometer-thick liquid boundary films, we take OFM boundary films in vehicle powertrain systems as another subject. Non-reactive MD simulations are used to investigate the adsorption behaviors of OFM molecules in base oils, confined between two iron oxide surfaces. QM calculations are used to obtain the adsorption energies between OFM molecules–substrate.

1.6 Dissertation Outline

In Chapter 1, the background on boundary lubrication was introduced, specifically focusing on two

applications: HDDs and vehicle powertrain systems. The significance of boundary films and the unresolved challenges, along with the research motivations were presented. MD simulations were chosen as the research method.

In Chapter 2, reactive MD simulations with ReaxFF force field will be applied for investigating the pure thermal and mechano-chemical reactions of PFPE lubricant films. The reaction rates are calculated and then fitted with the Arrhenius equation and stress-assisted Arrhenius equation, for pure thermal reaction and mechano-chemical reaction, separately. The effect of heat and mechanical stress on the decomposition rates are discussed. Different PFPE molecules are used to compare their reaction rate, and the reaction pathways are analyzed to recognize the vulnerable bonds of PFPEs.

In Chapter 3, the effect of water on the mechano-chemical decomposition of PFPE will be further investigated under different normal pressures. Analyzations are thoroughly carried out for the reaction rates, types, pathways, and products, and vulnerable bonds.

In Chapter 4, the adsorption behavior of a newly designed OFM will be investigated to understand the mechanism of its super frictional properties, by using non-reactive MD simulations with COMPASS II force field. Statistic analyzations are used to investigate the film structure and the formation. Dynamic analyzations are carried out to understand the self-repair process of the adsorption film.

Finally, in Chapter 5, the conclusions drawn from the entire body of work will be presented, along with the future work.

Chapter 2

Mechano-Chemical Reactions of Perfluoropolyether Lubricant Films in Heat-Assisted Magnetic Recording: Effects of Mechanical Stress and Heat

2.1 Introduction

As described in Chapter 1, the decomposition of PFPE lubricant films make it challenging to ensure the reliability and durability of the HDI. To understand the chemical stability of PFPE molecule, both experimental studies and MD simulations have been carried out.

In experimental studies, with Fourier transform infrared spectroscopy (FT-IR) or time-of-flight secondary ion mass spectroscopy (TOF-SIMS), the thermal decomposition of PFPEs has been experimentally confirmed to initiate at the polar end groups [50–52], and the dissociation of main chain occurs when the temperature further increases [52]. It was also confirmed that the main chain dissociation is mainly attributed to the break of C–O–C bond [50], which is the weakest bond in the main chain of PFPEs [53,54]. Helmick and Jones measured the thermal decomposition temperatures of bulk nonpolar PFPEs and determined the activation energies with the reaction rate theory [55]. Degradation of PFPE films during contact sliding at room temperature was observed using a high-vacuum environmental tribometer equipped with a mass spectrometer and the results suggested that triboelectrical reaction and mechanical scission could be the dominant mechanism for PFPE decomposition [56–58].

MD simulations have also been used to study properties of PFPE films [54,59–65]. Particularly, PFPE decomposition has been studied by reactive MD simulations. Performing ReaxFF MD simulations, Lotfi et al. studied the decomposition of polar PFPE D-4OH at elevated temperatures on DLC surfaces [65] and in the presence of oxygen, water, and nanoparticles of SiO_2, $FeO(OH)$, and Fe_2O_3 [54]. Their simulation results indicated that the PFPE decomposition is accelerated by DLC, water, and the oxide nanoparticles, whereas the effect of oxygen molecules is less significant.

As studies so far mainly focused on thermal and catalytic decompositions of PFPE lubricants, less is known about mechano-chemical decomposition. In addition, decomposition rates of PFPEs, which are particularly critical for HAMR because the time scale of heating process is ~1 ns [4], are yet to be quantified. Experimental approaches are difficult to access the extreme conditions of high temperature, high shear rate, and short heating time in HAMR. Though high temperature and shear rate are easily achieved in simulations, the heating time is somewhat long for reactive MD simulations. Even with the ReaxFF method, 1-ns simulations are still computationally expensive because a time step as small as

~0.1 fs is typically required for accurate simulation of reaction processes [54,65]. As a compromise, temperatures obviously higher than the actual conditions are usually used to accelerate reactive MD simulations.

In this chapter, aiming to understand mechano-chemical decomposition of PFPE lubricants in HAMR, we develop the ReaxFF force field of PFPEs, which is not available from the published literature, and conduct ReaxFF reactive nonequilibrium MD simulations [66,67] under the operation conditions of HAMR. The time constant of mechano-chemical decomposition is quantified and compared with that of pure thermal decomposition. Although high temperatures are used to accelerate the simulations of pure thermal decomposition, we are able to derive the time constants at the heating temperatures in HAMR by analyzing the simulation results with the reaction rate theory [45,46,68–70]. We also examine the mechano-chemical decomposition pathway of PEPF films and the change in decomposition rate with normal pressure and molecular structure. Specifically, the stress-assisted reaction rate theory [71–74] is applied to analyze the effect of mechanical stress.

2.2 Simulation Method and Details

2.2.1 ReaxFF Reactive Force Field Method

ReaxFF is a reactive force field method based on bond order [43,44], which dictates connectivities of atoms and is calculated from the interatomic distances of all pairs of atoms. Updating the bond order at each time step allows for description of bond breaking and bond forming during MD simulations. In ReaxFF the total energy of a system, E_{system}, is described as [45]

$$E_{\text{system}} = E_{\text{bond}} + E_{\text{over}} + E_{\text{under}} + E_{\text{tor}} + E_{\text{val}} + E_{\text{lp}} + E_{\text{vdw}} + E_{\text{coulomb}} \qquad (2\text{-}1)$$

where E_{bond}, E_{over}, E_{under}, E_{tor}, E_{val}, E_{lp}, E_{vdw}, E_{coulomb} represent bond energy, overcoordination energy penalty, undercoordination stability, torsion angle energy, valence angle energy, lone pair energy, van der Waals energy, and Coulomb energy, respectively.

In contrast to force fields for non-reactive MD, which are basically general-purpose, ReaxFF force field parameters are usually optimized to reproduce reactions of molecules of interest and thus specific

to target molecules [47,75]. After reviewing the published ReaxFF force fields, we confirmed that the ReaxFF force field for Teflon and molecules composed of C, H, and O atoms include most of the parameters for the ReaxFF of PFPE, but parameters for C–O and C–F bonds and O–C–F valence angle need to be added or refined [76]. Therefore, with QM calculations, we first prepared training data regarding the following items.

(1) change of potential energies with C–O and C–F bond lengths and O–C–F valence angle.

(2) dissociation energies of C–O and C–F bonds.

(3) optimized structures and the corresponding energies of PFPEs.

(4) energies of various structural isomers of PFPEs.

Chemical formulas of the PFPEs will be described in Section 2.2.2. Then the optimal force field parameters for the training datasets, which ensure the error defined below [45] within desired level, were obtained using the covariance matrix adaptation evolution strategy.

$$\text{Error} = \sum_{i=1}^{n} \left[\frac{X_{i,\text{TS}} - X_{i,\text{ReaxFF}}}{\sigma_i} \right]^2 \tag{2-2}$$

where n is the total number of the entries of the training sets, $X_{i,\text{TS}}$ and $X_{i,\text{ReaxFF}}$ are the ith training set and the corresponding ReaxFF value, and σ_i is the weighting factor.

The QM calculations were carried out with the Gaussian 16 package [77] using DFT with the B3LYP hybrid functional [78,79] and the 6-31G(d) basis set [80–82]. AMS (Amsterdam Modeling Suite) software [83], which uses a successive one-parameter parabolic extrapolation approach for the parameterization, was used to find the best fit ReaxFF. We performed five individual optimization runs and calculated the error of each run with Eq. (2-2). The force field with the lowest error was used in our reactive MD simulations. As will be presented in Section 2.3.1, the developed ReaxFF force field provides a good representation of the QM calculation results.

2.2.2 Models and Procedures

In our reactive MD simulations, we used four types of PFPE lubricants: polar D-4OH and nonpolar Demnum of the Demnum type and polar Z-tetraol and nonpolar Z of the Fomblin type. Their chemical formulas and molecular weights (Mw) are listed in Table 2-1, comparable to the Mw of PFPE used in

the HDI [84]. Note that, for the ReaxFF parameterization, only D-4OH and Z-tetraol were used and the number of repeat units in the main chain was set to one to reduce the computational cost of expensive DFT calculations.

To focus on the effect of mechanical stress rather than surface catalyst, as a simplified model of the DLC overcoats on the head and disk surfaces in HAMR, we built diamond crystal plates with (001) surface orientation, which feature high thermal stability [85]. The head was modeled as a slab instead of a curved shape because its curvature radius is about 20 mm, which is roughly four orders larger than the lateral dimensions of the contact region [8]. To ensure that the applied shear stress transfers into the lubricant films and to be representative of amorphous surfaces where slip is not expected [86], slip at the liquid–solid interfaces during shear was suppressed by surface roughness generated on the solid surfaces by removing some carbon atoms and passivating dangling bonds with hydrogen atoms [87–89]. These surfaces are similar to hydrogenated tetrahedral amorphous carbon (ta-C:H). To effectively suppress slip and be close to the typical value (0.2 nm) of the arithmetic mean roughness of the head and disk surfaces [90], the peak-to-valley height and period of the surface roughness were set to 0.27 and 1.0 nm in this study.

Table 2-1 Chemical formulas and molecular weights of PFPE lubricants.

Lubricant		Chemical formula	Molecular weight (g/mol)
Polar	D-4OH	$X–O–(CF_2CF_2CF_2O)_9–X$	1820
		$X = CF_2CH_2OCH_2CH(OH)CH_2OH$	
	Z-tetraol	$X–O–(CF_2CF_2O)_8–(CF_2O)_8–X$	1782
		$X = CF_2CH_2OCH_2CH(OH)CH_2OH$	
Nonpolar	Demnum	$X–O–(CF_2CF_2CF_2O)_9–X$	1848
		$X = CF_2CF_2CF_3$	
	Z	$X–O–(CF_2CF_2O)_9–(CF_2O)_9–X$	1792
		$X = CF_3$	

To separate the effects of temperature, normal pressure, and shear force on lubricant decomposition, we carried out three types of reactive MD simulations and monitored the progress of decomposition with time. One is for bulk PFPE subjected to heating, the second is for PFPE films coated on the disk

subjected to heating and impacting from the head under a constant normal pressure, and the third is for PFPE films coated on the disk subjected to heating and shearing by the head under a constant normal pressure and shear speed. These are simply referred to as heating, impacting, and shearing simulations, respectively. Only D-4OH, which is actually used in hard disk drives, was used for the heating and impacting simulations, and all of the four types of PFPEs were used for the shearing simulation. As will be described in Sections 2.2.2.1 and 2.2.2.2, the temperature was higher and the pressure was lower in the heating simulation than in the impacting and shearing simulations. These led to more rapid atomic motion in the heating simulations, hence the time step was set to 0.1 fs for the heating simulations and 0.2 fs for the impacting and shearing simulations. It should be noted that, to save computational time, initial configurations for the reactive MD simulations were equilibrated by non-reactive MD simulations employing the COMPASS (condensed-phase optimized molecular potentials for atomistic simulation studies) II force field [91]. We confirmed, for the heating simulation at 2500 K, that the results obtained from the initial configurations equilibrated with the COMPASS II and developed ReaxFF are consistent within the error margin (Figure 2-5). All of the MD simulations in this study were conducted using LAMMPS (Large-scale Atomic/Molecular Massively Parallel Simulator) [92]. Other details of the three types of reactive MD simulations are described below.

2.2.2.1 Heating Simulation

The initial configurations of the heating simulations consisted of 36 D-4OH molecules inside a cubic box with periodic boundaries in the x, y, and z directions, as shown in Figure 2-1. The system was heated to a target temperature in 4 ps and then fixed at the temperature for 100 ps. To accelerate lubrication decomposition and thus reduce the computational time, the target temperature was set from 2000 to 2500 K with an interval of 100 K, much higher than expected in HAMR. The pressure of the system was fixed at 0.1 MPa. The Nosé-Hoover thermostat and barostat were used for the temperature and pressure control [93,94]. To reduce statistical uncertainty, for each temperature, simulations were run with 10 different initial configurations and the results were averaged.
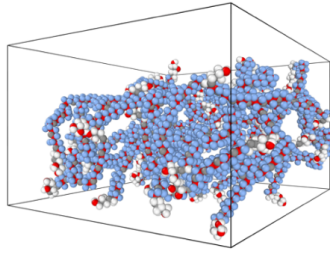
Figure 2-1 One initial configuration of the heating simulations. The system consisted of 36 D-4OH molecules. The gray, white, blue, and red represent carbon, hydrogen, fluorine, and oxygen atoms, respectively.

2.2.2.2 Impacting and Shearing Simulations

The initial configurations of the impacting and shearing simulations were similar and one is shown in Figure 2-2. Lubricant films consisting of 40 PFPE molecules were deposited on the disk located at the bottom of a simulation box, which had dimensions of 8.04624 nm and periodic boundaries in the x and y directions, and the head was set above the PFPE films. Non-periodic boundary condition was applied in the z direction. The film thickness, which was defined as the distance between the mean surfaces of the disk and PFPE film, was 1.34 nm. The distance between the mean surfaces of the head and disk was set to 1.70 nm in the impacting simulation so that the head did not contact with the PFPE films initially. In the shearing simulations, to exclude the decomposition induced by collision of the head with the PFPE films as in the impacting simulation, the head–disk distance was set to 1.55 nm so that the head contacted with the PFPE films initially.
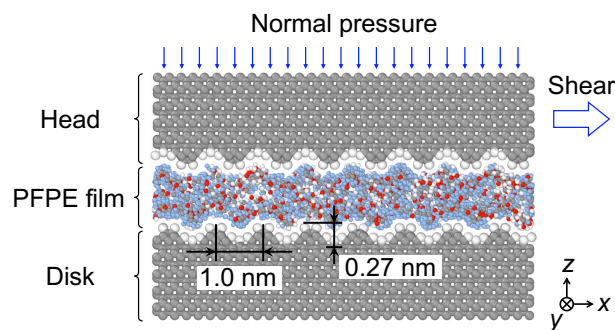
Figure 2-2 One initial configuration of the shearing simulations. Surface roughness with a peak-to-valley height of 0.27 nm and a period of 1.0 nm was introduced to suppress interfacial slip. The x and y dimensions of the simulation box were both set to 8.04624 nm, and periodic boundary conditions were applied in the two directions. The gray, white, blue, and red represent carbon, hydrogen, fluorine, and oxygen atoms, respectively.

Both in the impacting and shearing reactive MD simulations, the systems were heated to a target temperature in 4 ps and then fixed at the temperature. To ensure temperature rise in the PFPE films, the Nosé-Hoover thermostat was coupled to the head, films, and disk in the initial 4 ps. After that, the thermostat was removed from the films and interfacial layers (consisting of hydrogen atoms and their bonded carbon atoms) of the head and disk to avoid its unphysical influence on the dynamics of the films [95–98]. A constant normal pressure was applied to the head by applying a constant force in the $-z$ direction to the carbon atoms in the upmost layer of the head throughout the simulations. In the shearing simulations, in addition to the constant normal pressure, a constant shear speed of 50 m/s in the x direction was applied to the head from 4 ps to the end of simulations. To reproduce the operation conditions in HAMR, we set the target temperature and normal pressure to 700 K and 0.1 GPa. At the relatively low temperature and normal pressure, PFPE molecules decomposed slowly and therefore we performed the impacting and shearing simulations for a long time of 1 ns. Constrained by the extremely high computational cost, each simulation was run only one time. To examine the effect of normal pressure on mechano-chemical decomposition, we also varied the normal pressure from 0.5 to 9.8 GPa in the shearing simulations. For each of these relatively high normal pressures, simulations were run with 10 different initial configurations for 200 ps and the results were averaged to reduce statistical uncertainty.

2.2.3 Calculation Method for Bulk Density

To verify the non-bonded parameters of the developed ReaxFF force field, we calculated the bulk density for the D-4OH. The bulk system consisted of nine D-4OH molecules inside a cubic box with periodic boundaries in the x, y, and z directions. The Nosé-Hoover thermostat and barostat were applied to the system, fixing the temperature and pressure at 293 K and 0.1 MPa. The time step was set to 0.1 fs.

2.3 Results and Discussion

2.3.1 Validation of PFPE ReaxFF

Figure 2-3 compares the energies of C–O and C–F bonds and O–C–F valence angle calculated by

QM and our developed PFPE ReaxFF. Good agreement is obtained, particularly for the bond dissociation energies and energies in the vicinity of equilibrium. The deviation between the ReaxFF and QM is 1.8 and 0.65 kcal/mol for C–O and C–F bond dissociation energies. The deviation between the ReaxFF and QM averaged over seven data points in the vicinity of equilibrium is 1.3, 2.3, and 0.45 kcal/mol for energies of C–O bond, C–F bond, and O–C–F valence angle. Figure 2-4 shows the bulk density of D-4OH. The bulk density at equilibrium (i.e., the average over 200–250 ps) is 1.76 g/cm^3, favorably comparable to the value of 1.7 g/cm^3 provided by the manufacturer of D-4OH. These results demonstrate that the developed ReaxFF force field is reasonably accurate for reactive MD simulations of PFPEs.
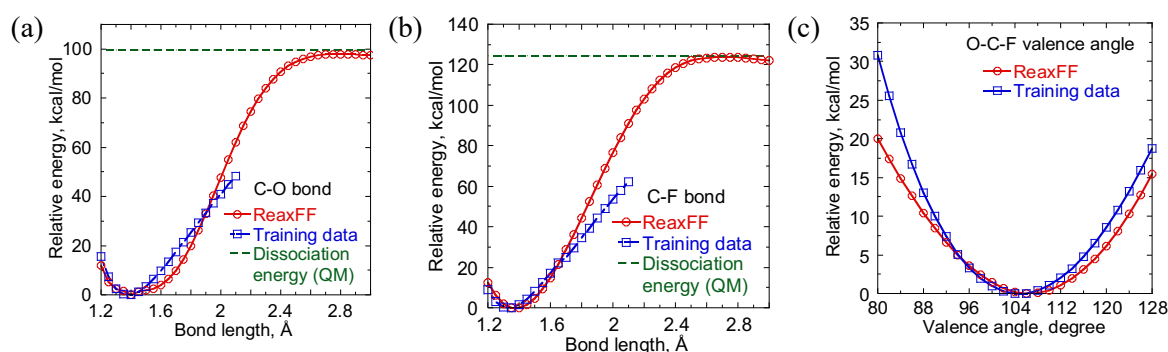
Figure 2-3 Comparison between results of the developed PFPE ReaxFF and training data from QM calculation: (a) C–O bond energy, (b) C–F bond energy, and (c) O–C–F valence angle energy. The bond dissociation energies (broken lines) in (a) and (b) were obtained by QM calculation.
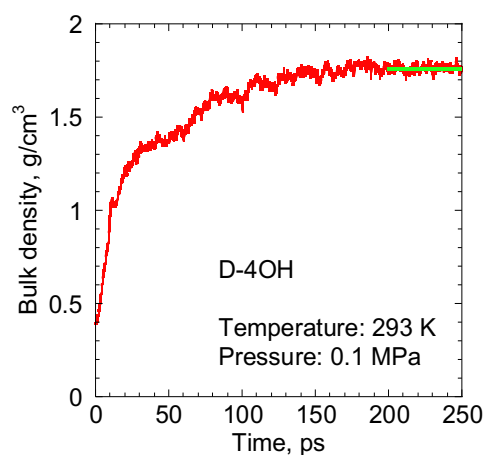
Figure 2-4 Time evolution of the bulk density of D-4OH. The green line indicates the average value over 200–250 ps.

21

2.3.2 Influence of Equilibration of Initial Configurations With/Without the Developed ReaxFF

In this research, initial configurations were not equilibrated with the developed ReaxFF to save computational time. To examine the influence, for the heating simulation of D-4OH at 2500 K, we equilibrated the initial configurations with the developed ReaxFF at 300 K and 0.1 MPa and then performed the simulations following the procedure described in Section 2.2.2.1. The results of five independent simulations are compared with those of ten independent simulations not equilibrated with the developed ReaxFF in Figure 2-5. The decomposition rate constants for the two cases are consistent within the error margin. This demonstrates that equilibration of initial configuration with/without the developed ReaxFF has little influence on the simulation results.
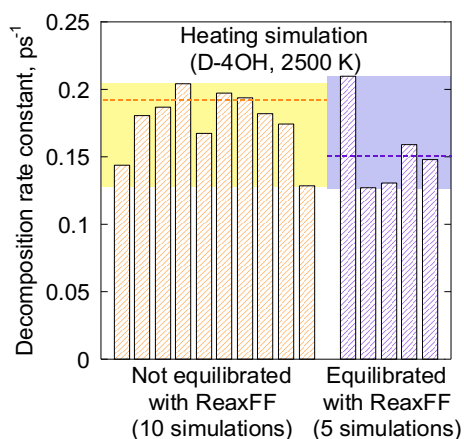
Figure 2-5 Comparison of thermal decomposition rate constants derived from simulations with initial configurations not equilibrated and equilibrated with the developed ReaxFF. The color blocks indicate the range between the maximum and minimum values. The dashed lines indicate the average values.

2.3.3 Comparison of Time Constants of Pure Thermal and Mechano-Chemical Decompositions

Because the heating time in HAMR is in the order of 1 ns, decomposition time constants are a critical criterion for lubricant selection and design. Hence, we compared the time constants of pure thermal and mechano-chemical decompositions of D-4OH under the operation conditions of HAMR by analyzing the results of the heating, impacting, and shearing simulations.

2.3.3.1 Pure Thermal Decomposition

To quantify the time constants of pure thermal decomposition of PFPE at arbitrary temperatures, we analyzed the results of the heating simulations using the Arrhenius model. First, we derived the decomposition rate constant k at each temperature by recording the number of intact PFPE molecules as a function of time, N_t, and fitting it with [46]

$$\ln(N_t/N_0) = -kt \tag{2-3}$$

where t is time and N_0 is the number of intact PFPE molecules at $t = 0$. It should be noted that the first-order kinetics is assumed in Eq. (2-3), which is reasonable for thermal decomposition of covalent compounds [45,46,69,99]. Then we fitted the reaction decomposition rate constants k at different temperatures T with the Arrhenius equation [46,100]

$$\ln k = \ln A - \frac{E_a}{RT} \tag{2-4}$$

where A is a pre-exponential factor, E_a is the activation energy, and R is the ideal gas constant. As a result, we are able to determine the values of A and E_a from the intercept and slope of the fitted line and extrapolate the fitted line to derive decomposition rate constants k at any temperatures of interest. The reciprocal of k is defined as the decomposition time constant.

Figure 2-6(a) shows $\ln(N_t/N_0)$ derived from the heating simulations of D-4OH at different temperatures as a function of time. For each temperature, the number of intact D-4OH molecules N_t was averaged over 10 independent simulations. The straight lines are fits to Eq. (2-3) and the coefficients of determination R^2 are larger than 0.94. This confirms that the thermal decomposition of D-4OH molecules follows the first-order kinetics. It is evident that the decomposition rate constant of D-4OH, which is given by the slopes of the fitted lines, increases with increasing temperature. At temperatures higher than 2200 K, all of the D-4OH molecules decomposed within 100 ps. Figure 2-6(b) shows the Arrhenius plot for the thermal decomposition rates k of D-4OH at different temperatures. The activation energy E_a and pre-exponential factor A were calculated from the fitted straight line and the results are listed in Table 2-2. As we did not find experimental values for D-4OH in the literature,

experimental values for nonpolar Demnum [55], which has identical main chain structure as D-4OH, are listed in Table 2-2 for comparison. The activation energy of D-4OH derived from our simulations is slightly smaller than the experimental values of nonpolar Demnum, which is considered reasonable because, as will be presented in Section 2.3.4.2, our simulation results show that polar D-4OH decomposes more rapidly than nonpolar Demnum. This comparison confirms the validity of our reactive MD simulations with the developed PFPE ReaxFF.
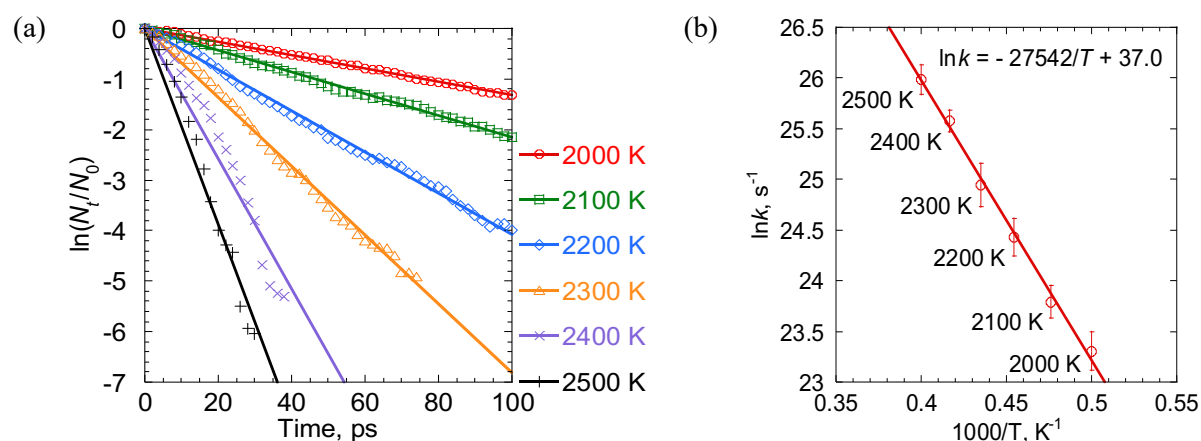
Figure 2-6 (a) Natural logarithms of ratios between the numbers of intact D-4OH at time t and time zero at different temperatures. For each temperature, the results were averaged over 10 independent heating simulations. The straight lines are fits to Eq. (2-3). (b) Arrhenius plot for thermal decomposition of D-4OH. The straight line is fit to Eq.(2-4). The decomposition rate constants k were obtained from the slopes of the fitted lines in (a). Error bar indicates the standard deviation of 10 independent simulations.

Table 2-2 Comparison of fitted Arrhenius parameters with experimental results [55].

	E_a (kcal/mol)	A (Hz)
This work	54.7	1.15×10^{16}
Experiment[a]	55.0–63.1	—

[a] Experimental results are for nonpolar Demnum.

By extrapolating the fitted straight line in Figure 2-6(b), we estimated the reaction rate constants k at 700 and 800 K, which are operation temperatures of HAMR, to be 0.094 and 12.854 s^{-1}, respectively. Then, the time constant for pure thermal decomposition of D-4OH was calculated to be 11 and 0.078 s at 700 and 800 K. These time constants are more than seven orders longer than the heating time of

24

approximately 1 ns in HAMR. Consequently, we conclude that pure thermal decomposition hardly occurs within the heating time of HAMR. Nevertheless, we should emphasize that decreasing the temperature from 800 to 700 K leads to an increase of decomposition time constant by approximately two orders and thus a further significantly lowered risk of lubricant decomposition.

2.3.3.2 Mechano-Chemical Decomposition

Figure 2-7(a) and (b) show the time evolution of the number of intact D-4OH during the 1-ns impacting and shearing simulations, respectively. For the impacting simulation, we confirmed that the head crashed into the D-4OH film at the maximum vertical speed of 32 m/s. Despite the relatively low temperature and normal pressure of 700 K and 0.1 GPa, approximately 23% and 18% molecules decomposed in the 1-ns impacting and shearing simulations, respectively. By fitting the results with Eq. (2-3), the decomposition time constants for the impacting and shearing simulations were calculated to 5 and 10 ns, respectively (Figure 2-8). Because each type of the simulations was run only one time, we suggest that the effects of vertical impact and horizontal shear on decomposition time constants are of similar extent. For comparison, the time constants of pure thermal and mechano-chemical decompositions are summarized in Table 2-3. The time constants of mechano-chemical decomposition are approximately nine orders shorter than that of pure thermal decomposition at 700 K and comparable to the heating time in HAMR. These results indicate the significant influence of mechanical stress on PFPE decomposition. We infer that, under the operation conditions of HAMR, PFPE molecules are highly likely to decompose if subjected to normal impact and/or horizontal shear.
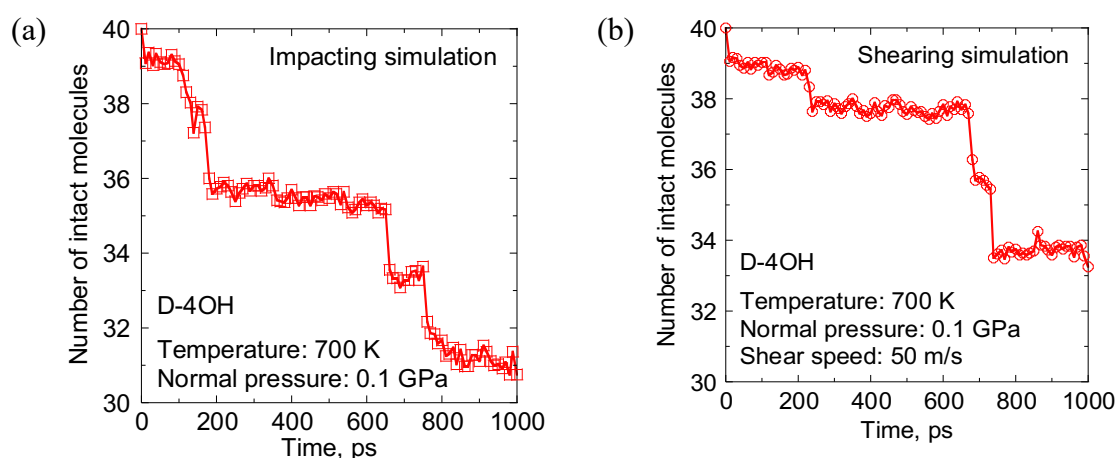
Figure 2-7 Time evolution of the number of intact D-4OH molecules in the (a) 1-ns impacting simulation and (b) 1-ns shearing simulation.
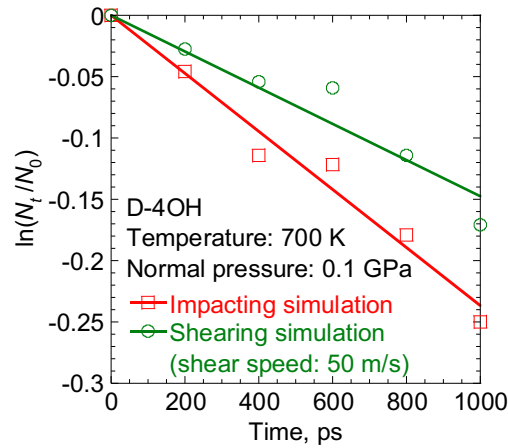
Figure 2-8 Natural logarithms of ratios between the numbers of intact D-4OH at time t and time zero.

Table 2-3 Comparison of time constants of pure thermal and mechano-chemical decompositions.

Conditions	Time constant
Heating (700 K)	11 s
Impacting (700K, 0.1 GPa)	5 ns
Shearing (700 K, 0.1 GPa, 50 m/s)	10 ns

2.3.4 Characteristics of Mechano-Chemical Decomposition

As we confirmed that mechano-chemical decomposition is highly likely to occur rather than pure thermal decomposition in HAMR in the previous section, we will focus on mechano-chemical decomposition of PFPE films and investigate the effects of normal pressure and molecular structure and the reaction pathway in this section. Note that the results presented below were obtained from the shearing simulations, which reflected the realistic situation in HAMR more closely than the impacting simulations.

2.3.4.1 Effect of Normal Pressure

To study the effect of normal pressure on the mechano-chemical decomposition rate of PFPE films, we varied the normal pressure to 0.5, 1.0, 2.0, 3.9, 5.9, 7.8, and 9.8 GPa in the shearing simulations. The decomposition rate constant at each normal pressure was calculated by fitting the time evolution of the number of intact D-4OH molecules during the 200-ps simulations with Eq. (2-3) [Figure 2-9(a)]. The results, together with that of the 1-ns shearing at the normal pressure of 0.1 GPa described in Section

2.3.3.2, are shown in Figure 2-9(b). The decomposition rate constant increases with increasing normal pressure. It is intriguing to note that, at relatively high normal pressures of 3.9–9.8 GPa the change of logarithm of decomposition rate constant with normal pressure can be well fitted by a straight line, whereas data points at 0.1–2.0 GPa lie obviously below the fitted straight line.

To explain these results, we adopt the widely used stress-assisted reaction rate theory, which is extended from the pure thermal Arrhenius theory [68,71–74]. The stress-dependent reaction rate constant k_σ is given by [72]

$$\ln k_\sigma = \ln A - \frac{E_{a\sigma}}{RT} \tag{2-5}$$

Here, $E_{a\sigma}$ is the activation energy in the presence of mechanical stress and is expanded as [70,72,101,102]

$$E_{a\sigma} = E_a - \sigma \Delta V_a \tag{2-6}$$

$$\sigma = \sigma_0 + \mu P \tag{2-7}$$

where E_a is the stress-free activation energy, σ is the shear stress, ΔV_a is the activation volume, P is the external normal pressure, σ_0 is the shear stress at $P = 0$, and μ is a constant and can be assumed to be the same as friction coefficient in the absence of substrate wear [103]. Eq. (2-5) is rewritten by substituting Eqs. (2-6) and (2-7) as

$$\ln k_\sigma = \ln A - \frac{E_a}{RT} + \frac{\sigma_0 \Delta V_a}{RT} + \frac{\mu \Delta V_a}{RT} P \tag{2-8}$$

It should be noted that, in Eqs. (2-6)–(2-8), shear stress rather than normal pressure is supposed to be the component reducing the activation energy.

From Eq. (2-8) and the nonlinear increase of $\ln k_\sigma$ with P in Figure 2-9(b), it can be known that $\mu \Delta V_a$ is not a constant at low normal pressures. To gain insights, we first determined the value of friction coefficient μ by calculating shear stresses at different normal pressures from the simulations. The result is shown in Figure 2-10. Data points are well fitted by Eq. (2-7) with $\sigma_0 = 0$ and $\mu = 0.18$. Because

the slopes of the curve of $\ln k_\sigma$ versus P at different normal pressures are determined by $\frac{\mu \Delta V_a}{RT}$ according to Eq. (2-8), we then calculated the activation volumes ΔV_a from the slopes. As can be seen from Figure 2-11, the activation volume remains nearly constant at high normal pressures of 3.9–9.8 GPa, which is approximately 1.7 % of the volume of the D-4OH molecules. However, below 3.9 GPa the activation volume increases with decreasing normal pressure. The change of activation volume with pressure is consistent with that observed for solid polymeric material [104]. This result suggests caution in extrapolating the linear stress-activated Arrhenius curve obtained at high normal pressures, which could cause significant overestimation of decomposition rate constants at low normal pressures because the activation volume could be no longer a constant in a wide pressure range.
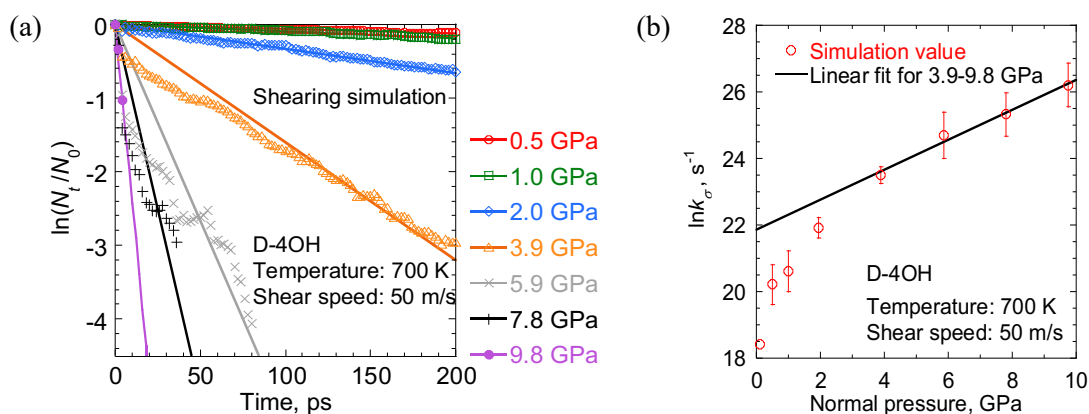
Figure 2-9 (a) Natural logarithms of ratios between the numbers of intact D-4OH at time t and time zero under different normal pressures. The data points are average of 10 independent simulations. (b) Natural logarithm of stress-dependent decomposition rate constant k_σ for D-4OH as a function of normal pressure. Error bar indicates the standard deviation of 10 independent simulations.
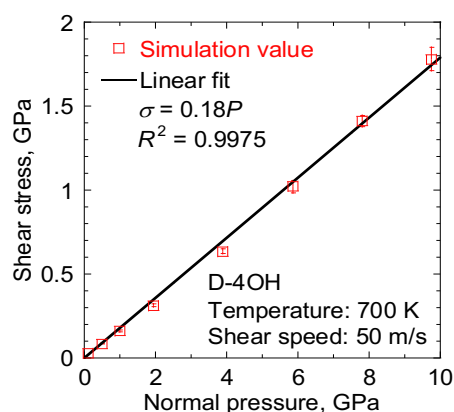
Figure 2-10 Shear stress versus normal pressures for D-4OH. Error bar indicates the standard deviation of 10 independent simulations.
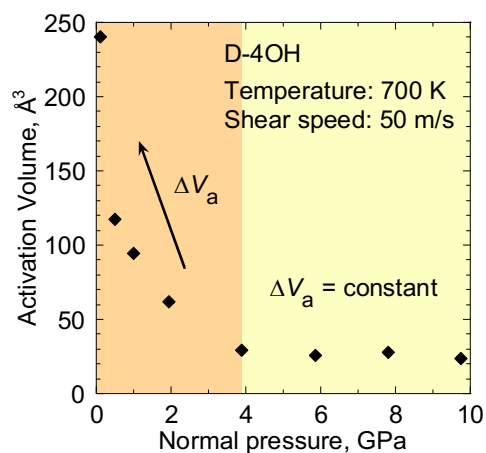
Figure 2-11 Activation volume as a function of normal pressure for D-4OH.

2.3.4.2 Effect of Molecular Structure and Mechano-Chemical Decomposition Pathways

To investigate the effect of molecular structure on the decomposition rate of PFPE films, we performed shearing simulations for Demnum, Z, D-4OH, and Z-tetraol. To reduce the computational time, a relatively high normal pressure of 7.8 GPa was used. Figure 2-12(a) compares the progress of decomposition of the four types of PFPE molecules. The plots of $\ln(N_t/N_0)$ versus time and the linear fits with Eq. (2-3) are shown in Figure 2-12(b). We found that polar D-4OH and Z-tetraol decompose more rapidly than nonpolar Demnum and Z, and the nonpolar Z decomposes more rapidly than the nonpolar Demnum.
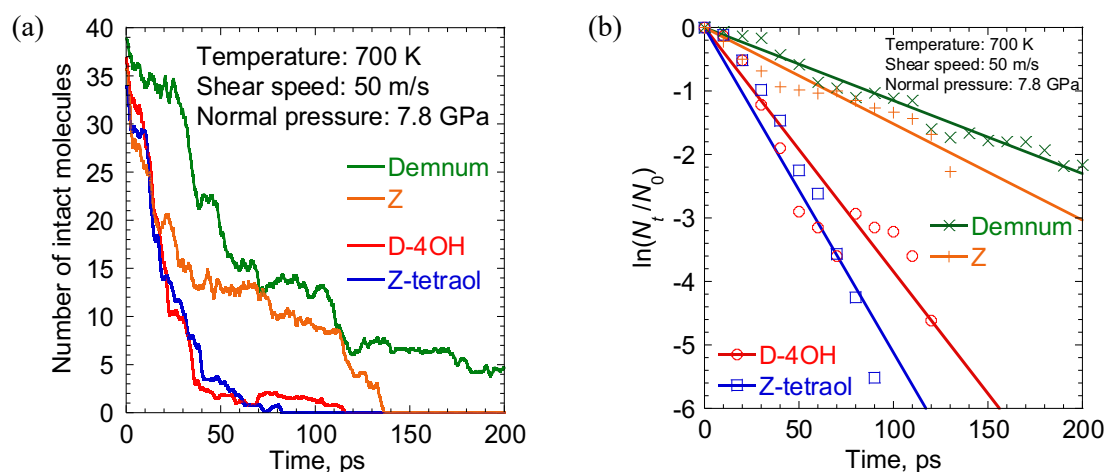
Figure 2-12 (a) Time evolution of the number of intact PFPE molecules in the 200-ps shearing simulations. (b) Natural logarithms of ratios between the numbers of intact PFPE molecules at time t and time zero. Demnum and Z are nonpolar and D-4OH and Z-tetraol are polar molecules.

29

To understand the underlying mechanism of the above results, we analyzed the decomposition pathways by calculating the dissociation ratios for different types of bonds. Here the dissociation ratio for one type of bond is defined as the ratio of the number of dissociated bonds to the total number of that type of bond. Table 2-4 lists the analysis results for Z-tetraol, which exhibits the highest decomposition rate as seen from Figure 2-12(a). Note that, though data are not shown, similar results were obtained for the other three types of PFPEs. The C–OH and ether C–OC bonds in the end groups show the two highest dissociation rates, which are four times larger than the highest bond dissociation rate in the main chain (i.e., the dissociation rate of the C–O bond in the main chain). This demonstrates that decomposition of PFPE molecules occurs mostly at the polar end groups. This also rationally explain the faster decomposition of polar PFPEs than the nonpolar ones. In the main chain, the C–O bond shows roughly four times larger dissociation rate than the C–C bond. This should be the reason for the faster decomposition of Z than Demnum, as the number of C–O bond in Z is roughly twice that in Demnum.

Table 2-4 Bond dissociation ratio for Z-tetraol in the shearing simulation.

Bond location	Bond type	Bond dissociation ratio (%)
Main chain	C–C	3.43
	C–O	13.2
	C–F	0.00
End group	C–C	3.43
	C–OC	58.8
	C–OH	63.8
	C–H	0.00
	O–H	16.9

2.4 Conclusions

We developed a ReaxFF force field for PFPE, and using this force field we performed reactive MD simulations to gain insights into mechano-chemical decomposition of nanometer-thick PFPE films at the HDI of HAMR. For comparison, pure thermal decomposition of bulk PFPE was also simulated. The

logarithm of the rate constant of pure thermal decomposition exhibits a linear relation with the reciprocal of temperature, indicating Arrhenius behavior. The time constant of pure thermal decomposition was estimated from the Arrhenius plot to be 11 and 0.078 s at the HAMR operation temperatures of 700 and 800 K. In contrast, the decomposition time constant decreased to approximately 10 ns when PFPE films were subjected to normal impact or horizontal shear from the head at normal pressure of 0.1 GPa and shear speed of 50 m/s, in addition to heating at 700 K. We thus concluded that, within the 1-ns heating time of HAMR, pure thermal decomposition hardly occurs, whereas mechano-chemical decomposition is highly likely to occur.

Our simulations results showed that the decomposition rate constant of PFPE films subjected to confined shear increases with normal pressure. The increase is well fitted by a linear stress-activated Arrhenius curve at high normal pressures, whereas this is not the case at low normal pressures. According to the stress-assisted reaction rate theory, the deviation at low normal pressures can be interpreted by the change of activation volume. Hence, we caution against extrapolating the linear stress-activated Arrhenius curve obtained at high normal pressures to low normal pressures, which could cause significant overestimation of decomposition rate constants at low normal pressures.

Our simulation results also showed that polar molecules D-4OH and Z-tetrol decompose more rapidly than nonpolar molecules Demnum and Z, and the nonpolar Z decomposes more rapidly than the nonpolar Demnum. We confirmed that the decomposition of PFPE molecules is mainly caused by the dissociation of C–OH and ether C–OC bonds in the polar end groups, and in the main chain the C–O bond is more likely to dissociate than the C–C bond. Our findings extend understanding of mechano-chemical decomposition of nanometer-thick liquid films and are instructive for the design of head–disk interface in HAMR.

Chapter 3

Mechano-Chemical Reactions of Perfluoropolyether Lubricant Films in Heat-Assisted Magnetic Recording: Effect of Water

3.1 Introduction

As described in Chapter 1, water cannot be completely removed from the HDI, thus may catalyze the reaction of PFPE molecules due to their polarity. Therefore, it is crucial to elucidate the effect of water on the stability of PFPE boundary films. Extensive experimental and simulation studies have demonstrated that water molecules interact with the polar end groups of PFPE molecules, leading to substantial changes in both the physical and chemical properties of PFPE lubricant films [54,105–114]. For instance, it was reported that water altered the distribution and diffusion of PFPE lubricant films on disk surfaces [105–109], as well as promoted debonding from the disk surface and transfer of lubricant molecules to the head [109–111]. It was also found that water molecules can reduce the pressure of the air bearing in the HDI, increasing the probability of head–disk contact [112], and can evaporate and adsorb to the head, forming smears [113]. Dai et al. observed that contact sliding on PFPE lubricant films in humid environments led to the formation of viscous liquid droplets or solid-like agglomerates [105]. These products were suggested to be composed of PFPE micelles; however, the detailed mechanism behind their formation remains unclear. On the other hand, Kasai et al. inferred that water can passivate electron deficient sites on the head surface which are responsible for the catalytic decomposition of PFPE lubricants, thus enhancing the durability of PFPE lubricant films [114]. Recently, Lotfi et al. performed reactive MD simulations for a bulk mixture of PFPE D-4OH and water at high temperatures, and they found that water accelerated the degradation of D-4OH through scission of C–O bonds in the main chain and end groups [54]. However, despite the extensive studies to date, there is still a lack of comprehensive atomic-level understanding of how PFPE decomposition occurs under the combined influence of heat, mechanical stress, and water.

To address this issue, this chapter aims to examine the chemical reactions of nanometer-thick PFPE lubricant films subjected to heating and confined shear at different normal pressures, both in the presence and absence of water.

3.2 Simulation Method

3.2.1 Force Field

The ReaxFF force field, which was developed for PFPE molecules in Chapter 2, was used in this study. To verify the applicability of the ReaxFF to reactions between PFPE and water, we calculated the energies of a hydrolysis reaction of PFPE, which is the most frequent reaction found in this study and described in detail in Section 3.3.2.1, using the ReaxFF and DFT methods. The activation energy calculated by the ReaxFF is 65.0 kcal/mol, with a relatively small error of 7.6% compared to the value of 60.4 kcal/mol calculated by the DFT. The agreement justifies the applicability of the ReaxFF to reactions between PFPE and water.

3.2.2 Models and Procedures

Figure 3-1 shows the all-atom models of the lubricant and entire system. The lubricant was PFPE D-4OH, which is practically used in the HDI. Its molecular formula and molecular weight (Mw) is 1820 g/mol, which is the same as that used in the research of Chapter 2. The head and disk were modeled in the same manner as described in Section 2.2.2.2, but with a reduced thickness of approximately 48% to 9.8 Å in order to save computational time. Compared to the thicker substrate, employing this thinner substrate yielded no significant differences in terms of the structural deformation of the substrate and temperature control of the liquid during the shearing simulation. This indicates that the thin substrate does not encounter any issues with rigidity or thermostat effect.

First, systems with a lubricant film of pure D-4OH or D-4OH randomly mixed with water confined between the head and disk were constructed. The dimensions of the systems in the x and y directions were 8.04624 nm × 8.04624 nm, and periodic boundary conditions were applied in the two directions. Non-periodic boundary condition was applied in the z direction. The numbers of D-4OH and H_2O molecules were 40 and 100, respectively, corresponding to a concentration of water of 2.4 wt%. The number of water molecules was determined to ensure effective observation of reaction events. The film thickness was approximately 1.3 nm. The target temperature was fixed at 700 K. The normal pressure applied on the head was set to 0.2, 0.5, 1.0, or 1.5 GPa, with 0.2 GPa being typical in the HDI [8]. Note
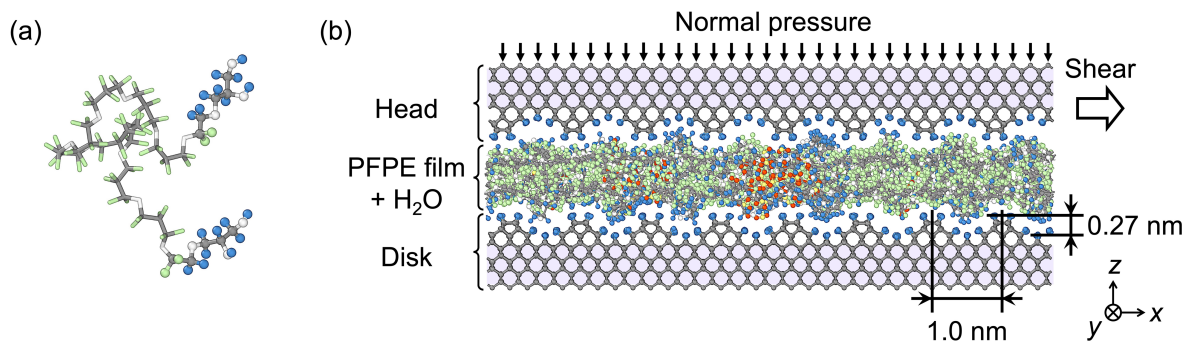
Figure 3-1 All-atom models of (a) PFPE D-4OH and (b) the entire system. In (a), atoms of the end groups are indicated with balls, whereas the main chain is simply indicated with sticks for clarity. The gray, blue, white, and green represent carbon, hydrogen, oxygen and fluorine atoms of D-4OH and head and disk, respectively. The yellow and red represent oxygen and hydrogen atoms of water, respectively. Thermostated atoms are marked with purple in (b).

that lower normal pressures were used in this study compared to those in Chapter 2, in order to distinctly discern the influence of water. As described in detail in Section 3.2.2.1, we formulated a series of compression, relaxation, and recompression procedures and carefully selected the simulation conditions so that no chemical reactions occurred during the system construction.

Subsequently, the lubricant film was sheared by applying a constant velocity of 25 m/s in the x direction to the carbon atoms in the uppermost layer of the head while fixing the carbon atoms in the lowermost layer of the disk. The temperature and normal pressure were kept constant at the target values. The Nosé-Hoover thermostat [93,94] was applied only to the intermediate layers of the head and disk [marked with purple in Figure 3-1(b)] to avoid any unphysical influence on the behavior of liquid molecules [95–98]. The shearing process was performed for 0.5 ns with a time step of 0.2 fs. The time to start shearing was set to time zero ($t = 0$) and reactions of D-4OH during the entire shearing process were analyzed.

For each of the systems with and without water at different normal pressures, 10 simulations were performed using different initial configurations. However, simulations without water at 0.2 GPa were deemed unnecessary and not conducted, as almost no reactions were observed without water at 0.5 GPa [see Fig. 2(c)]. All the MD simulations were conducted by LAMMPS [92]. The initial configurations of the lubricant films were constructed by Packmol [115] and Moltemplate [116]. The simulation results were visualized using OVITO [117].

3.2.2.1 Procedures for Forming Lubricant Films

To ensure that chemical reactions do not occur during the process of forming lubricant films, we formulated a set of procedures, as described in detail below.

(1) Compression

The objective is to form a liquid film from liquid molecules. First, D-4OH molecules or randomly mixed D-4OH and water molecules were placed between the upper and lower solid substrates. Then, the x, y, and z coordinates of the outermost carbon atoms of the lower substrate were fixed. A normal pressure of 0.1 GPa was applied to the outermost carbon atoms of the upper solid substrate to compress the liquid molecules and form a liquid film. The temperature was set to 393 K. To avoid any chemical reactions during the compression, we utilized the non-reactive COMPASS II force field.

(2) Relaxation

The objective is to relieve the internal stress in the compressed liquid film. First, the upper substrate was lifted away from the liquid film and then the x, y, and z coordinates of the outermost carbon atoms were fixed, so that the liquid film was not compressed by the upper substrate. Next, the liquid film was relaxed at 393 K for 1 ns. Finally, the temperature was lowered to 293 K and the liquid film was further relaxed at this temperature for 1 ns.

(3) Switch of force field

Subsequently, the force field was switched from the COMPASS II to ReaxFF. Because the equilibrium configurations of the system are not exactly the same for the two force fields, atoms could move rapidly upon switching, resulting in bond breakage. To prevent this, we reduced the temperature for the entire system to 1 K to slow down the motion of atoms. We confirmed that 1 ps was adequate for achieving equilibrium with the ReaxFF.

(4) Recompression

The objective is to obtain a liquid film confined between the solid substrates at the target temperature and normal pressure. First, the temperature of the entire system was increased from 1 to 293 K at a rate of 292 K/ps. Next, the liquid film was compressed by first applying a normal pressure of 0.1 MPa for 50 ps, then a constant velocity of $v_z = -20$ m/s for 30 ps, and finally the target normal pressure of 0.5, 1.0, or 1.5 GPa until reaching equilibrium on the upper substrate. The constant velocity compression was applied to prevent sudden change in the normal pressure, which could induce reactions

of the liquid molecules because of the strong impact from the upper substrate. Finally, 40 ps simulation was performed to increase the temperature from 293 K to the target value of 700 K.

In the above procedures, the timestep was set to 1.0 fs for the simulations using the COMPASS II, 0.1 fs for switching from the COMPASS II to ReaxFF, and 0.2 fs for the equilibration using the ReaxFF. Nosé-Hoover thermostat was applied to the entire system except for the outermost carbon atoms of the upper and lower substrates.

3.3 Results and Discussion

3.3.1 Reaction Rates

First, we investigated the effect of water on the reaction rates of D-4OH at different normal pressures. For first order reactions, the reaction rate constant k can be obtained by fitting with Eq. (2-3).

Figure 3-2(a) and (b) show the time evolution of $\ln(N_t/N_0)$ of intact D-4OH molecules with and without water, respectively. In Figure 3-2(b), the result at the normal pressure of 0.5 GPa is not shown because only one reaction of D-4OH was observed in the 10 simulations. All the results are well fitted by straight lines described in Eq. (2-3), with the coefficients of determination R^2 larger than 0.98, indicating that the reactions of D-4OH follow the first-order kinetics regardless of the presence of water.

The reaction rate constants k were determined by the slopes of the fitted straight lines in Figure 3-2(a) and (b) and are plotted in Figure 3-2(c). Error bars are the standard deviation of 10 simulations. Regardless of the presence of water, the reaction rate constants of D-4OH increase with increasing normal pressure. Interestingly, the presence of water consistently increases the reaction rate constants of D-4OH at all the normal pressures. At 0.2 and 0.5 GPa, the reaction rate constants in the presence of water are approximately 10^8 s^{-1}, significantly larger compared to the nearly zero value in the absence of water. However, at 1.0 and 1.5 GPa, the reaction rate constants in the presence of water are only 2.0 and 1.4 times those in absence of water, respectively. These results demonstrate that water accelerates the mechano-chemical reactions of D-4OH and such effect is more pronounced at lower pressures than at higher pressures.
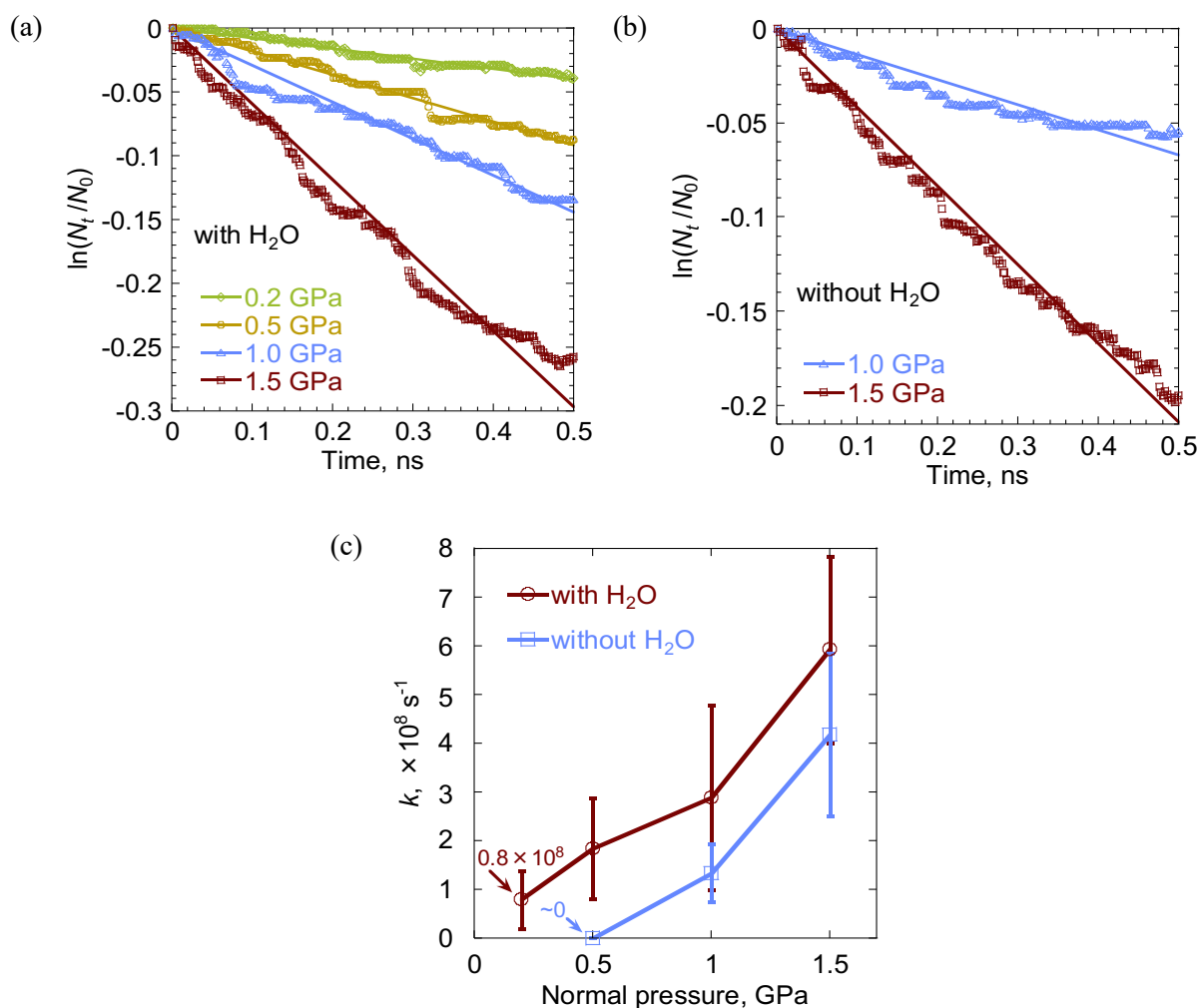
Figure 3-2 Time evolution of $\ln(N_t/N_0)$ of intact D-4OH molecules (a) with and (b) without water at different normal pressures. The values of $\ln(N_t/N_0)$ were averaged over 10 simulations. The result at the normal pressure of 0.5 GPa is not shown in (b) because only one reaction of D-4OH was observed in the 10 simulations. Straight lines are linear fits to Eq. (2-3). (c) Comparison of reaction rate constants k at different normal pressures with and without water. Error bars represent the standard deviation of 10 simulations.

To judge whether water can induce reactions of D-4OH within the approximately 1-ns heating time in HAMR, we calculated the reaction time constant τ as the reciprocal of k. Even at the lower normal pressures of 0.2 and 0.5 GPa, the addition of water significantly reduces τ to the order of 10 and 1 ns, respectively, which are comparable to the typical heating time in HAMR. Thus, we infer that D-4OH molecules subjected to confined shear in HAMR are highly likely to degrade in the presence of water.

38

3.3.2 Reaction Types and Pathways

To gain insights into the effect of water on accelerating the reactions of D-4OH at different normal pressures, we identified and classified the reactions of D-4OH that involve intact D-4OH molecules as reactants into different types. Three types were observed: (1) hydrolysis reaction, (2) end group–end group association (EEA) reaction, and (3) main chain–end group association (MEA) reaction. All three types of reactions occur when water is added, whereas only the last two types of reactions occur when no water is added.

The pathways of the three types of reactions are illustrated in Figure 3-3 and described in detail below.

3.3.2.1 Pathways of Hydrolysis Reaction

As shown in Figure 3-3(a), the hydrolysis reaction involves the decomposition of a D-4OH molecule by reacting with a water molecule. There are pathways (i) and (ii), with the former accounting for 83% of the total count of the hydrolysis reaction occurring in our simulations. In both pathways, one of the ether bonds of C–O–C at the end groups of D-4OH and one of the O–H bonds in the water molecule break. The resulting fragments then associate to form one glycerol molecule and a derivative of D-4OH with one end group converted to a $-CF_2CH_2OH$ group. The reactants and products in both pathways are identical, with the only difference between the two pathways being the location of the dissociated ether bond in D-4OH.

3.3.2.2 Pathways of EEA Reaction

As shown in Figure 3-3(b), the EEA reaction is a reaction between two D-4OH molecules. Two D-4OH molecules decompose at the CO–C and C–OH bond of one end group, respectively. The resulting fragments then associate to form a glycerol molecule and a longer chain molecule in which the two D-4OH molecules, each with a part of one end group being truncated, are linked together.

3.3.2.3 Pathways of MEA Reaction

As shown in Figure 3-3(c), the MEA reaction is also a reaction between two D-4OH molecules to

39

produce two products. Different from the EEA reaction, in the MEA reaction, one D-4OH molecule decomposes at an arbitrary ether bond of the main chain, and hence both products contain the main chain fragment of $(CF_2CF_2CF_2O)_n$. There are various reaction pathways and Figure 3-3(c) illustrates two representative pathways. The broken bond at the end group of one D-4OH molecule can be any of the C–O [pathway (i)] or C–C [pathway (ii)] bonds. As will be seen in Section 3.3.4, pathway (i) is the major one rather than pathway (ii).
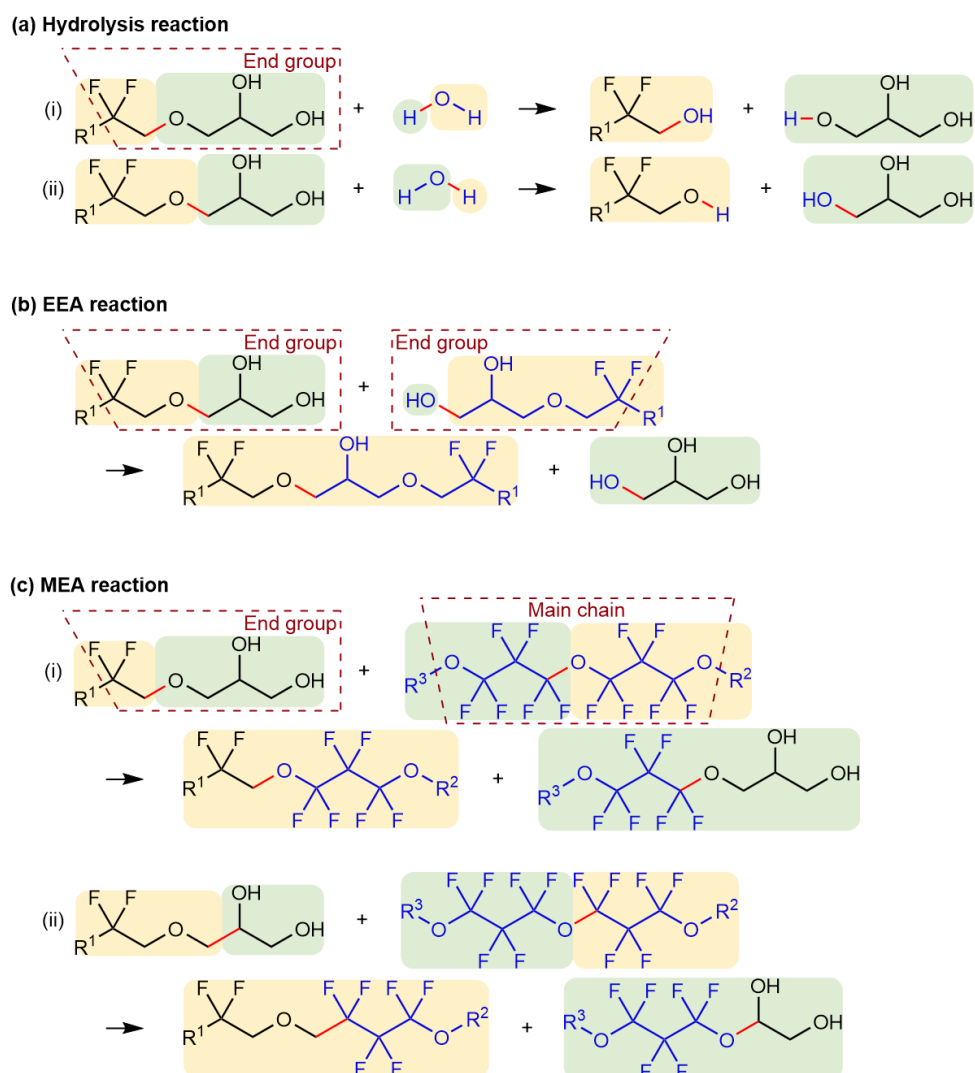
Figure 3-3 Schematic diagram of pathways of (a) hydrolysis, (b) EEA, and (c) MEA reactions. The two reactant molecules are indicated in black and blue, respectively. The bonds in red represent those breaking and forming in the reactions. There are two pathways of the hydrolysis reaction and various pathways of the MEA reaction. The pathways (i) and (ii) in (c) are two representative examples of the MEA reaction, which result from the dissociation of either a C–O or a C–C bond in one of the end groups of D-4OH.

3.3.3 Effect of Water on the Three Types of Reactions at Different Normal Pressures

We then compared the speed of the three types of reactions in the presence and absence of water and at different normal pressures. Here, the speed was simply quantified by the total count of each type of reactions occurring in the 10 simulations of 0.5 ns shear each. The results are shown in Figure 3-4. Because the hydrolysis reaction only occurs when adding water, we discuss the results of the hydrolysis reaction and non-hydrolysis EEA and MEA reactions separately below.
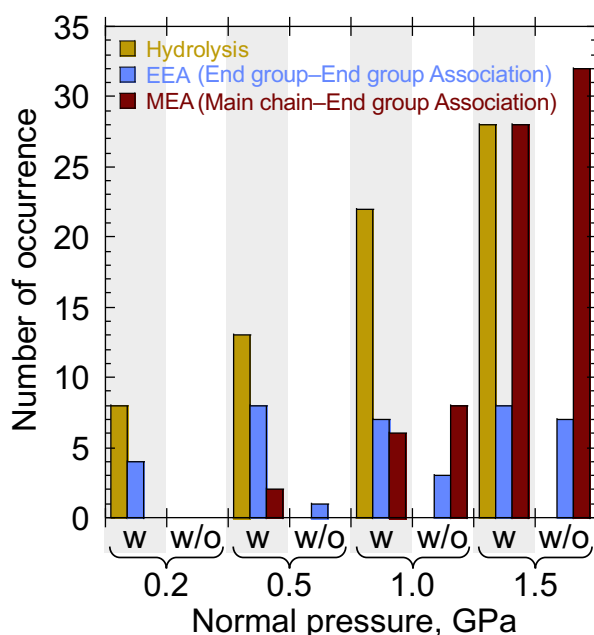
Figure 3-4 Total number of occurrences of each type of reactions in the 10 simulations of 0.5 ns shear each at different normal pressures. w and w/o represent the simulations with and without adding water, respectively.

3.3.3.1 Hydrolysis Reaction

The yellow bars in Figure 3-4 show the results of the hydrolysis reaction. Among the three types of reactions in the presence of water, the proportion of the hydrolysis reaction is 67% at 0.2 GPa, 57% at 0.5 GPa, 63% at 1.0 GPa, and 44% at 1.5 GPa. While the hydrolysis reaction exhibits a relatively low proportion at 1.5 GPa because of the significant increase in the number of the MEA reaction, it is still one major reaction. These results demonstrate that the hydrolysis reaction is the main reason for the

mechano-chemical decomposition of D-4OH molecules in the presence of water.

As the normal pressure increases from 0.2 to 0.5 GPa, from 0.5 to 1.0 GPa and from 1.0 to 1.5 GPa, the hydrolysis reaction becomes 1.6, 1.7 and 1.3 times faster, respectively. These results suggest that normal pressure accelerates the hydrolysis reaction, but this effect tends to saturate at higher pressures.

3.3.3.2 Non-Hydrolysis EEA and MEA Reactions

Comparing the non-hydrolysis reactions in the presence and absence of water shown in Figure 3-4, we notice that water accelerates the EEA reaction but not the MEA reaction. Specifically, adding water leads to 8, 2.3, and 1.1-fold increase in the number of EEA reaction at the normal pressures of 0.5, 1.0, and 1.5 GPa, respectively. At 0.2 GPa, the EEA reaction still occurs in the presence of water, while in the absence of water it can be inferred by extrapolation from the results at higher pressures that the EEA reaction hardly occurs. These demonstrate that the effect of water on accelerating the EEA reaction is more pronounced at lower pressures. As the normal pressure increases, the number of the EEA reaction increases only when water is absent, whereas the number of the MEA reaction significantly increases regardless of the presence or absence of water.

The above analysis of the three types of reactions elucidates the mechanism underlying the results presented in Figure 3-2(c). The increased rates of mechano-chemical reactions of D-4OH after adding water are attributed to the occurrence of the hydrolysis reaction and the acceleration of the non-hydrolysis EEA reaction. However, these effects tend to saturate at higher normal pressures. Additionally, the non-hydrolysis MEA reaction is significantly accelerated by normal pressure, even in the absence of water. Therefore, the effect of water on accelerating the mechano-chemical reactions of D-4OH becomes relatively less significant with increasing normal pressure.

The stress-assisted activation energy theory [68,71–74] can explain the pronounced effect of water at lower normal pressures. Normal pressure provides energies to molecules, assisting them in overcoming the activation energy barrier and thus facilitating reactions and leading to high reaction rates. However, at lower normal pressures of 0.2 and 0.5 GPa, due to insufficient energy supplementation from normal pressure, the MEA and non-water-catalyzed EEA reactions are still difficult to occur. In contrast, the presence of water enables the hydrolysis reaction and water-catalyzed EEA reaction to take place, as their activation energies are low and do not require additional energy from normal pressure to drive

the reactions. This distinct influence of water on the activation energies is more evident in reaction rates at lower normal pressures.

To understand why water accelerates the EEA but not the MEA reaction, we visualized the distribution of water molecules, as shown in Figure 3-5. It is evident that most water molecules, which were initially randomly mixed with D-4OH molecules, aggregate to form clusters and are encompassed by the polar end groups of D-4OH molecules, resulting in a water-in-oil structure. This phenomenon was highlighted in previous computational and experimental studies [109,118]. It is attributed to the strong attractive hydrogen bonding interaction between water and the hydroxyl end groups of D-4OH and the repulsive hydrophobic interaction between water and the perfluorinated polyether main chain of D-4OH. As a result, few water molecules locate in close proximity to the main chains of D-4OH molecules. Therefore, the presence of water has little effect on the MEA reaction, which involves breaking the main chain of one D-4OH molecule [Figure 3-3(c)].
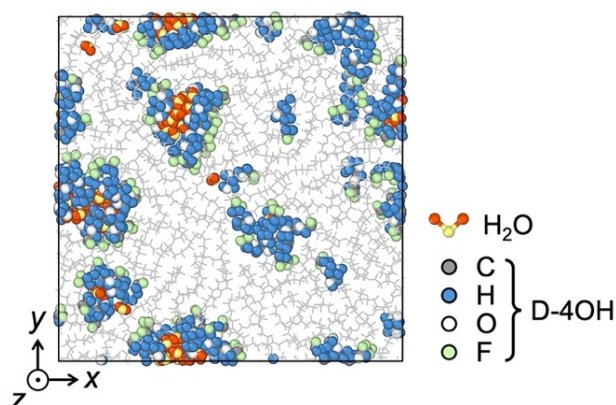
Figure 3-5 Snapshot of the MD simulation showing the distribution of water molecules. For clarity, atoms of water and the end groups of D-4OH are indicated with balls, whereas the main chains of D-4OH are simply indicated with gray sticks.

In contrast, we found that water serves as a catalyst for the EEA reaction, which involves cleavage of one end group in each of two D-4OH molecules [Figure 3-3(b)]. Figure 3-6 shows one reaction process. As indicated in Step 1, the reaction involves the C1 and O1 atoms in one D-4OH molecule (Mol1) and the C2 and O2 atoms in the other D-4OH molecule (Mol2). It is noted that some water molecules locate in close proximity to the end groups of D-4OH. At the transition state (TS) shown in Step 2, a rhombus structure is formed between the two end groups of the D-4OH molecules because of the formation of the C1–O2 and O1–C2 bonds. Simultaneously, the oxygen atom of a water molecule

forms two hydrogen bonds with the hydrogen atoms of the primary and secondary hydroxyl end group in the two D-4OH molecules. As this water molecule is attracted by the cohesive force from the cluster of water, a dragging force is exerted on the rhombus structure to break the C1–O1 and C2–O2 bonds. Finally, as shown in Step 3, the two D-4OH polymerize through the C1–O2 bond and form a glycerol molecule through the O1–C2 bond.
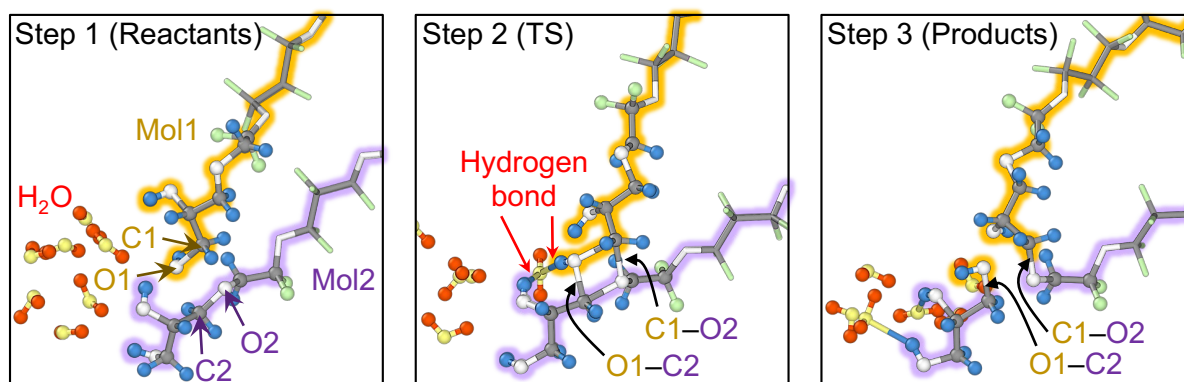
Figure 3-6 Snapshots of the MD simulation showing the process of the EEA reaction between two D-4OH molecules (Mol1 in yellow and Mol2 in purple) in the presence of water. For clarity, atoms of water and end groups of D-4OH are indicated with the same color balls as in Figure 3-5, whereas the main chains of D-4OH are simply indicated with sticks and molecules unrelated to the reaction are hidden.

3.3.4 Number of Broken Bonds

To identify the vulnerable bonds in D-4OH molecule under the influence of water at different normal pressures, we counted the number of broken bonds of five different types in the 10 simulations. As indicated in Figure 3-7, the five types include one C–O bond in the main chain (MC), two C–O bonds in the end group (EG), and two C–C bonds in the end group, which are referred to as $C–OC_{(MC)}$, $C–OC_{(EG)}$, $C–OH_{(EG)}$, $C–C_{1(EG)}$, and $C–C_{2(EG)}$, respectively.

The results shown in Figure 3-8 demonstrate that C–O bonds are more susceptible to cleavage than C–C bonds, which is consistent with the results in Section 2.3.4.2 and previous study [54]. Thus, the following discussion will focus on the effect of water on the cleavage of the three types of C–O bonds. Adding water leads to the greatest number of broken $C–OC_{(EG)}$ bonds at any of the normal pressures, because all the three types of reactions can break this bond. At the lower normal pressures of 0.2 and
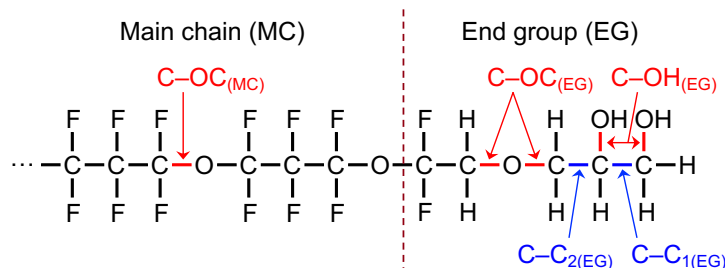
Figure 3-7 Types of bonds in the main chain (MC) and end group (EG) of D-4OH.
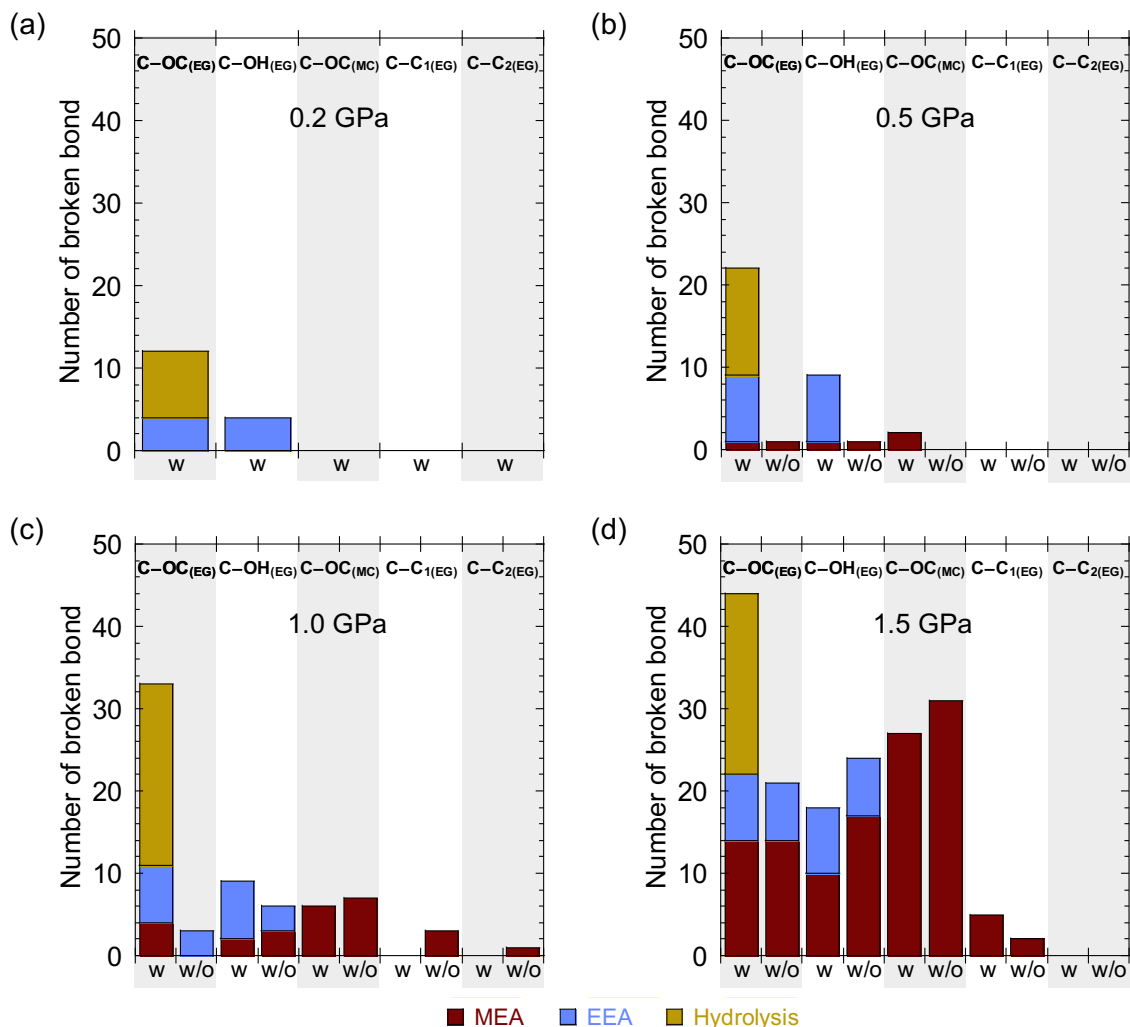
Figure 3-8 Number of broken bonds of each type at (a) 0.2, (b) 0.5, (c) 1.0, and (d) 1.5 GPa. w and w/o represent the simulations with and without adding water, respectively.

0.5 GPa, adding water noticeably increases the number of broken C–OH$_{(EG)}$ bonds compared to without adding water, because water catalyzes the EEA reaction. However, beyond 0.5 GPa, the difference in the number of broken C–OH$_{(EG)}$ bonds between with and without water diminishes and even reverses, owing to saturation of the EEA reaction and increase in the MEA reaction even in the absence of water.

Water shows no effect on the cleavage of C–OC$_{(MC)}$ bond, which, however, increases in number with increasing normal pressure solely due to the MEA reaction. Briefly, water mainly dissociates the C–OC$_{(EG)}$ and C–OH$_{(EG)}$ bonds in the end groups, whereas high normal pressure dissociates all the three types of C–O bonds in the end groups and main chain. The effect of water on dissociating the C–OH$_{(EG)}$ bond saturates at higher normal pressures.

For the MEA reaction, which dissociates all the types of C–O and C–C bonds in the end groups (Section 3.3.2.3), Figure 3-8 shows that the C–O bonds are the major dissociated bonds in the end groups rather than the C–C bonds, and the C–OC$_{(EG)}$ and C–OH$_{(EG)}$ bonds are roughly equally involved.

3.3.5 Species of Reaction Products

We analyzed the species of the reaction products that remained stable in the 10 simulations by counting the total numbers based on their Mw. The results are shown in Figure 3-9. For comparison, the Mw of an intact D-4OH is marked with a red dashed line in the figure. The results demonstrate that the presence of water or increase in normal pressure significantly increases the total number of the products; however, their effect on the species (i.e., the Mw) of the products is distinct. Adding water does not significantly increase the species of the products, except for 0.2 and 0.5 GPa where reactions hardly occur without water. This is because water just induces the hydrolysis reaction and accelerates the EEA reaction, and the products of the two types of reactions are limited in species as seen in Figure 3-9 and Sections 3.3.2.1 and 3.3.2.2.

In contrast, increase in normal pressure significantly increases the species of the products, which are the most diverse at the high normal pressure of 1.5 GPa. One reason is that normal pressure accelerates the MEA reaction, and this type of reaction has various pathways and thus products as seen in Figure 3-9 and Section 3.3.2.3. The other reason is that, as the normal pressure increases, some products become less chemically stable and undergo further reactions with D-4OH or water molecules. The products of the subsequent reactions are different in species from those of the initial reactions. Such chain reactions were only observed at 1.5 GPa, not at 0.2, 0.5 and 1.0 GPa. The products of the chain reactions account for 7.6% of the total 251 products and 9.7% of the total 113 products in the presence and absence of water. As seen from Table 3-1, the subsequent reactions mainly include the MEA reaction in both the presence and absence of water and the hydrolysis reaction in the presence of water.
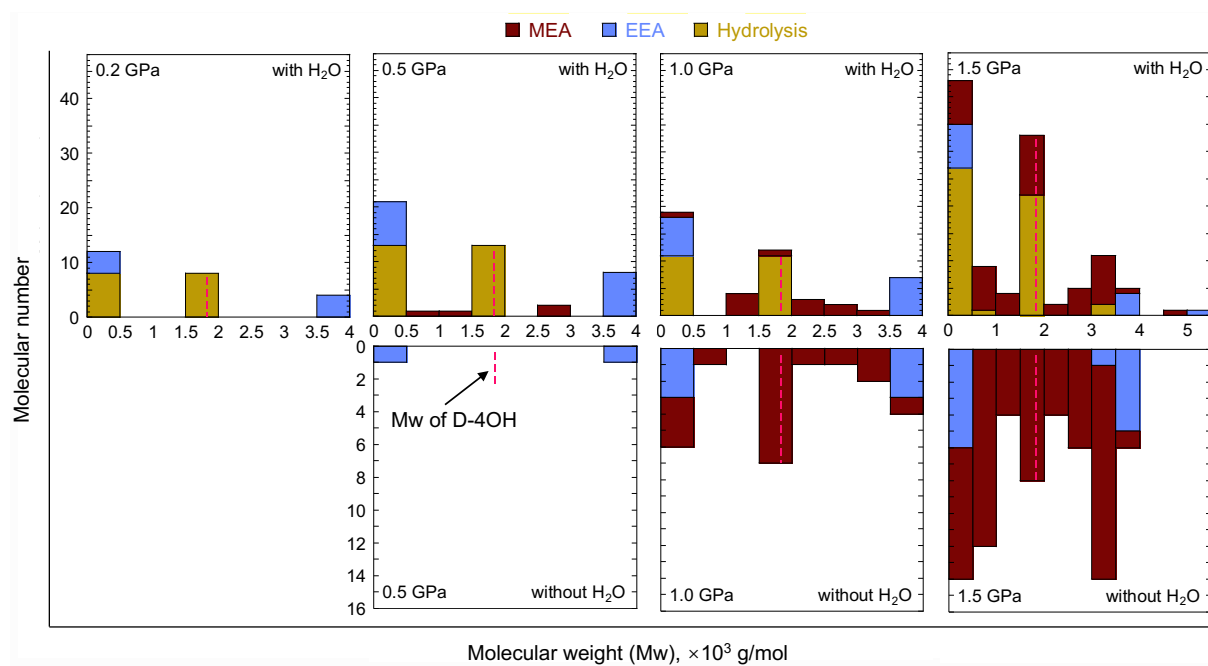
Figure 3-9 Number distribution of stable products with different molecular weights (Mw). The red dashed line indicates the Mw of an intact D-4OH molecule. Note that the upper and lower plots have different scales of the vertical axis and the rightmost plots have different scales of the horizontal axis from the others.

Table 3-1 Number of the subsequent reactions of each type at 1.5 GPa.

	MEA	EEA	Hydrolysis
with H$_2$O	10	1	4
without H$_2$O	7	1	–

3.4 Conclusions

Using our previously developed ReaxFF of PFPE, we performed nonequilibrium reactive MD simulations to investigate the effect of water on the mechano-chemical decomposition of PFPE D-4OH lubricant films subjected to heating at 700 K and confined shear at the normal pressures of 0.2, 0.5, 1.0, or 1.5 GPa. We found that the presence of water accelerates the mechano-chemical reactions of D-4OH and this effect is more pronounced at lower pressures than at higher pressures, rendering the D-4OH

lubricant films likely to degrade during the HAMR system operation. We elucidated that three types of reactions, i.e., hydrolysis reaction, EEA reaction, and MEA reaction, occur in the presence of water, with the hydrolysis reaction being the major one. In contrast, only the last two types of reactions occur in the absence of water. Water molecules aggregate to form clusters and are encompassed by the polar end groups of D-4OH molecules, resulting in a water-in-oil structure. Therefore, water induces the hydrolysis reaction and catalyzes the EEA reaction, which involve the dissociation of D-4OH end groups, while having no effect on the MEA reaction, which involves the dissociation of D-4OH main chains. We found that water primarily dissociates the C–O bonds in the end groups, while high normal pressures dissociate the C–O bonds in both the end groups and main chains. The effect of water on the dissociation of the C–OC bonds in the end groups is more significant compared to the C–OH bonds in the end groups, and both effects level off at higher normal pressures. We also confirmed that adding water or increasing in normal pressure significantly increases the total number of products, but adding water does not significantly increase the species of the products. Our findings enhance comprehension of the mechano-chemical reactions of nanometer-thick PFPE lubricant films in the HDI under the effect of water, and are instructive for developing more effective lubrication strategies in HAMR systems.

Chapter 4

Adsorption Behavior of TEMPO-Based Organic Friction Modifier during Sliding between Iron Oxide Surfaces

4.1 Introduction

As described in Chapter 1, to achieve effective nanometer-thick OFM boundary films with high friction-reducing performance, it is crucial to understand how the OFM molecular structures relate to the adsorption behaviors and structures of boundary films.

Friction and wear-reducing performance of OFMs depends critically on the strength of the adsorbed boundary films and the adsorption kinetics [20,25]. The film strength, i.e., the ability to withstand loaded sliding, is determined not only by the surface adsorption strength of individual OFM molecules but also by the cumulative cohesion strength of the films. The former depends solely on the type and number of functional groups [23,119–121]. In contrast, the latter depends on the structure of the films, such as the number of layers [38,122], film thickness [36,123,124], surface coverage [23,33,125,126], packing density [127–129], and conformation of OFM molecules [130], which is governed not only by the functional groups [23,126] but also by the number [38], length [23,35,120,131], unsaturation [35,38,128,131,132], and branching of the alkyl chains [129]. The adsorption kinetics depends on the chemical structure not only of the functional groups and alkyl chains of OFMs but also of lubricating oils because adsorption involves a process of OFM molecules diffusing onto the solid surfaces from the lubricating oils [38,133–136]. Literature shows that, on ferrous substrates, OFMs with carboxylic acid and amine groups are generally more effective than with alcohol and ester groups. It was reported that, compared with a single functional group, multiple functional groups lead to strong adsorption owing to multi-site adsorption or chelate effect, and thereby high adsorbed masses; however, the steric hindrance caused by the large size could slow down the adsorption kinetics [38,129]. Longer alkyl chains were found to result in thicker boundary films [23,35], and linear saturated alkyl chains are believed to result in ordered and close-packed boundary films compared with branched and unsaturated ones [132]. Many studies demonstrated that high adsorbed masses or thick films result in low friction and wear, possibly due to the high surface coverage and packing density [35,38,137]. In contrast, a few recent studies reported that adsorbed masses evidently affect the initial friction but not the steady-state friction [124], and fast adsorption kinetics is effective at reducing friction and wear rather than high adsorbed masses [129]. A recent study also suggests that complete surface coverage is not necessary for effective friction reduction [133]. These findings, including conflicting ones, indicate that the performance of OFMs is

affected by many complex factors and thus its correlation with the molecular structure remains unclear. As a result, despite the extensive studies, the guidelines for optimal molecular design of OFMs have not yet been established.

In our previous studies, we have developed N-(2,2,6,6-tetramethyl-1-oxyl-4-piperidinyl) dodecaneamide, which will be simply referred to as $C_{12}TEMPO$ hereafter, as a new type of OFM [138,139]. Note that it is named as $C_{12}TEMPO$ and $C_{12}Amide-TEMPO$ in Ref. [138] and Ref. [139], respectively. As is seen from Figure 4-1(a), it consists of a linear saturated alkyl chain, an amide (–CONH–) linkage, a six-membered ring, and a terminal oxygen radical (O•). The two functional groups of different types, i.e., the amide group and oxygen radical, are particularly unique as compared with conventional OFMs, which usually have a single functional group or multiple functional groups of the same type. Pin-on-disk type tribological tests have demonstrated that $C_{12}TEMPO$ exhibits higher load-carrying capacity, higher wear-reducing effect, and more stable friction coefficient over time than the conventional OFMs of stearic acid and GMO [138,139]. The optimized static structure from QM calculations with the DFT showed that both the radical and amide group chemically adsorb on iron oxide surfaces, thereby leading to stronger surface adsorption than stearic acid and GMO [139]. Although the QM results correlate with the good performance of $C_{12}TEMPO$, the adsorption behavior of $C_{12}TEMPO$ in lubricating oils during sliding and the structure of the adsorbed boundary films are yet to be elucidated.

In this chapter, aiming to further understand the mechanism for the high tribological performance of $C_{12}TEMPO$ and also provide hints for optimal molecular design of OFMs, we performed non-equilibrium MD simulations [66,67] for confined shear of $C_{12}TEMPO$ solution in base oil between iron oxide surfaces. We gained molecular-level insights into both the structure of the boundary films and its dynamic variation during sliding. The findings from our simulations can reasonably explain the superior tribological performance of $C_{12}TEMPO$ observed experimentally.

4.2 Simulation Method

4.2.1 Models and Procedures

Figure 4-1(a) and (b) show the chemical structures and all-atom models of the OFM and base oil used in this study. The OFM was $C_{12}TEMPO$, and the base oil was poly-alpha-olefin (PAO) lubricating

oil and modeled as tetramers of 1-decene(9-methyl-11,13-dioctyltricosane) [140,141]. Their molecular weights are 354 and 563 g/mol, respectively. The solid surfaces confining the OFM and base oil were modeled as Fe_2O_3 with (001) surface orientation [121,142,143].

The COMPASS II force field [91] was used to dictate the atomic interactions. Harmonic bond and angle potentials with the force constant of 130 kcal/mol/$Å^2$ and 130 kcal/mol were added for atoms in the substrates to reproduce the thermal vibration [125]. The force field used in this study was validated by comparing the bulk density of PAO and C_{12}TEMPO (Table 4-3) and interaction energies between C_3TEMPO and Fe_2O_3 (001) surfaces (Figure 4-3) with experimental and DFT results.

Figure 4-1(c) shows one of the initial configurations for the MD simulations. The dimensions in the x and y directions were 4.360 nm × 5.035 nm and periodic boundary conditions were applied in the two directions. Same as in the previous MD study for conventional OFMs [33], C_{12}TEMPO molecules with roughly upright conformation were placed on each solid substrate and PAO molecules were inserted between the upper and lower C_{12}TEMPO films. Such initial structures rather than random mixtures of C_{12}TEMPO and PAO allow us to skip the process of C_{12}TEMPO approaching the solid surfaces via diffusion in PAO and thus quickly reach steady-state adsorption [33,67].

Throughout the simulations, a constant normal pressure of 0.5 GPa was applied by exerting a constant downward force to the atoms in the outermost layer of the upper substrate and fixing the atoms in the outermost layer of the lower substrate. Although 0.5 GPa might induce elastohydrodynamic-like behavior for PAO [144,145], it is within the range of 0.4–1.2 GPa used in our experiments [139] and identical to that used in the previous MD study for conventional OFMs [33], thereby facilitating comparison with the previous study. First, the Nosé-Hoover thermostat [93,94] was coupled to the entire system except the fixed layer, and an equilibration run at the temperature of 393 K was executed for 0.5 ns. Then, the temperature was set to the target value of 393, 353, or 313 K and the system was further relaxed for 0.5 ns. Finally, simulations with a shear speed of 10 m/s were carried out for 20 ns by driving the upper and lower substrates at 5 m/s in the y and $-y$ directions. During the shearing process, the thermostat was removed from the liquid films and the interfacial layers (i.e., the two innermost layers) of the substrates to avoid its unphysical influence on the dynamics of the films [95–98]. The timestep was set to 1.0 fs. We confirmed that during the last 10 ns the temperature and pressure remained at the target values, and the thickness and velocity distribution of the confined liquid films also reached steady. Results presented in the next section were obtained from the data in the last 10 ns.

Three different OFM concentrations with 92, 46, and 22 C_{12}TEMPO molecules, referred to as high, medium, and low concentrations, were used. These correspond to surface coverages of 2.10, 1.05, and 0.50 nm^{-2} for the initial configurations. Note that, same as in Ref. [33], the initial surface coverages were calculated as the number of head groups per area of surface. In addition, surface coverages beyond 2.10 nm^{-2} cannot be achieved due to the large size of the head group of C_{12}TEMPO. To focus on the effect of OFM concentration and rule out any other influence, we applied the same shear rate to the liquid films with different OFM concentrations. Hence, we adjusted the number of PAO to be 30, 56, and 69 for the high, medium, and low OFM concentrations, which allows for an identical film thickness of 4.0 nm and shear rate of 2.5×10^9 s^{-1}. The weight percentage of C_{12}TEMPO was 66, 34, and 17 wt% for the high, medium, and low concentrations. Although higher than typical bulk concentrations used in experiments, these concentrations are possible at the contacting conjunctions because of the presence of adsorbed OFMs and low entrainment of lubricating oils in the boundary lubrication regime.

The MD simulations in this study were conducted using LAMMPS [92]. The initial structures of the simulation system were constructed using Packmol [115] and Moltemplate [116]. The simulation results were visualized using OVITO [117].
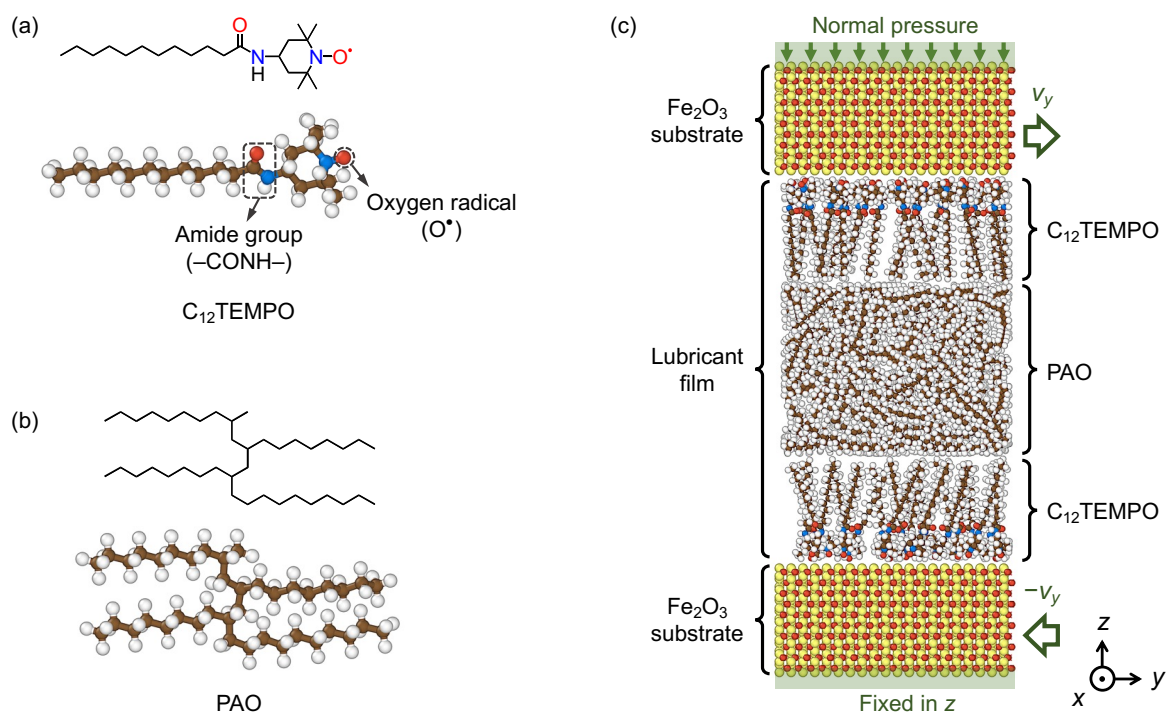
Figure 4-1 Chemical structures and all-atom models of (a) C_{12}TEMPO (OFM) and (b) PAO (base oil) and (c) initial configuration of the MD simulations. The white, brown, red, blue, and yellow represent hydrogen, carbon, oxygen, nitrogen, and iron atoms, respectively.

Note that, to save computational time, our MD simulations used a higher sliding velocity compared to those used in boundary lubrication experiments. Nevertheless, we consider that our simulations can still capture the essential molecular behavior of boundary films in experiments. This is because we consider thin lubricating films or small solid–solid distances to be the most crucial feature of boundary lubrication. In experiments, boundary lubrication typically occurs at low velocities (see Figure 1-1), as high velocities entrain more lubricating oils into contact regions, resulting in thick lubricating films or large solid–solid distances. However, in MD simulations, as the number of lubricant molecules between solid surfaces is predetermined, thin lubricating films or small solid–solid distances are maintained even at high velocities. Therefore, despite the significant difference in sliding velocities, our MD simulations are consistent with experiments regarding the most crucial feature of boundary lubrication.

4.2.2 Force Field Modification

Because the COMPASS II force field does not include atom types for the radical oxygen O•, we have made necessary modifications to the force field parameters for O• using the following procedures.

The O• atom is bonded to a N atom at the head group of C_{12}TEMPO. In COMPASS II force field, there are five different types of O atoms defined for this O–N connection: o1n, o2, o2a, o2c, and o2n. Because the charge value significantly influences the long-range intermolecular interactions in MD simulations, we initially compared the charge values derived from QM results with those present in the COMPASS II force field. QM calculations were performed by Gaussian 16 [77] and Multiwfn [146,147] for single C_{12}TEMPO molecule. After optimizing the molecular structure of C_{12}TEMPO, we calculated charge values based on the electrostatic potential (ESP) and restrained electrostatic potential (RESP).

Table 4-1 shows the charges from QM results and COMPASS II force field. Note that in the COMPASS II force field, changing the atom type of O in the O–N connection also leads to a corresponding change in the bonded N atom type. Therefore, the charge value of the N_{head} atom varies depending on the specific atom type of O•. Except for O• and N_{head} atoms, we also verified the charge values for the amide group (–CONH–) because it also significantly contributes to adsorption [see Figure 4-3(a)]. Among these five atom types, o1n closely aligns with the QM results. Therefore, we selected the o1n force field and proceeded with its modification as detailed below.

Assigning the O• atom as o1n atom type, leads to a problem as the parameters for the $E_{dihedral}$ and

$E_{improper}$ terms are not defined for the molecular topology of C_{12}TEMPO. This includes the absence of energy parameters, as well as the equilibrium bond length and angle values. Here, we only modified the $E_{dihedral}$ parameters for $O\bullet–N_{head}–C_{head}–C_{head}$ (Dihedral 1 in Figure 4-2), as it is crucial for maintaining the structural integrity of the head group. The parameters for equilibrium bond length and angle value were determined from the optimized structure obtained through QM calculations, without any modification. As for the energy parameters, because both the $O\bullet$ atom and the N_{amide} atom form similar dangling bond structures in the head group, we employ the Dihedral 2 parameters, which has been defined in COMPASS II force field, as the parameters for Dihedral 1. The newly added parameters are listed in Table 4-2.

Table 4-1 Comparison of charges from QM results and COMPASS II force field.

Atom	QM		COMPASS II				
	ESP	RESP	o1n	o2	o2a	o2c	o2n
$O\bullet$	−0.37	−0.365	−0.468	−0.025	−0.1912	0	−0.2905
N_{head}	0.049	0.046	0.0941	−0.349	−0.1828	−0.374	−0.0835
N_{amide}	−0.828	−0.805	−0.574				
H_{amide}	0.381	0.371	0.351				
C_{amide}	0.755	0.722	0.45				
O_{amide}	−0.546	−0.536	−0.45				
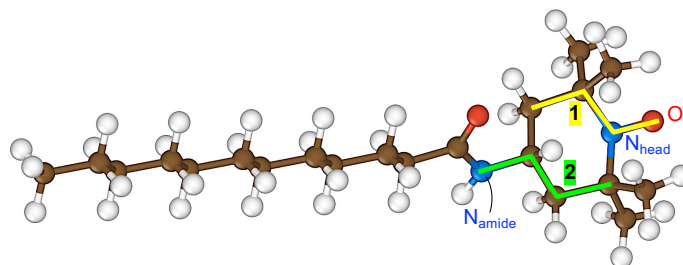
Figure 4-2 Schematic diagram illustrating the modification of the dihedral parameters.

Table 4-2 Modification of $E_{dihedral}$ energy parameters for $O•-N_{head}-C_{head}-C_{head}$ dihedral.

Coefficients of $E_{dihedral}$[a]	Modified parameters
$K1$ (kcal/mol)	0.0972
$K2$ (kcal/mol)	0.0722
$K3$ (kcal/mol)	−0.2581
$A1$ [kcal/(mol·Å)]	−4.2324
$A2$ [kcal/(mol·Å)]	−3.3023
$A3$ [kcal/(mol·Å)]	−1.3244
$B1$ [kcal/(mol·Å)]	0.0742
$B2$ [kcal/(mol·Å)]	0.0105
$B3$ [kcal/(mol·Å)]	0.0518
$C1$ [kcal/(mol·Å)]	−0.0797
$C2$ [kcal/(mol·Å)]	−0.0406
$C3$ [kcal/(mol·Å)]	0.0255
$D1$ (kcal/mol)	−0.5501
$D2$ (kcal/mol)	−1.6982
$D3$ (kcal/mol)	0.2485
$E1$ (kcal/mol)	0.2039
$E2$ (kcal/mol)	0.1602
$E3$ (kcal/mol)	−0.7946
M (kcal/mol)	−1.0631
N [kcal/(mol·Å^2)]	0

[a] Parameters defined in LAMMPS for calculating dihedral energy by COMPASS II force field [148].

4.3 Results and Discussion

As was described in Section 4.2.1, different temperatures and C_{12}TEMPO concentrations were used in our simulations to clarify their influence on the adsorption behavior of C_{12}TEMPO. However, qualitatively similar results were obtained for all the cases. For clarity, only the results for the medium concentration at 393 K, which are the most representative among all the cases, are shown below. Results

for the other cases are shown in the Appendix section (Figures A-1–A-7).

4.3.1 Validation of the Force Field

4.3.1.1 Bulk Densities of PAO and C_{12}TEMPO

MD simulations were conducted for systems consisting of 60 PAO or C_{12}TEMPO molecules in a cubic box with periodic boundary conditions in all the three directions. The systems were first equilibrated in NVT ensemble at 353 K for 0.5 ns, and then equilibrated at 288 K for PAO and at 373 K for C_{12}TEMPO for 0.5 ns. Finally, production run was carried out in NPT ensemble at 1 atm for 1.0 ns. We confirmed that during the last 0.5 ns the pressure and temperature remained at the target values, therefore bulk densities were derived from the data in the last 0.5 ns and the results are shown in Table 4-3. The calculated values are highly consistent with the experimental ones, validating the accuracy of the force field for PAO and C_{12}TEMPO.

Table 4-3 Comparison of bulk densities (g/cm^3) obtained from MD simulation and experiment.

	PAO[a]	C_{12}TEMPO[b]
MD	0.84	0.92
Experiment[c]	0.83	0.93

[a] 288 K, 1 atm; [b] 373 K, 1 atm; [c] The value for PAO was provided by the manufacturer and that for C_{12}TEMPO was measured by ourselves.

4.3.1.2 Interaction Energies Between C_3TEMPO and Fe_2O_3 (001) Surface

To verify the OFM-solid interactions, we performed QM calculations with the density functional theory and MD simulations to derive the interaction energies between C_3TEMPO molecules and Fe_2O_3 (001) surfaces. Note that, rather than C_{12}TEMPO, C_3TEMPO was used to save the computational time. The QM calculations were performed by Vienna Ab initio Simulation Package (VASP) [149–152] packages with the projector-augmented wave (PAW) pseudo-potentials method. The calculation setup was almost the same as reported by Gattinoni et al [121]. The Fe_2O_3 (001) surface was modeled as a single Fe-terminated 6-layer slab 10.07 Å × 15.105 Å in length and width. Each Fe bilayer is ferromagnetic and adjacent bilayers are coupled antiferromagnetically [121,153]. Electronic correlations

in the Fe 3d orbitals were accounted for by adding a Hubbard $U - J = 4$ eV (in the Dudarev approach [121,154]). The band gap was calculated to be 1.71 eV, within the experimentally observed range (1.38−2.09 eV) [155]. The optB86b-vdW functional was selected for its good performance on molecular adsorption. The plane-wave cutoff was set to 550 eV and a Monkhorst–Pack k−point mesh of $4 \times 4 \times 2$ was used. A dipole correction was also applied.

As shown in Figure 4-3(a), two types of adsorbed structures were used, which are for C_3TEMPO lying flat or standing upright on the surfaces, respectively. For the flat conformation, both O• and O_{amide} can bond to Fe atoms, showing double-site adsorption; for the upright conformation, only O• can bond to Fe atoms, showing single-site adsorption. First, the most stable structures for the flat and upright conformations were identified from the QM calculation with at least five different initial configurations for each conformation. Then, by fixing the structures while changing the distance of O•–Fe in the z direction [z_s in Figure 4-3(a)], the interaction energies were calculated by [156,157]

$$E_{int} = E_{sys} - (E_{slab} + E_{mol}) \tag{4-1}$$

where E_{sys} is the total energy of the complex system of the C_3TEMPO molecule and the surface, E_{slab} is the total energy of the surface, and E_{mol} is the total energy of the C_3TEMPO molecule.

Figure 4-3(b) shows the calculation results. Compared with the QM calculations, the MD force field gives rise to long equilibrium distances and weak interaction energies. However, it should be noted that, both from the QM calculations and the MD force field, the interaction energy at the equilibrium distance for the flat conformation is 1.7 times stronger than for the upright conformation. That is, the MD force field accurately reproduce the relative surface interaction strengths for the flat and upright conformations, which are critical for the structure of the adsorbed films. Moreover, in our MD simulations typically 80% or more molecules stably adsorb on the surfaces (the value of SA1 in Figure A-5), demonstrating that the surface interactions are sufficiently strong. Therefore, we believe that the findings in this study will not change even if using stronger interaction energies as in the QM calculations.
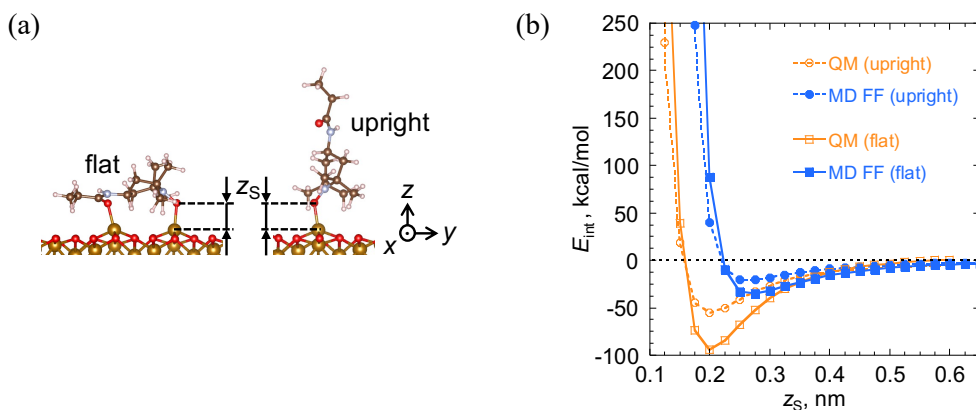
Figure 4-3 (a) Models for calculation of interaction energies between C_3TEMPO and Fe_2O_3 (001) surface. Flat and upright conformations of C_3TEMPO, which lead to double and single-site adsorption, respectively, were used. The red, white, brown, blue, and yellow represent oxygen, hydrogen, carbon, nitrogen, and iron atoms, respectively. (b) Comparison of interaction energies between the QM calculations and MD force field.

4.3.2 Comparison of Adsorption Energy of C_3TEMPO and Conventional OFMs

Table 4-4 compares the adsorption energy of C_3TEMPO, hexanoic acid [121] [HA: $CH_3(CH_2)_4COOH$, main chain reduced stearic acid], and glycerol monohexanate [121] [GMH: $CH_3(CH_2)_4COOCH_2CHOHCH_2OH$, main chain reduced glycerol monooleate] on Fe_2O_3 (001) surface obtained from the QM calculations. Here the adsorption energy is defined as the interaction energy at the equilibrium distance, as seen in Figure 4-3(b). For the three OFMs, the flat conformation leads to stronger surface adsorption than the upright one. For the flat conformation, the adsorption energy of C_3TEMPO is 1.7 and 1.3 times larger than those of HA and GMH; for the upright conformation, the adsorption energy of C_3TEMPO is slightly larger than that of HA but slightly smaller than that of GMH.

Table 4-4 Adsorption energies (kcal/mol) of C_3TEMPO, HA and GMH on Fe_2O_3 (001) surface obtained from QM calculations.

	Flat	Upright	Δ
C_3TEMPO	−94.0	−55.7	38.3
HA	−54.7	−49.6	5.10
GMH	−73.6	−60.7	12.9

4.3.3 Structure of Boundary Films

The structure of boundary films formed by OFM molecules largely determines the friction and wear reduction performance in the boundary lubrication regime. Hence, we first examined the snapshot of the MD simulations at the final timestep to qualitatively understand the structure of the boundary films formed by C_{12}TEMPO. As shown in Figure 4-4, to distinguish the individual C_{12}TEMPO molecules, their terminal O• atoms are indicated with a large red sphere and all the PAO molecules are omitted. Significantly different from the initial structure shown in Figure 4-1(c), during steady sliding O• atoms are not located only on the solid surfaces, but are distributed within a certain distance from the solid surfaces. This indicates that C_{12}TEMPO molecules can form multi-layer structured boundary films. Besides, the alkyl chains of C_{12}TEMPO molecules are randomly oriented even at the high concentration (Figure A-1), which is different from the regular perpendicular orientation suggested by the Hardy model for conventional OFMs [33,158].
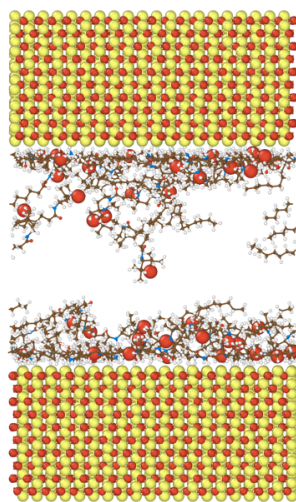
Figure 4-4 Front-view snapshot at the final timestep. For easy observation of the structure of the boundary films, only the iron oxide substrates and C_{12}TEMPO molecules are shown. The large red spheres represent the terminal O• atom of C_{12}TEMPO.

Then, to quantitatively analyze the structure of the adsorbed boundary films, particularly the number of layers, we calculated the number density profile of O• atoms, $\rho(z)$, with

$$\rho(z) = \frac{\langle n(z) \rangle}{A dz} \tag{4-2}$$

where and hereafter the brackets denote the time average over the last 10 ns of the simulations, z is the distance from the lower surface, $n(z)$ is the number of O• atoms in the region of $[z, z + \mathrm{d}z)$, A is the surface area of one substrate, and $\mathrm{d}z$ was set to 0.02 nm. The result is presented in Figure 4-5(a). Because $\rho(z)$ exhibits nearly the same characteristics in the vicinity of the lower and upper substrates, we focus the following description on $\rho(z)$ at $z \in [0,2]$ nm, i.e., $\rho(z)$ in the lower half region. Three peaks, noted as P_{O1}, P_{O2}, and P_{O3}, are observed at $z = 0.26$, 0.50, and ~0.90 nm, respectively. Because the positions of P_{O1} and P_{O2} are lower and the position of P_{O3} is higher than the maximum height (approximately 0.6 nm) of one C_{12}TEMPO molecule lying flat on the substrates, P_{O1} and P_{O2} should belong to the first layer and P_{O3} to the second layer of the boundary film. As shown in Figure 4-5(b), when the cyclic group of C_{12}TEMPO adopts the boat or chair conformation, the O• atom is located at 0.25 or 0.48 nm from the surface, which correspond well to the locations of P_{O1} or P_{O2}, respectively. Therefore, we conclude that the change in conformation of the cyclic group results in the two peaks in the first layer, and the boundary films are composed of two layers. Considering that the valley between P_{O2} and P_{O3} is located at 0.62 nm, we defined the C_{12}TEMPO molecules with O• atoms located in [0,0.62] nm from the surfaces as in the first layer and in (0.62,1.24] nm as in the second layer, as indicated by the broken and dotted lines in Figure 4-5(a).
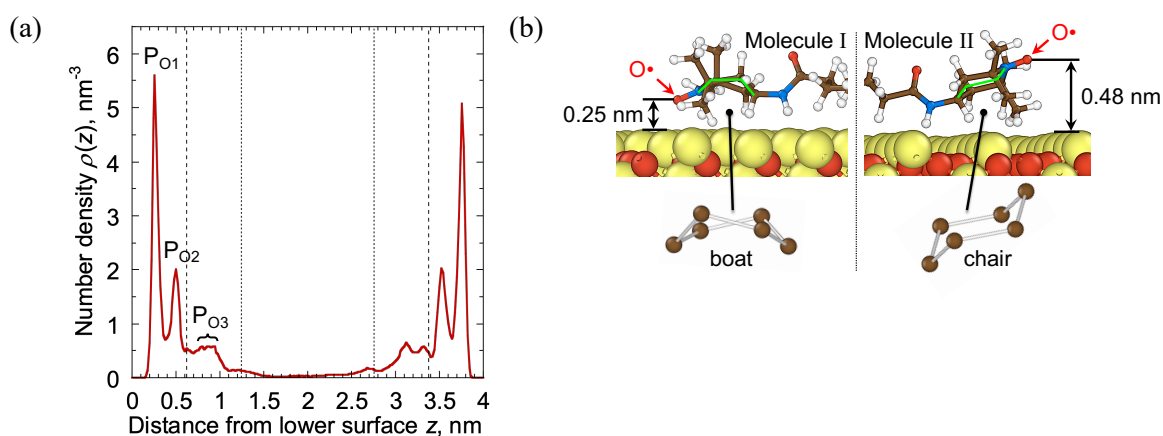
Figure 4-5 (a) Number density profile of O• atoms in C_{12}TEMPO molecules. The upper solid surface is located at $z = 4.0$ nm. Broken and dotted lines indicate the boundaries of the first and second layers, respectively. (b) Snapshots for two C_{12}TEMPO molecules in the first layer on the iron oxide surfaces. The cyclic group exhibits the boat (left figure) and chair (right figure) conformations, as indicated by the green lines. For reference, the boat and chair conformations of cyclohexane are also schematically illustrated below the snapshots.

4.3.4 Formation of the Structure of Boundary Films

4.3.4.1 Formation of the First Layer

To understand how the first layer is formed, we analyzed the adsorption state of C_{12}TEMPO molecules on the solid surfaces. Because C_{12}TEMPO adsorbs on Fe_2O_3 (001) surfaces mainly through $O\bullet$ and O_{amide} (the amide oxygen) atoms [Figure 4-3(a)], there are six adsorption states depending on the surface adsorption strengths of $O\bullet$ and O_{amide} atoms. These adsorption states include one type of strong double-site adsorption (DSs), three types of weak double-site adsorption (DSw-a, DSw-o, and DSw-ao), and two types of single-site adsorption (SSs and SSw). For DSs, both $O\bullet$ and O_{amide} adsorb strongly on the surfaces; for DSw-a, O_{amide} adsorbs weakly while $O\bullet$ strongly on the surfaces; for DSw-o, $O\bullet$ adsorbs weakly while O_{amide} strongly on the surfaces; for DSw-ao, both $O\bullet$ and O_{amide} adsorb weakly on the surfaces; and for SSs and SSw, only $O\bullet$ adsorbs strongly or weakly on the surfaces. Note that there is no single-site adsorption via O_{amide} for C_{12}TEMPO molecules in the first layer because only the molecules with strongly or weakly adsorbed $O\bullet$ atoms, which are located within 0.62 nm from the solid surfaces, were defined as in the first layer.

To determine the adsorption state of individual C_{12}TEMPO molecules, we set thresholds to distinguish whether the surface adsorption of $O\bullet$ and O_{amide} is strong or weak, according to the characteristic distances observed from the density profiles of $O\bullet$ and O_{amide} and the surface interaction strength at those distances. At the characteristic distances of 0.38 and 0.62 nm for $O\bullet$ [Figure 4-5(a)], the surface interaction strength is −10.4 and −2.4 kcal/mol [Figure 4-3(b)], 13 and 3 times larger than the thermal energy (0.78 kcal/mol) at 393 K, respectively. Hence, $O\bullet$ atoms located in (0,0.38] nm from the surfaces were defined as strongly adsorbed, in (0.38,0.62] nm as weakly adsorbed, and beyond 0.62 nm as non-adsorbed. To find the characteristic distances for O_{amide}, we calculated the number density profiles of O_{amide} in C_{12}TEMPO molecules with strongly or weakly adsorbed $O\bullet$ atoms. The results are shown in Figure 4-6. Because the DFT calculations suggested that O_{amide} and $O\bullet$ are located at an equal distance from the surfaces for the most stable adsorbed structure of C_{12}TEMPO molecules [139], 0.40 nm was selected as one characteristic distance for O_{amide}, which is close to 0.38 nm for $O\bullet$. The other characteristic distance was selected to be 0.50 nm because beyond this distance both the number density and its variation are small. Thus, O_{amide} atoms located in (0,0.40] nm from the surfaces were defined as

strongly adsorbed, in (0.40,0.50] nm as weakly adsorbed, and beyond 0.50 nm as non-adsorbed. Finally, we can judge the adsorption state of individual C_{12}TEMPO molecules based on the distances of O• and O_{amide} from the solid surfaces, as listed in Table 4-5.

(a)   (b)
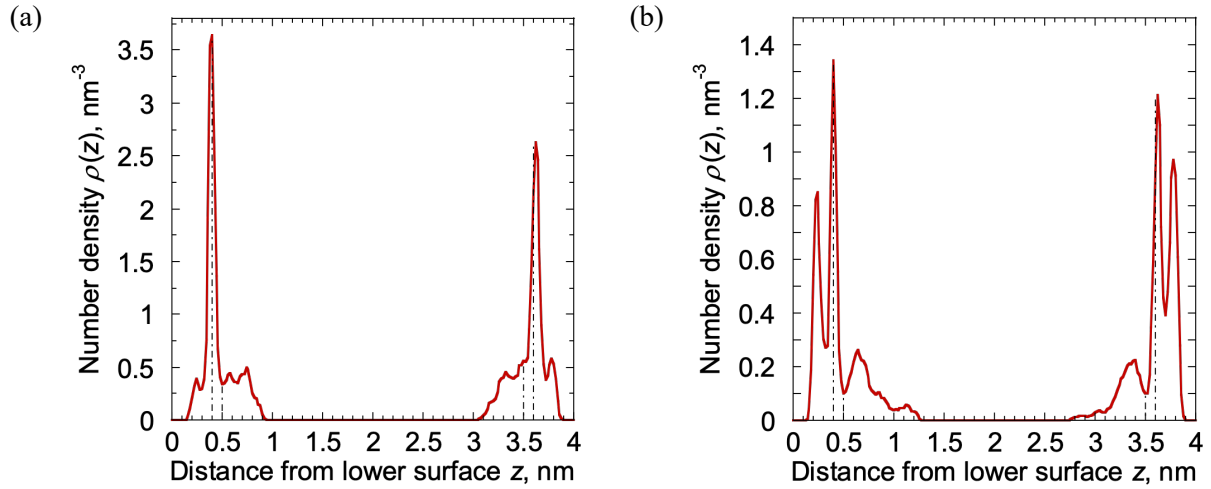
Figure 4-6 Number density profiles of O_{amide} atoms in C_{12}TEMPO molecules with (a) strongly adsorbed O• atoms and (b) weakly adsorbed O• atoms.

Table 4-5 Definition of adsorption states of C_{12}TEMPO molecules in the first layer of the boundary films on Fe_2O_3 (001) surfaces.

Distance from surfaces (nm)		O•	
		(0,0.38] (strong)	(0.38,0.62] (weak)
O_{amide}	(0,0.40] (strong)	DSs	DSw-o
	(0.40,0.50] (weak)	DSw-a	DSw-ao
	> 0.50 (non)	SSs	SSw

Figure 4-7 shows the probability of occurrence of each adsorption state for C_{12}TEMPO molecules in the first layer. The strong double-site adsorption (DSs) and weak double-site adsorption (DSw-a +

DSw-o + DSw-ao) account for 34 and 39%, respectively. All the double-site adsorption (DSs + DSw-a + DSw-o + DSw-ao) accounts for 73%, roughly three times more than the single-site adsorption (SSs + SSw) of 27%. Even for the high concentration, this ratio still accounts for 63% at 393 K (Figure A-4 in the Appendix Section). This demonstrates that C_{12}TEMPO molecules in the first layer are more likely to have their rigid six-membered ring being anchored at two opposite ends to the iron oxide surfaces by the amide group and terminal oxygen radical; i.e., the head groups are more likely to lie flat than stand upright on the iron oxide surfaces [see Figure 4-3(a) for the flat and upright conformations]. As described in detail in Sections 4.3.1.2 and 4.3.2, the DFT calculations showed that, for C_3TEMPO, hexanoic acid [121] (main chain reduced stearic acid), and glycerol monohexanate [121] (main chain reduced glycerol monooleate), the surface adsorption energy for the flat conformation is 38.3, 5.10 and 12.9 kcal/mol stronger than that for the upright conformation (Table 4-4). The energy difference is the largest for C_3TEMPO. This confirms that, compared with stearic acid and GMO, C_{12}TEMPO is energetically more likely to adsorb on the solid surfaces with its head group lying flat.
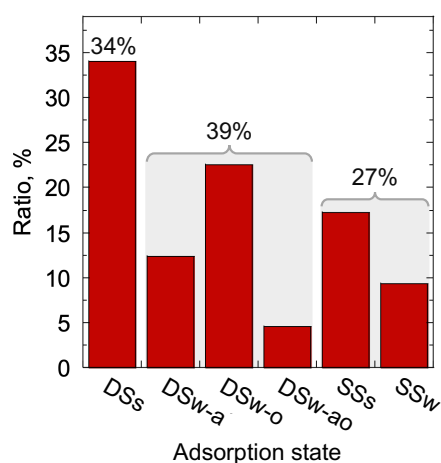
Figure 4-7 Probability of occurrence of different adsorption states for C_{12}TEMPO in the first layer.

4.3.4.2 Formation of the Second Layer

To understand how the second layer is formed, we focused on the interactions between C_{12}TEMPO molecules in the first and second layers. The two functional groups in C_{12}TEMPO can give rise to strong interlayer interactions through hydrogen-bonding of either $O\bullet$–H_{amide} or O_{amide}–H_{amide}, where H_{amide} represents the amide hydrogen. To judge the formation of the hydrogen bonds during sliding, we defined a critical bond length according to the characteristic distances observed from the radial distribution

functions (RDFs) of $O\bullet-H_{amide}$ and $O_{amide}-H_{amide}$ (Figure 4-8) and the interaction strengths at those distances (Figure 4-9). To derive the RDFs, bulk simulations with NVT ensemble at 0.5 GPa were performed with 60 C_{12}TEMPO molecules for 10.5 ns. The results show that for both $O\bullet-H_{amide}$ and $O_{amide}-H_{amide}$ the first peak of RDFs ends at the distance of 0.3 nm, where the interaction energy is -5.8 and -5.0 kcal/mol for $O\bullet-H_{amide}$ and $O_{amide}-H_{amide}$, approximately 8 and 7 times larger than the thermal energy (0.78 kcal/mol) at 393 K. Hence, 0.3 nm was used as the critical bond length.

The ratio of C_{12}TEMPO molecules that form interlayer hydrogen-bonding was quantified with

$$\alpha_{21} = \frac{\langle n_{H21}\rangle}{\langle N_2\rangle} \times 100\% \tag{4-3}$$

where n_{H21} is the number of the second-layer C_{12}TEMPO molecules that are hydrogen-bonded to the first-layer molecules, and N_2 is the total number of C_{12}TEMPO molecules in the second layer. α_{21} was calculated to be 32%. It is interesting to note that, at an arbitrary time during steady sliding, while 32% of the C_{12}TEMPO molecules in the second layer are hydrogen-bonded to the first layer, the other 68% remain in the second layer even though they are not hydrogen-bonded. This suggests that the hydrogen bonds are relatively weak and can be broken by shear, and thus C_{12}TEMPO molecules in the second layer are intermittently rather than permanently bonded to the first layer during sliding. Nevertheless, when the interlayer hydrogen bonds are broken, C_{12}TEMPO molecules in the second layer can quickly form new hydrogen-bonding with other C_{12}TEMPO molecules in the first layer during relative motion in the horizontal direction induced by the shear of the solid surfaces. As a result, these molecules can remain in rather than escape outside the second layer. Thus, we infer that the formation of the second layer in the boundary film of C_{12}TEMPO is attributable to the intermittent interlayer hydrogen-bonding.
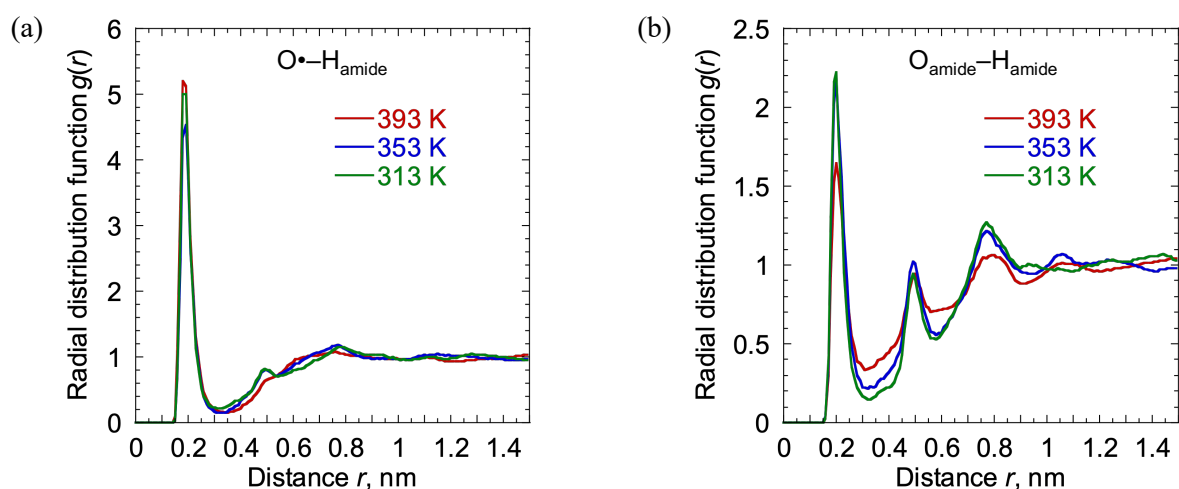
Figure 4-8 Radial distribution function for (a) $O\bullet–H_{amide}$ and (b) $O_{amide}–H_{amide}$.
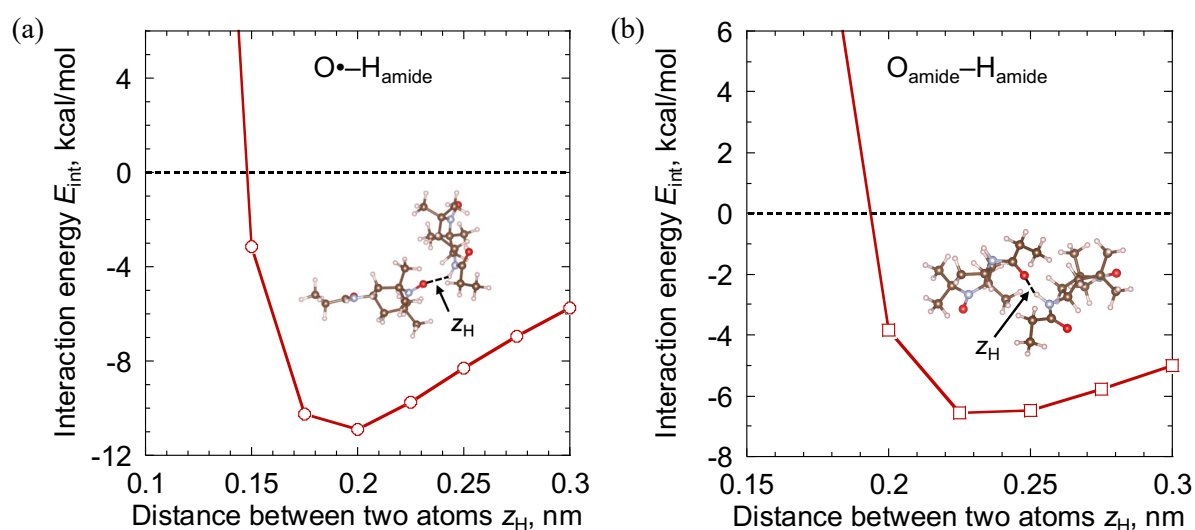
Figure 4-9 PES scans of (a) $O\bullet–H_{amide}$ and (b) $O_{amide}–H_{amide}$ interactions calculated with the COMPASS II force field.

4.3.4.3 Formation of Intralayer Hydrogen Bonding

In addition to the interlayer hydrogen-bonding, intralayer hydrogen-bonding was also analyzed to understand the bonding state of C_{12}TEMPO molecules in each of the first and second layers. The ratios of the C_{12}TEMPO molecules that form intralayer hydrogen-bonding in the first and second layers were quantified with α_{11} and α_{22}, respectively,

$$\alpha_{11} = \frac{\langle n_{H11} \rangle}{\langle N_1 \rangle} \times 100\% \qquad (4\text{-}4)$$

$$\alpha_{22} = \frac{\langle n_{H22} \rangle}{\langle N_2 \rangle} \times 100\% \qquad\qquad (4\text{-}5)$$

where n_{H11} and n_{H22} are the number of hydrogen-bonded C_{12}TEMPO molecules in each of the first and second layers, respectively, and N_1 is the total number of C_{12}TEMPO molecules in the first layer.

α_{11} was calculated to be 46%. As the C_{12}TEMPO molecules in the first layer adsorb either strongly or weakly on the solid surfaces according to our definition, the value of α_{11} indicates that 46% of the first-layer C_{12}TEMPO molecules are hydrogen-bonded to each other while adsorbing on the surfaces. α_{22} was calculated to be 41%, comparable to the value of α_{11}. We also confirmed that the second-layer C_{12}TEMPO molecules that form both interlayer and intralayer hydrogen-bonding account for 3%. Along with the interlayer hydrogen-bonding, the intralayer hydrogen-bonding, which can constrain C_{12}TEMPO molecules to the second layer, is also beneficial for the formation of the second layer. As was described in Section 1, the strength of the OFM boundary films is determined not only by the surface adsorption strength but also by the cumulative cohesion strength. For conventional OFMs, the cumulative cohesion strength originates from the van der Waals interactions between the alkyl chains of adsorbed OFMs [35,159,160]. The intralayer and interlayer hydrogen-bonding interactions between C_{12}TEMPO molecules are roughly one order stronger than the van der Waals interactions and thus can more effectively enhance the cohesion strength of the C_{12}TEMPO boundary films.

4.3.5 Dynamic Behavior of Boundary Films During Sliding

4.3.5.1 Velocity Distribution

To understand the motion of C_{12}TEMPO molecules during sliding, we analyzed their velocity distribution. The result is shown in Figure 4-10. The velocity profile of the liquid lubricants (i.e., both C_{12}TEMPO and PAO molecules) is also shown for comparison. Note that the velocity profile of C_{12}TEMPO in the central layer is statistically meaningless because of the extremely low density. In the first and second layers, the C_{12}TEMPO molecules show nearly the same velocities as the liquid lubricants. In the first layer, the velocity nearly equals to the sliding velocity of the adjacent surface and the velocity gradient is approximately zero. These indicate that the C_{12}TEMPO molecules in the first layer behaves like solid. In the second layer, the velocity gradient is not zero, but it is evidently smaller

than that in the central layer. These indicate that the $C_{12}TEMPO$ molecules in the second layer behave like liquid [89], but the apparent viscosity is larger than that of the liquid lubricants in the central layer. For most conventional OFMs, while the solid-like behavior of the first layer is common, the liquid-like behavior of the second layer has not been reported to our knowledge [33,96,161].
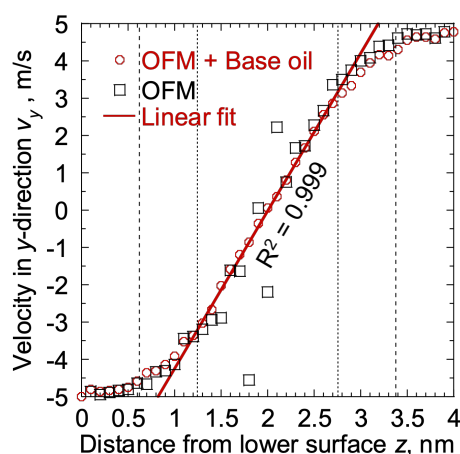
Figure 4-10 Velocity profiles of $C_{12}TEMPO$ molecules (OFM) and liquid lubricants (OFM + Base oil). The straight line is the linear fit to the velocities of the liquid lubricants in the central layer. Broken and dotted lines indicate the boundaries of the first and second layers, respectively.

4.3.5.2 Stability of Adsorption

To gain insight into the dynamic adsorption behavior, we analyzed the adsorption stability of individual $C_{12}TEMPO$ molecules. The adsorption stability was defined as follows. If the velocity difference in the y direction between the $C_{12}TEMPO$ molecules and solid surfaces is no larger than 0.5 m/s, then the $C_{12}TEMPO$ molecules are defined as stably adsorbed; otherwise, if the velocity difference is larger than 0.5 m/s and the difference lasts more than 80 ps (see below for the reason), then the $C_{12}TEMPO$ molecules are defined as unstably adsorbed. For distinction, the stably adsorbed molecules in the first and the upper layers are referred to as SA1 and SA2, respectively.

Here, 80 ps was used in the judgement of adsorption is because, as one example, Figure 4-11 shows the histogram for the duration time of unstable adsorption derived from the data in the last 10 ns for the medium concentration at 393 K. The duration time was calculated according to the judgment of stable or unstable adsorption for all the $C_{12}TEMPO$ molecules at every 2 ps. Note that here unstable adsorption was defined as if the velocity difference in the y direction between the $C_{12}TEMPO$ molecules and solid surfaces is larger than 0.5 m/s. A peak is seen for duration time of 0–80 ps as indicated in red, which

accounts for 19.4% of the total. This peak is largely dependent on the sampling time and can induce statistical uncertainty for the number of SA1 and SA2. Therefore, we added a critical time for unstable adsorption, i.e., unstable adsorption was finally defined as if the velocity difference larger than 0.5 m/s lasts more than 80 ps.
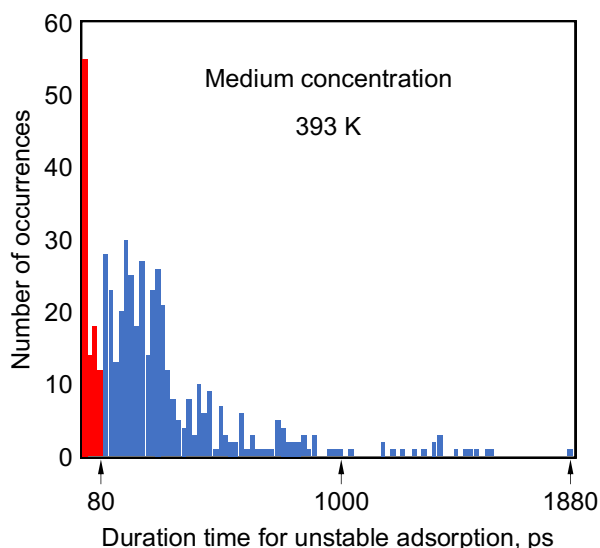
Figure 4-11 Histogram for duration time of unstable adsorption. The red indicates the duration time no longer than 80 ps.

We found that, in average over the last 10 ns, SA1 and SA2 account for 77% and 39% of the molecules in the first and the upper layers, respectively. The large fraction of SA1 and the relatively small fraction of SA2 demonstrate again that the first and second layers are solid and liquid-like, respectively. It is noteworthy that transition between SA1, SA2, and unstable adsorption is observed for individual C_{12}TEMPO molecules. Figure 4-12 shows such transition in the last 10 ns for four C_{12}TEMPO molecules, which represent all the typical dynamic behaviors observed in our simulations. The transition of SA1 and SA2 to and from unstable adsorption is seen in Figure 4-12(a) and (b), respectively. Compared with SA1, SA2 exhibits shorter lifetime and more frequent transition to and from unstable adsorption. This also demonstrates that the molecules in the second layer are easier to move in the sliding direction than those in the first layer. From Figure 4-12(c) and (d) transition between SA1 and SA2 is also observed. Such transition is associated with the self-repair of the boundary films, which will be described in detail below.
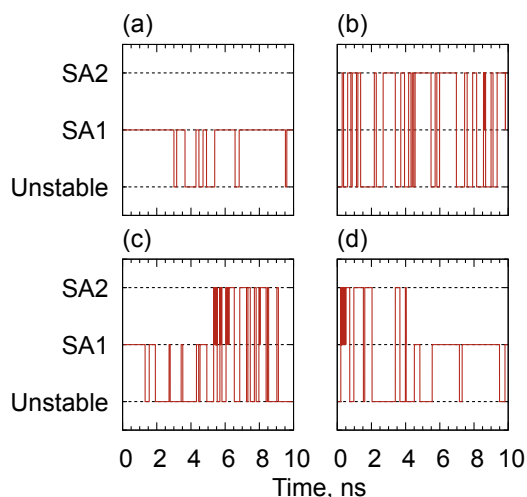
Figure 4-12 Transition between adsorption states of C_{12}TEMPO molecules.

4.3.5.3 Self-Repair of Boundary Films

As observed from our simulations, when flowing on the first layer, the second-layer C_{12}TEMPO molecules can be captured by the first-layer molecules through the interlayer hydrogen-bonding and then be pulled down to the first layer by the surface interactions. This behavior is referred to as self-repair of the boundary films. Figure 4-13 shows snapshots illustrating the dynamic process of the self-repair at the medium concentration and 393 K. For clarity, only the two C_{12}TEMPO molecules involved in the process and a part of the solid surface are shown. At 18.140 ns, molecule I in the first layer adsorbed on the solid surface, and molecule II was in the second layer with its head group located at a little distance away from that of molecule I. Then, molecule II moved due to the shear of solid surfaces and its O• atom approached to the amide group of molecule I at 18.962 ns. Subsequently at 19.274 ns, the distance between the O• atom in molecule II and the H_{amide} atom in molecule I was as small as 0.19 nm and thus the two molecules were hydrogen-bonded to each other. At 19.958 ns, molecule II captured by molecule I was finally pulled to adsorb onto the solid surface by the surface interactions. These results demonstrate the important role of the interlayer hydrogen-bonding for self-repair of the C_{12}TEMPO boundary films. That is, when C_{12}TEMPO molecules desorb from the surface and move to the second layer, they can rapidly re-adsorb onto the surface to repair the depleted area owing to the hydrogen bonds developed between the first and second layers.

70
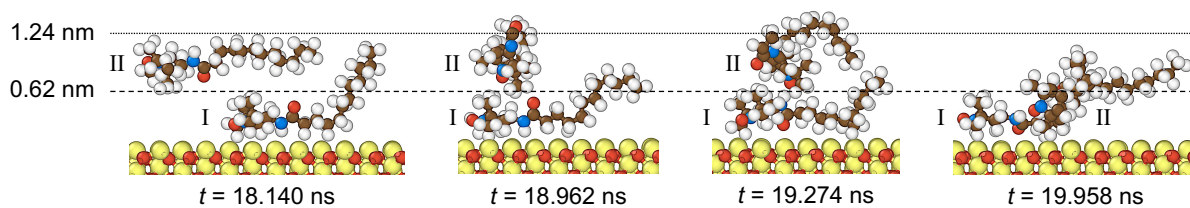
Figure 4-13 A typical self-repair process of C$_{12}$TEMPO boundary films at the medium concentration and 393 K. Only two C$_{12}$TEMPO molecules (I and II) and a part of the lower substrate are shown for clarity. The yellow, red, white, brown, and blue represent iron, oxygen, hydrogen, carbon, and nitrogen atoms, respectively.

4.3.6 Discussion on the Correlation Between Adsorption Behavior and Friction and Wear-Reducing Performance

Different from conventional OFMs, which usually have one functional group or multiple functional groups of the same type, C$_{12}$TEMPO molecules are characterized by two functional groups of different types, i.e., the terminal oxygen radical and amide group. As is illustrated in Figure 4-14, such molecular structure allows for multi-type surface adsorption and also intermolecular hydrogen-bonding, thereby resulting in adsorbed boundary films with a double-layer structure similar to the electric double layer. In the first layer, as shown in brown color, a large fraction of C$_{12}$TEMPO molecules adsorb on the solid surfaces via the two functional groups, exhibiting double-site adsorption states (DSs, DSw-o, DSw-a, DSw-ao), and a small fraction adsorb via only the terminal oxygen radical, exhibiting single-site adsorption states (SSs, SSw). As shown in red color, some C$_{12}$TEMPO molecules do not directly adsorb on the solid surfaces; however, they are bonded to the C$_{12}$TEMPO molecules in the first layer via interlayer hydrogen-bonding (indicated with black dotted lines) of O•–H$_{amide}$ or O$_{amide}$–H$_{amide}$, forming the second layer. Moreover, intralayer hydrogen-bonding also forms in each of the first and second layers, as illustrated in Figure 4-14(b).

Our previous studies experimentally demonstrated that C$_{12}$TEMPO exhibits higher load-carrying capacity, wear-reducing effect, and stability of friction than the conventional OFMs of stearic acid and GMO [138,139]. All of these superior tribological properties suggest that the boundary films of C$_{12}$TEMPO remain effective at preventing solid–solid contacts even under heavily loaded and prolonged sliding. As was described in Section 4.1, the effectiveness of boundary films is governed not only by

71
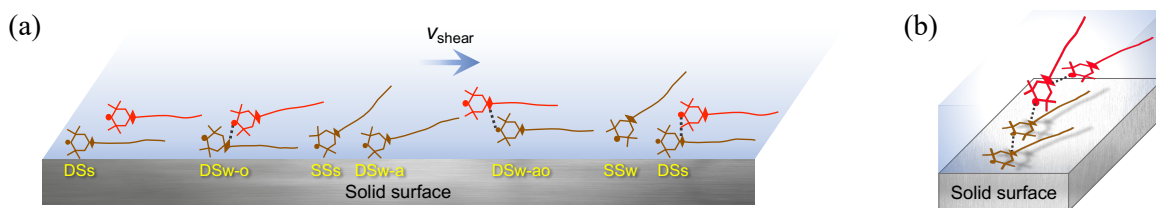
Figure 4-14 Schematic model for (a) multi-type adsorption of C_{12}TEMPO and (b) intralayer and interlayer hydrogen-bonding. Note that the molecular structure of C_{12}TEMPO is simplified for clarity. The circle, hexagon, rhombus, and curve represent the oxygen radical, cyclic head, amide group, and alkyl chain, respectively. The brown and red indicate molecules in the first and second layers, respectively. Black dotted lines represent hydrogen-bonding.

film strength but also by adsorption kinetics. High film strength makes it difficult for the boundary films to be sheared off from solid surfaces. However, as the normal load or shear stress increases, the boundary films can still be removed from the surfaces. Self-repair of the boundary films through rapid re-adsorption is thus crucial, as suggested by recent experimental studies [23,124,129]. Even under heavily loaded and prolonged sliding, if the repair rate constant (determined by adsorption kinetics) is no smaller than the removal rate constant (determined by film strength), the boundary films can keep dynamically stable rather than eventually wear out. Therefore, we suggest that the superior tribological properties of C_{12}TEMPO are attributed to the unique features of the C_{12}TEMPO boundary films that make the films difficult to be removed and easy to repair quickly as compared with conventional OFMs. The details are discussed below.

First, let us discuss why the C_{12}TEMPO boundary films are difficult to be removed. Because a large fraction (73% for the medium concentration at 393 K) of C_{12}TEMPO molecules in the first layer exhibit double-site adsorption, the surface adsorption strength of the first layer should be strong. In addition to the surface interactions, a fraction (46% for the medium concentration at 393 K) of the molecules in the first layer also form intralayer hydrogen-bonding, which is one order stronger than van der Waals interactions, thereby resulting in fewer conformational defects and stronger cohesion of the first layer [162]. The strong adsorption and cohesion are believed to synergistically enhance the strength of the first layer. Moreover, the first layer is covered by the liquid-like second layer. A fraction (41% for the medium concentration at 393 K) of the molecules in the second layer are hydrogen-bonded to each other, rendering the second layer more viscous than the base oil as seen from the smaller velocity gradient in

Figure 4-10. The viscous second layer could act as an effective buffer for the first layer against shear. As a result, the first layer of the C_{12}TEMPO boundary films, which is the last barrier to prevent solid–solid contacts, is difficult to be removed as compared with conventional OFMs. This feature is also well demonstrated by the solid-like behavior observed from the nearly zero velocity gradient in Figure 4-10 and the large fraction (77% for the medium concentration at 393 K) of C_{12}TEMPO molecules that remain stably adsorbed on the solid surfaces during sliding.

The feature that the C_{12}TEMPO boundary films are easy to repair quickly is believed to result from the behavior of the second layer. The second layer forms owing to interlayer hydrogen-bonding. However, in contrast to the solid-like first layer, the second layer is liquid-like, as demonstrated by the non-zero velocity gradient in Figure 4-10, the relatively small fraction (39% for the medium concentration at 393 K) of the second-layer C_{12}TEMPO molecules that move at the same velocity as the solid surfaces, and the frequent transition between stable and non-stable adsorption [Figure 4-12(b)]. These suggest that the interlayer hydrogen-bonding is not permanent but intermittent. As a result, the molecules in the second layer move on the first layer in a stick-slip-like manner and repair the once depleted region in the first layer, as was illustrated in Figure 4-13. That is, the second layer can act as a reservoir to rapidly repair the first layer owing to the intermittent hydrogen-bonding with the first layer.

4.4 Conclusions

We performed MD simulations to gain molecular-level insights into the adsorption behavior of C_{12}TEMPO, a new type of OFM developed in our previous study, from PAO oil onto hematite surfaces during sliding. The results showed that, owing to the two functional groups of different types (i.e., the amide group and terminal oxygen radical), C_{12}TEMPO molecules exhibit multi-type adsorption and form boundary films with a double-layer structure, which are different from the single-type adsorption and single-layer structure reported for most conventional OFMs. In the first layer, C_{12}TEMPO molecules exhibit strong/weak double-site surface adsorption via the two functional groups or strong/weak single-site surface adsorption via the terminal oxygen radical. The second layer forms because some C_{12}TEMPO molecules adsorb on the first-layer molecules through interlayer hydrogen-bonding of O•–H_{amide} and O_{amide}–H_{amide}. Additionally, intralayer hydrogen-bonding also forms in the first and second layers.

The results of velocity analysis showed that the first layer behaves as solid and stably adsorbs on the surfaces during sliding, whereas the second layer behaves as liquid with viscosity larger than the base oil and flows relative to the first layer during sliding. We suggest that the reasons why the first layer is hard to be sheared off lie on strong surface adsorption, strong cohesion due to the intralayer hydrogen-bonding, and the buffer effect of the viscous second layer. From the simulation snapshots, we also found that, when flowing on the first layer, the second-layer molecules can be captured by the first-layer molecules through the interlayer hydrogen-bonding and then be pulled down to the first layer by the surface interactions. This indicates that the second layer can act as a reservoir to quickly repair the once depleted region in the first layer. We suggest that the experimentally observed superior tribological properties of C_{12}TEMPO, i.e., high load-carrying capacity, high antiwear effect, and high stability of friction over time, are attributable not only to the durability of the first layer but also to the repair ability of the second layer. The unique structure and dynamic behavior of the boundary films found in this study provide new hints for the optimal molecular design of high-performance OFMs.

Chapter 5

Summary and Future Work

Reducing friction plays a pivotal role in conserving energy. In oil-based lubricant systems, boundary lubrication, which occurs within nanoscale gaps of two solid substrates, results in elevated friction coefficients. Thus, to achieve advanced mechanical systems that involve relative motion across nanoscale gaps, it is crucial to establish effective boundary lubrication through nanometer-thick liquid films to reduce friction. Effective nanometer-thick liquid boundary films require both high stability and high friction-reducing performance, encompassing stable adsorption ability, chemical stability, high load-carrying capacity, and low shear strength. In Chapter 1, we elucidated the importance of nanometer-thick liquid film boundary films and highlighted the persisting challenges they present in HDDs and vehicle powertrain systems. To address these challenges, we opted for MD simulations as the approach to investigate the chemical and physical behaviors exhibited by molecules within the boundary films.

To understand the chemical behavior of the nanometer-thick liquid films, we take the HAMR systems, a type of high-recording density HDDs, as the subject. In Chapter 2 and 3, we developed a new ReaxFF force field for PFPE molecules, which allows us to perform nonequilibrium reactive MD simulations to gain insights into mechano-chemical decomposition of nanometer-thick PFPE films at the HDI of HAMR. Our research confirmed that D-4OH molecules hardly react only at the high temperatures within the 1-ns 700 K heating time of HAMR. But once subjected to mechanical stress, D-4OH molecules are highly possible to react. Adding water can further promote the reactions at low normal pressures. We found that the most vulnerable bond in D-4OH molecules is the C–O bonds in the end groups, thus polar PFPE molecules tend to undergo more rapid decomposition compared to nonpolar PFPE molecules. Water primarily dissociates the C–O bonds in the end groups, while high normal pressures dissociate the C–O bonds in both the end groups and main chains. The effect of water on the dissociation of the C–OC bonds in the end groups is more significant compared to the C–OH bonds in the end groups, and both effects level off at higher normal pressures. We caution against extrapolating the linear stress-activated Arrhenius curve obtained at high normal pressures to low normal pressures, which could cause significant overestimation of decomposition rate constants at low normal pressures.

To understand the physical behavior of the nanometer-thick liquid films, we take OFM boundary films in vehicle powertrain systems as the subject. In Chapter 4, we performed non-reactive MD simulations to gain molecular-level insights into the adsorption behavior of C_{12}TEMPO, a new type of TEMPO-based OFM developed in our previous study. The MD results provide us with insights into the underlying mechanism behind the remarkable tribological performance of C_{12}TEMPO, as observed in

experimental studies. These include its higher load-carrying capacity, higher wear-reducing effect, and more stable friction coefficient over time than the conventional OFMs of stearic acid and GMO. We found that C_{12}TEMPO molecules exhibit multi-type adsorption and form boundary films with a double-layer structure owing to the two functional groups of different types, which are different from the single-type adsorption and single-layer structure reported for most conventional OFMs. We suggest that the reasons why the first layer is hard to be sheared off lie on strong surface adsorption, strong cohesion due to the intralayer hydrogen-bonding, and the buffer effect of the viscous second layer. We also found that, when flowing on the first layer, the second-layer molecules can be captured by the first-layer molecules through the interlayer hydrogen-bonding and then be pulled down to the first layer by the surface interactions. This indicates that the second layer can act as a reservoir to quickly repair the once depleted region in the first layer. We suggest that the experimentally observed superior tribological properties of C_{12}TEMPO are attributable not only to the durability of the first layer but also to the repair ability of the second layer.

In conclusion, these works not only expand our understanding of the influence of heat, mechanical stress, and water on the chemical reactions occurring in nanometer-thick liquid films within HAMR systems, but also elucidate the mechanism behind the remarkable friction-reducing performance achieved by the formation of nanometer-thick liquid films through a novel TEMPO-based OFM. We expect these works will provide valuable insights for optimizing chemically stable lubricant molecules in HDI, thereby enhancing lubrication strategies in HAMR systems. Also, we expect these studies to offer novel insights for designing high-performance OFM with enhanced friction-reducing properties, thereby contributing to the reduction of friction in vehicle powertrain systems.

Meanwhile, we also notice that there are still some gaps that require further investigation and may serve as potential directions for future research, as outlined below.

First, in our research on HAMR systems, we did not take into account the catalytic effect of DLC on the reactions of PFPE molecules. In future investigations, we propose substituting the diamond substrates with DLC substrates to simulate the working conditions of HAMR more accurately. Furthermore, while we found that the terminal C–OH bonds of the PFPE lubricant molecules are susceptible to breaking under the influence of water and mechanical stress, the presence of the C–OH groups offers the advantage of anchoring PFPE molecules to disk surfaces. It is therefore imperative to devise strategies that reconcile these two aspects, which will be a future challenge.

Second, in our research on OFMs, the flat–flat MD model did not allow molecules to escape from the contact area, leading to less pronounced desorption behavior. To address this limitation, we suggest using semicylinder–flat or semispherical–flat MD models. These models allocate space for liquid molecules to escape from the contact area, enabling a more realistic exploration of the desorption behaviors of OFM molecules during shearing. Additionally, our study focused on oil-based lubricating systems, which have low permittivity. In such circumstances, the intermolecular interactions between polar functional groups in OFMs are sufficiently strong to sustain the boundary films and form the two layers. In future research, exploring the physical behaviors of OFMs in high permittivity environments, such as in water-based lubrication systems, where interactions between polar functional groups are weak, could offer a more comprehensive understanding of the molecular design of OFMs.

Reference

[1]   International Energy Agency. Energy Technology Perspectives 2010. Scenarios & Strategies to 2050. https://iea.blob.core.windows.net/assets/04776631-ea93-4fea-b56d-2db821bdad10/etp2010.pdf (accessed 2021-11-23).

[2]   Holmberg, K.; Erdemir, A. Influence of Tribology on Global Energy Consumption, Costs and Emissions. *Friction* **2017**, *5*, 263–284.

[3]   Roddick, E.; Kief, M.; Takeo, A. A New Advanced Storage Research Consortium HDD Technology Roadmap. In *2022 IEEE 33rd Magnetic Recording Conference (TMRC)*; IEEE: Milpitas, CA, USA, 2022; pp 1–2.

[4]   Kryder, M. H.; Gage, E. C.; McDaniel, T. W.; Challener, W. A.; Rottmayer, R. E.; Ju, G. Heat Assisted Magnetic Recording. *Proc. IEEE* **2008**, *96*, 1810–1835.

[5]   Fowler, D. E.; Geiss, R. H. Chemical Contamination at the Head–Disk Interface in a Disk Drive. *IEEE Trans. Magn.* **2000**, *36*, 133–139.

[6]   Suzuki, I.; Takahashi, Y. K. Grain Density Control in FePt Granular Films for Heat-Assisted Magnetic Recording Media. *Jpn. J. Appl. Phys.* **2023**, *62*, SB0801.

[7]   Marchon, B.; Pitchford, T.; Hsia, Y.-T.; Gangopadhyay, S. The Head–Disk Interface Roadmap to an Areal Density of 4 Tbit/in^2. *Adv. Tribol.* **2013**, *2013*, 1–8.

[8]   Rajauria, S.; Ruiz, O.; Canchi, S. V.; Schreck, E.; Dai, Q. Electrostatically Tunable Adhesion in a High Speed Sliding Interface. *Phys. Rev. Lett.* **2018**, *120*, 026101.

[9]   Kiely, J. D.; Jones, P. M.; Hoehn, J. Materials Challenges for the Heat-Assisted Magnetic Recording Head-Disk Interface. *MRS Bull.* **2018**, *43*, 119–124.

[10]   Mendez, A. R.; Bogy, D. B. Lubricant Flow and Accumulation on the Slider's Air-Bearing Surface in a Hard Disk Drive. *Tribol. Lett.* **2014**, *53*, 469–476.

[11]   Sonoda, K. Flying Instability Due to Organic Compounds in Hard Disk Drive. *Adv. Tribol.* **2012**, *2012*, 1–6.

[12]   Weller, D.; Parker, G.; Mosendz, O.; Lyberatos, A.; Mitin, D.; Safonova, N. Y.; Albrecht, M. Review Article: FePt Heat Assisted Magnetic Recording Media. *J. Vac. Sci. Technol., B: Nanotechnol. Microelectron.: Mater., Process., Meas., Phenom.* **2016**, *34*, 060801.

[13]   Huang, L.; Stipe, B.; Staffaroni, M.; Juang, J.; Hirano, T.; Schreck, E.; Huang, F. HAMR Thermal Modeling Including Media Hot Spot. *IEEE Trans. Magn.* **2013**, *49*, 2565–2568.

[14]   Kiely, J. D.; Jones, P. M.; Yang, Y.; Brand, J. L.; Anaya-Dufresne, M.; Fletcher, P. C.; Zavaliche, F.; Toivola, Y.; Duda, J. C.; Johnson, M. T. Write-Induced Head Contamination in Heat-Assisted Magnetic Recording. *IEEE Trans. Magn.* **2017**, *53*, 1–

7.

[15] Xiong, S.; Wang, N.; Smith, R.; Li, D.; Schreck, E.; Dai, Q. Material Transfer Inside Head Disk Interface for Heat Assisted Magnetic Recording. *Tribol. Lett.* **2017**, *65*, 74.

[16] Ghahri Sarabi, M. S.; Bogy, D. B. Simulation of the Performance of Various PFPE Lubricants Under Heat Assisted Magnetic Recording Conditions. *Tribol. Lett.* **2014**, *56*, 293–304.

[17] Yang, Y.; Li, X.; Stirniman, M.; Yan, X.; Huang, F.; Zavaliche, F.; Wang, H.; Huang, J.; Tang, H.; Jones, P. M.; et al. Head-Disk Lubricant Transfer and Deposition During Heat-Assisted Magnetic Recording Write Operations. *IEEE Trans. Magn.* **2015**, *51*, 1–4.

[18] Fuel economy - Fuels & Technologies https://www.iea.org/fuels-and-technologies/fuel-economy (accessed 2023-05-31).

[19] Holmberg, K.; Andersson, P.; Erdemir, A. Global Energy Consumption Due to Friction in Passenger Cars. *Tribol. Int.* **2012**, *47*, 221–234.

[20] Spikes, H. Friction Modifier Additives. *Tribol. Lett.* **2015**, *60*, 5.

[21] Vaitkunaite, G.; Espejo, C.; Wang, C.; Thiébaut, B.; Charrin, C.; Neville, A.; Morina, A. MoS_2 Tribofilm Distribution from Low Viscosity Lubricants and Its Effect on Friction. *Tribol. Int.* **2020**, *151*, 106531.

[22] McQueen, J. S.; Gao, H.; Black, E. D.; Gangopadhyay, A. K.; Jensen, R. K. Friction and Wear of Tribofilms Formed by Zinc Dialkyl Dithiophosphate Antiwear Additive in Low Viscosity Engine Oils. *Tribol. Int.* **2005**, *38*, 289–297.

[23] Cyriac, F.; Tee, X. Y.; Poornachary, S. K.; Chow, P. S. Influence of Structural Factors on the Tribological Performance of Organic Friction Modifiers. *Friction* **2021**, *9*, 380–400.

[24] Allen, C. M.; Drauglis, E. Boundary Layer Lubrication: Monolayer or Multilayer. *Wear* **1969**, *14*, 363–384.

[25] Tang, Z.; Li, S. A Review of Recent Developments of Friction Modifiers for Liquid Lubricants (2007–Present). *Curr. Opin. Solid State Mater. Sci.* **2014**, *18*, 119–139.

[26] Bowden, F. P.; Tabor, D. *The Friction and Lubrication of Solids*; Clarendon Press: Oxford, 1971.

[27] Meng, Y.; Xu, J.; Jin, Z.; Prakash, B.; Hu, Y. A Review of Recent Advances in Tribology. *Friction* **2020**, *8*, 221–300.

[28] Zhou, Y.; Qu, J. Ionic Liquids as Lubricant Additives: A Review. *ACS Appl. Mater. Interfaces* **2017**, *9*, 3209–3222.

[29] De Barros Bouchet, M. I.; Martin, J. M.; Avila, J.; Kano, M.; Yoshida, K.; Tsuruda, T.; Bai, S.; Higuchi, Y.; Ozawa, N.; Kubo, M.; Asensio, M. C. Diamond-like Carbon Coating under Oleic Acid Lubrication: Evidence for Graphene Oxide Formation in

Superlow Friction. *Sci. Rep.* **2017**, *7*, 46394.

[30] Sunqing, Q.; Junxiu, D.; Guoxu, C. A Review of Ultrafine Particles as Antiwear Additives and Friction Modifiers in Lubricating Oils. *Lubr. Sci.* **1999**, *11*, 217–226.

[31] Wong, V. W.; Tung, S. C. Overview of Automotive Engine Friction and Reduction Trends–Effects of Surface, Material, and Lubricant-Additive Technologies. *Friction* **2016**, *4*, 1–28.

[32] ゲーゲンマイケル; ダーキンウィリアム; 梅原亮二. 次世代パワートレイン向けの専用eフルード潤滑油・添加剤の進化. トライボロジスト **2023**, *68*, 79–85.

[33] Ewen, J. P.; Gattinoni, C.; Morgan, N.; Spikes, H. A.; Dini, D. Nonequilibrium Molecular Dynamics Simulations of Organic Friction Modifiers Adsorbed on Iron Oxide Surfaces. *Langmuir* **2016**, *32*, 4450–4463.

[34] Li, W.; Kumara, C.; Meyer, H. M.; Luo, H.; Qu, J. Compatibility between Various Ionic Liquids and an Organic Friction Modifier as Lubricant Additives. *Langmuir* **2018**, *34*, 10711–10720.

[35] Cyriac, F.; Yamashita, N.; Hirayama, T.; Yi, T. X.; Poornachary, S. K.; Chow, P. S. Mechanistic Insights into the Effect of Structural Factors on Film Formation and Tribological Performance of Organic Friction Modifiers. *Tribol. Int.* **2021**, *164*, 107243.

[36] Hirayama, T.; Kawamura, R.; Fujino, K.; Matsuoka, T.; Komiya, H.; Onishi, H. Cross-Sectional Imaging of Boundary Lubrication Layer Formed by Fatty Acid by Means of Frequency-Modulation Atomic Force Microscopy. *Langmuir* **2017**, *33*, 10492–10500.

[37] Guegan, J.; Southby, M.; Spikes, H. Friction Modifier Additives, Synergies and Antagonisms. *Tribol. Lett.* **2019**, *67*, 83.

[38] Zachariah, Z.; Nalam, P. C.; Ravindra, A.; Raju, A.; Mohanlal, A.; Wang, K.; Castillo, R. V.; Espinosa-Marzal, R. M. Correlation Between the Adsorption and the Nanotribological Performance of Fatty Acid-Based Organic Friction Modifiers on Stainless Steel. *Tribol. Lett.* **2020**, *68*, 11.

[39] Ratoi, M.; Niste, V. B.; Alghawel, H.; Suen, Y. F.; Nelson, K. The Impact of Organic Friction Modifiers on Engine Oil Tribofilms. *RSC Adv.* **2014**, *4*, 4278–4285.

[40] Schwartz, D. K. Mechanisms and Kinetics of Self-Assembled Monolayer Formation. *Annu. Rev. Phys. Chem.* **2001**, *52*, 107–137.

[41] Beltzer, M.; Jahanmir, S. Role of Dispersion Interactions Between Hydrocarbon Chains in Boundary Lubrication. *ASLE Trans.* **1987**, *30*, 47–54.

[42] Jahanmir, S. Chain Length Effects in Boundary Lubrication. *Wear* **1985**, *102*, 331–349.

[43] van Duin, A. C. T.; Dasgupta, S.; Lorant, F.; Goddard, W. A. ReaxFF: A Reactive Force Field for Hydrocarbons. *J. Phys. Chem. A* **2001**, *105*, 9396–9409.

[44] Chenoweth, K.; van Duin, A. C. T.; Goddard, W. A. ReaxFF Reactive Force Field for Molecular Dynamics Simulations of Hydrocarbon Oxidation. *J. Phys. Chem. A* **2008**,

112, 1040–1053.

[45]   Ashraf, C.; van Duin, A. C. T. Extension of the ReaxFF Combustion Force Field toward Syngas Combustion and Initial Oxidation Kinetics. *J. Phys. Chem. A* **2017**, *121*, 1051–1068.

[46]   Ashraf, C.; Shabnam, S.; Jain, A.; Xuan, Y.; van Duin, A. C. T. Pyrolysis of Binary Fuel Mixtures at Supercritical Conditions: A ReaxFF Molecular Dynamics Study. *Fuel* **2019**, *235*, 194–207.

[47]   Senftle, T. P.; Hong, S.; Islam, M. M.; Kylasa, S. B.; Zheng, Y.; Shin, Y. K.; Junkermeier, C.; Engel-Herbert, R.; Janik, M. J.; Aktulga, H. M.; et al. The ReaxFF Reactive Force-Field: Development, Applications and Future Directions. *npj Comput. Mater.* **2016**, *2*, 1–14.

[48]   Ewen, J. P.; Latorre, C. A.; Gattinoni, C.; Khajeh, A.; Moore, J. D.; Remias, J. E.; Martini, A.; Dini, D. Substituent Effects on the Thermal Decomposition of Phosphate Esters on Ferrous Surfaces. *J. Phys. Chem. C* **2020**, *124*, 9852–9865.

[49]   Plimpton, S. J.; Thompson, A. P. Computational Aspects of Many-Body Potentials. *MRS Bull.* **2012**, *37*, 513–521.

[50]   Ji, R.; Xu, J.; Liew, T.; Zhang, J.; Xie, H. Q.; Xu, B.; Dao, T. K. L. TOF-SIMS Analysis of Media Lubricant under Laser Irradiation for HAMR Application. *Surf. Interface Anal.* **2011**, *43*, 406–409.

[51]   Li, L.; Jones, P. M.; Hsia, Y.-T. Effect of Chemical Structure and Molecular Weight on High-Temperature Stability of Some Fomblin Z-Type Lubricants. *Tribol. Lett.* **2004**, *16*, 21–27.

[52]   Tani, H.; Shibahara, Y.; Lu, R.; Koganezawa, S.; Tagawa, N. TOF-SIMS Analysis of Perfluoropolyether Lubricant Smear Transferred from Disk Surface Following Laser Heating. *Microsyst. Technol.* **2020**, *26*, 79–88.

[53]   Murugesan, V.; Cho, J. S.; Govind, N.; Andersen, A.; Olszta, M. J.; Han, K. S.; Li, G.; Lee, H.; Reed, D. M.; Sprenkle, V. L.; et al. Lithium Insertion Mechanism in Iron Fluoride Nanoparticles Prepared by Catalytic Decomposition of Fluoropolymer. *ACS Appl. Energy Mater.* **2019**, *2*, 1832–1843.

[54]   Lotfi, R.; van Duin, A. C. T.; Biswas, M. M. Molecular Dynamics Simulations of Perfluoropolyether Lubricant Degradation in the Presence of Oxygen, Water, and Oxide Nanoparticles Using a ReaxFF Reactive Force Field. *J. Phys. Chem. C* **2018**, *122*, 2684–2695.

[55]   Helmick, L. S.; Jones, W. R. Determination of the Thermal Stability of Perfluoroalkylethers. *National Aeronautics and Space Administration* **1990**, NASA Technical Memorandum-102493.

[56]   Zhao, X.; Bhushan, B. Comparison Studies on Degradation Mechanisms of Perfluoropolyether Lubricants and Model Lubricants. *Tribol. Lett.* **2001**, *9*, 187–197.

[57] Tao, Z.; Bhushan, B. Degradation Mechanisms and Environmental Effects on Perfluoropolyether, Self-Assembled Monolayers, and Diamondlike Carbon Films. *Langmuir* **2005**, *21*, 2391–2399.

[58] Tao, Z.; Bhushan, B. Bonding, Degradation, and Environmental Effects on Novel Perfluoropolyether Lubricants. *Wear* **2005**, *259*, 1352–1361.

[59] Tanaka, K.; Kato, T.; Matsumoto, Y. Molecular Dynamics Simulation of Vibrational Friction Force Due to Molecular Deformation in Confined Lubricant Film. *J. Tribol.* **2003**, *125*, 587–591.

[60] Dai, L.; Sorkin, V.; Sha, Z. D.; Pei, Q. X.; Branicio, P. S.; Zhang, Y. W. Molecular Dynamics Simulations on the Frictional Behavior of a Perfluoropolyether Film Sandwiched between Diamond-like-Carbon Coatings. *Langmuir* **2014**, *30*, 1573–1579.

[61] Sorkin, V.; Sha, Z. D.; Branicio, P. S.; Pei, Q. X.; Zhang, Y. W. Atomistic Molecular Dynamics Study of Structural and Thermomechanical Properties of Zdol Lubricants on Hydrogenated Diamond-like Carbon. *IEEE Trans. Magn.* **2013**, *49*, 5227–5235.

[62] Nath, S. K. D.; Wong, C. H.; Sorkin, V.; Sha, Z. D.; Zhang, Y. W.; Kim, S. G. Study of the Spreading of Perfluoropolyether Lubricants on a Diamond-Like Carbon Film. *Tribol. Trans.* **2013**, *56*, 255–267.

[63] Li, B.; Wong, C. H.; Chen, Q. Kinetics of Lubricant Desorption and Decomposition under Heat Treatment: A Molecular Dynamics Study. *Soft Matter* **2013**, *9*, 700–708.

[64] Deb Nath, S. K. Thermal Decomposition and Desorption of PFPE Zdol on a DLC Substrate Using Quartic Bond Interaction Potential. *RSC Adv.* **2015**, *5*, 69651–69659.

[65] Lotfi, R.; Jonayat, A.; van Duin, A. C. T.; Biswas, M. M.; Hempstead, R. A Reactive Force Field Study on the Interaction of Lubricant with Diamond-Like Carbon Structures. *J. Phys. Chem. C* **2016**, *120*, 27443–27451.

[66] Ashurst, W. T.; Hoover, W. G. Dense-Fluid Shear Viscosity via Nonequilibrium Molecular Dynamics. *Phys. Rev. A* **1975**, *11*, 658–678.

[67] Ewen, J. P.; Heyes, D. M.; Dini, D. Advances in Nonequilibrium Molecular Dynamics Simulations of Lubricants and Additives. *Friction* **2018**, *6*, 349–386.

[68] Martini, A.; Eder, S. J.; Dörr, N. Tribochemistry: A Review of Reactive Molecular Dynamics Simulations. *Lubricants* **2020**, *8*, 44.

[69] Ding, J.; Zhang, L.; Zhang, Y.; Han, K. A Reactive Molecular Dynamics Study of N-Heptane Pyrolysis at High Temperature. *J. Phys. Chem. A* **2013**, *117*, 3266–3278.

[70] Khajeh, A.; He, X.; Yeon, J.; Kim, S. H.; Martini, A. Mechanochemical Association Reaction of Interfacial Molecules Driven by Shear. *Langmuir* **2018**, *34*, 5971–5977.

[71] Jacobs, T. D. B.; Gotsmann, B.; Lantz, M. A.; Carpick, R. W. On the Application of Transition State Theory to Atomic-Scale Wear. *Tribol. Lett.* **2010**, *39*, 257–271.

[72] Gosvami, N. N.; Bares, J. A.; Mangolini, F.; Konicek, A. R.; Yablon, D. G.; Carpick, R.

W. Mechanisms of Antiwear Tribofilm Growth Revealed in Situ by Single-Asperity Sliding Contacts. *Science* **2015**, *348*, 102–106.

[73]   Jacobs, T. D. B.; Carpick, R. W. Nanoscale Wear as a Stress-Assisted Chemical Reaction. *Nat. Nano.* **2013**, *8*, 108–112.

[74]   Vahdat, V.; Ryan, K. E.; Keating, P. L.; Jiang, Y.; Adiga, S. P.; Schall, J. D.; Turner, K. T.; Harrison, J. A.; Carpick, R. W. Atomic-Scale Wear of Amorphous Hydrogenated Carbon during Intermittent Contact: A Combined Study Using Experiment, Simulation, and Theory. *ACS Nano* **2014**, *8*, 7027–7040.

[75]   Wang, Y.; Shi, Y.; Sun, Q.; Lu, K.; Kubo, M.; Xu, J. Development of a Transferable ReaxFF Parameter Set for Carbon- and Silicon-Based Solid Systems. *J. Phys. Chem. C* **2020**, *124*, 10007–10015.

[76]   Islam, M. M.; Bryantsev, V. S.; van Duin, A. C. T. ReaxFF Reactive Force Field Simulations on the Influence of Teflon on Electrolyte Decomposition during Li/SWCNT Anode Discharge in Lithium-Sulfur Batteries. *J. Electrochem. Soc.* **2014**, *161*, E3009–E3014.

[77]   Frisch, M. J.; Trucks, G. W.; Schlegel, H. B.; Scuseria, G. E.; Robb, M. A.; Cheeseman, J. R.; Scalmani, G.; Barone, V.; Petersson, G. A.; Nakatsuji, H.; et al. Gaussian 16, Revision C.01, 2016.

[78]   Becke, A. D. A New Mixing of Hartree–Fock and Local Density-functional Theories. *J. Chem. Phys.* **1993**, *98*, 1372–1377.

[79]   Lee, C.; Yang, W.; Parr, R. G. Development of the Colle-Salvetti Correlation-Energy Formula into a Functional of the Electron Density. *Phys. Rev. B* **1988**, *37*, 785–789.

[80]   Hehre, W. J.; Ditchfield, R.; Pople, J. A. Self-Consistent Molecular Orbital Methods. XII. Further Extensions of Gaussian-Type Basis Sets for Use in Molecular Orbital Studies of Organic Molecules. *J. Chem. Phys.* **1972**, *56*, 2257–2261.

[81]   Hariharan, P. C.; Pople, J. A. The Influence of Polarization Functions on Molecular Orbital Hydrogenation Energies. *Theor. Chim. Acta* **1973**, *28*, 213–222.

[82]   Ditchfield, R.; Hehre, W. J.; Pople, J. A. Self-consistent Molecular-orbital Methods. IX. An Extended Gaussian-type Basis for Molecular-orbital Studies of Organic Molecules. *J. Chem. Phys.* **1971**, *54*, 724–728.

[83]   AMS. *SCM, Theoretical Chemistry, Vrije Universiteit, Amsterdam, The Netherlands*.

[84]   Yakata, K.; Kurafuji, H.; Tani, H.; Lu, R.; Koganezawa, S.; Kawada, S.; Tagawa, N. Effects of Oxygen on Smear Formation in Heat Assisted Magnetic Recording System. *Tribol. Online* **2022**, *17*, 348–355.

[85]   Sque, S. J.; Jones, R.; Briddon, P. R. Structure, Electronics, and Interaction of Hydrogen and Oxygen on Diamond Surfaces. *Phys. Rev. B* **2006**, *73*, 085313.

[86]   Voeltzel, N.; Fillot, N.; Vergne, P.; Joly, L. Orders of Magnitude Changes in the Friction

of an Ionic Liquid on Carbonaceous Surfaces. *J. Phys. Chem. C* **2018**, *122*, 2145–2154.

[87] Guo, L.; Chen, S.; Robbins, M. O. Effective Slip Boundary Conditions for Sinusoidally Corrugated Surfaces. *Phys. Rev. Fluids* **2016**, *1*, 074102.

[88] Kobayashi, T.; Zhang, H.; Fukuzawa, K.; Itoh, S. Coarse-Grained Molecular Dynamic Simulations of Nanometer-Thick Polar Lubricant Films Sheared Between Solid Surfaces With Random Roughness. *IEEE Trans. Magn.* **2015**, *51*, 1–4.

[89] Zhang, H.; Fukuda, M.; Washizu, H.; Kinjo, T.; Yoshida, H.; Fukuzawa, K.; Itoh, S. Shear Thinning Behavior of Nanometer-Thick Perfluoropolyether Films Confined between Corrugated Solid Surfaces: A Coarse-Grained Molecular Dynamics Study. *Tribol. Int.* **2016**, *93*, 163–171.

[90] Lu, R.; Zhang, H.; Mitsuya, Y.; Fukuzawa, K.; Itoh, S. Influence of Surface Roughness and Coating on the Friction Properties of Nanometer-Thick Liquid Lubricant Films. *Wear* **2014**, *319*, 56–61.

[91] Sun, H. Compass: An Ab Initio Force-Field Optimized for Condensed-Phase Applications-Overview with Details on Alkane and Benzene Compounds. *J. Phys. Chem. B* **1998**, *102*, 7338–7364.

[92] Plimpton, S. Fast Parallel Algorithms for Short-Range Molecular Dynamics. *J. Comput. Phys.* **1995**, *117*, 1–19.

[93] Nosé, S. A Molecular Dynamics Method for Simulations in the Canonical Ensemble. *Mol. Phys.* **1984**, *52*, 255–268.

[94] Hoover, W. G. Canonical Dynamics: Equilibrium Phase-Space Distributions. *Phys. Rev. A* **1985**, *31*, 1695–1697.

[95] Bernardi, S.; Todd, B. D.; Searles, D. J. Thermostating Highly Confined Fluids. *J. Chem. Phys.* **2010**, *132*, 244706.

[96] Ewen, J. P.; Spikes, H. A.; Dini, D. Contributions of Molecular Dynamics Simulations to Elastohydrodynamic Lubrication. *Tribol. Lett.* **2021**, *69*, 24.

[97] Ayestarán Latorre, C.; Remias, J. E.; Moore, J. D.; Spikes, H. A.; Dini, D.; Ewen, J. P. Mechanochemistry of Phosphate Esters Confined between Sliding Iron Surfaces. *Commun. Chem.* **2021**, *4*, 178.

[98] Ewen, J. P.; Gattinoni, C.; Thakkar, F. M.; Morgan, N.; Spikes, H. A.; Dini, D. A Comparison of Classical Force-Fields for Molecular Dynamics Simulations of Lubricants. *Materials* **2016**, *9*, 651.

[99] Guan, Y.; Lou, J.; Liu, R.; Ma, H.; Song, J. Reactive Molecular Dynamics Simulation on Thermal Decomposition of N-Heptane and Methylcyclohexane Initiated by Nitroethane. *Fuel* **2020**, *261*, 116447.

[100] Arrhenius, S. Über Die Reaktionsgeschwindigkeit Bei Der Inversion von Rohrzucker Durch Säuren. *Z. Phys. Chem.* **1889**, *4*, 226–248.

[101] Zhang, J.; Spikes, H. On the Mechanism of ZDDP Antiwear Film Formation. *Tribol. Lett.* **2016**, *63*, 24.

[102] Zhang, J.; Ewen, J. P.; Ueda, M.; Wong, J. S. S.; Spikes, H. A. Mechanochemistry of Zinc Dialkyldithiophosphate on Steel Surfaces under Elastohydrodynamic Lubrication Conditions. *ACS Appl. Mater. Interfaces* **2020**, *12*, 6662–6676.

[103] Yeon, J.; He, X.; Martini, A.; Kim, S. H. Mechanochemistry at Solid Surfaces: Polymerization of Adsorbed Molecules by Mechanical Shear at Tribological Interfaces. *ACS Appl. Mater. Interfaces* **2017**, *9*, 3142–3148.

[104] Nobrega, M. M.; Ceppatelli, M.; Temperini, M. L. A.; Bini, R. Pressure-Induced Reactivity in the Emeraldine Salt and Base Forms of Polyaniline Probed by FTIR and Raman. *J. Phys. Chem. C* **2014**, *118*, 27559–27566.

[105] Dai, Q.; Vurens, G.; Luna, M.; Salmeron, M. Lubricant Distribution on Hard Disk Surfaces: Effect of Humidity and Terminal Group Reactivity. *Langmuir* **1997**, *13*, 4401–4406.

[106] Chen, H.; Guo, Q.; Li, L.; Hsia, Y.-T.; Jhon, M. S. Humidity Effects on the Relaxation of Perfluoropolyether Lubricant Films. *IEEE Trans. Magn.* **2006**, *42*, 2531–2533.

[107] Min, B. G.; Choi, J. W.; Brown, H. R.; Yoon, D. Y.; O'Connor, T. M.; Jhon, M. S. Spreading Characteristics of Thin Liquid Films of Perfluoropolyalkylethers on Solid Surfaces. Effects of Chain-End Functionality and Humidity. *Tribol. Lett.* **1995**, *1*, 225–232.

[108] Karis, T. E. Water Adsorption on Thin Film Media. *J. Colloid Interface Sci.* **2000**, *225*, 196–203.

[109] Tyndall, G. W.; Waltman, R. J.; Pacansky, J. Effect of Adsorbed Water on Perfluoropolyether-Lubricated Magnetic Recording Disks. *J. Appl. Phys.* **2001**, *90*, 6287–6296.

[110] Kasai, P. H.; Raman, V. Lubricant Transfer in Disk Drives. *Tribol. Lett.* **2012**, *48*, 367–374.

[111] Kim, S. H.; Dai, Q.; Marchon, B.; Flechsig, K. Humidity Effects on Lubricant Transfer in the Head-Disk Interface of a Hard Disk Drive. *J. Appl. Phys.* **2009**, *105*, 07B704.

[112] Ma, Y.; Liu, B. Contribution of Water Vapor to Slider Air-Bearing Pressure in Hard Disk Drives. *Appl. Phys. Lett.* **2007**, *90*, 223502.

[113] Ma, Y.; Zhou, W.; Yu, S.; Hua, W. Adsorbed Water Film and Heat Conduction from Disk to Slider in Heat-Assisted Magnetic Recording. *Tribol. Lett.* **2014**, *56*, 93–99.

[114] Kasai, P. H.; Raman, V. Z-Dol Versus Z-Tetraol: Bonding and Durability in Magnetic Hard Disk Application. *Tribol. Lett.* **2004**, *16*, 29–36.

[115] Martínez, L.; Andrade, R.; Birgin, E. G.; Martínez, J. M. PACKMOL: A Package for Building Initial Configurations for Molecular Dynamics Simulations. *J. Comput. Chem.*

2009, *30*, 2157–2164.

[116] Jewett, A. I.; Stelter, D.; Lambert, J.; Saladi, S. M.; Roscioni, O. M.; Ricci, M.; Autin, L.; Maritan, M.; Bashusqeh, S. M.; Keyes, T.; Dame, R. T.; Shea, J.-E.; Jensen, G. J.; Goodsell, D. S. Moltemplate: A Tool for Coarse-Grained Modeling of Complex Biological Matter and Soft Condensed Matter Physics. *J. Mol. Biol.* **2021**, *433*, 166841.

[117] Stukowski, A. Visualization and Analysis of Atomistic Simulation Data with OVITO– the Open Visualization Tool. *Modell. Simul. Mater. Sci. Eng.* **2010**, *18*, 015012.

[118] Kasai, P. H.; Raman, V. Hydrogen Bonding in Lubricants for Hard Disk Drives. *Tribol. Lett.* **2006**, *21*, 205–216.

[119] Desanker, M.; He, X.; Lu, J.; Liu, P.; Pickens, D. B.; Delferro, M.; Marks, T. J.; Chung, Y.-W.; Wang, Q. J. Alkyl-Cyclens as Effective Sulfur- and Phosphorus-Free Friction Modifiers for Boundary Lubrication. *ACS Appl. Mater. Interfaces* **2017**, *9*, 9118–9125.

[120] Desanker, M.; He, X.; Lu, J.; Johnson, B. A.; Liu, Z.; Delferro, M.; Ren, N.; Lockwood, F. E.; Greco, A.; Erdemir, A.; Marks, T. J.; Wang, Q. J.; Chung, Y.-W. High-Performance Heterocyclic Friction Modifiers for Boundary Lubrication. *Tribol. Lett.* **2018**, *66*, 50.

[121] Gattinoni, C.; Ewen, J. P.; Dini, D. Adsorption of Surfactants on α-Fe$_2$O$_3$(0001): A Density Functional Theory Study. *J. Phys. Chem. C* **2018**, *122*, 20817–20826.

[122] Davidson, J. E.; Hinchley, S. L.; Harris, S. G.; Parkin, A.; Parsons, S.; Tasker, P. A. Molecular Dynamics Simulations to Aid the Rational Design of Organic Friction Modifiers. *J. Mol. Graphics Modell.* **2006**, *25*, 495–506.

[123] Hirayama, T.; Maeda, M.; Sasaki, Y.; Matsuoka, T.; Komiya, H.; Hino, M. Growth of Adsorbed Additive Layer for Further Friction Reduction. *Lubr. Sci.* **2019**, *31*, 171–178.

[124] Fry, B. M.; Moody, G.; Spikes, H. A.; Wong, J. S. S. Adsorption of Organic Friction Modifier Additives. *Langmuir* **2020**, *36*, 1147–1155.

[125] Doig, M.; Warrens, C. P.; Camp, P. J. Structure and Friction of Stearic Acid and Oleic Acid Films Adsorbed on Iron Oxide Surfaces in Squalane. *Langmuir* **2014**, *30*, 186–195.

[126] Ewen, J. P.; Kannam, S. K.; Todd, B. D.; Dini, D. Slip of Alkanes Confined between Surfactant Monolayers Adsorbed on Solid Surfaces. *Langmuir* **2018**, *34*, 3864–3873.

[127] Lee, S.; Shon, Y.-S.; Colorado, R.; Guenard, R. L.; Lee, T. R.; Perry, S. S. The Influence of Packing Densities and Surface Order on the Frictional Properties of Alkanethiol Self-Assembled Monolayers (SAMs) on Gold: A Comparison of SAMs Derived from Normal and Spiroalkanedithiols. *Langmuir* **2000**, *16*, 2220–2224.

[128] Wood, M. H.; Casford, M. T.; Steitz, R.; Zarbakhsh, A.; Welbourn, R. J. L.; Clarke, S. M. Comparative Adsorption of Saturated and Unsaturated Fatty Acids at the Iron Oxide/Oil Interface. *Langmuir* **2016**, *32*, 534–540.

[129] Nalam, P. C.; Pham, A.; Castillo, R. V.; Espinosa-Marzal, R. M. Adsorption Behavior and Nanotribology of Amine-Based Friction Modifiers on Steel Surfaces. *J. Phys. Chem. C* **2019**, *123*, 13672–13680.

[130] Bradley-Shaw, J. L.; Camp, P. J.; Dowding, P. J.; Lewtas, K. Molecular Dynamics Simulations of Glycerol Monooleate Confined between Mica Surfaces. *Langmuir* **2016**, *32*, 7707–7718.

[131] Castle, R. C.; Bovington, C. H. The Behaviour of Friction Modifiers under Boundary and Mixed EHD Conditions. *Lubr. Sci.* **2003**, *15*, 253–263.

[132] Loehlé, S.; Matta, C.; Minfray, C.; Le Mogne, T.; Iovine, R.; Obara, Y.; Miyamoto, A.; Martin, J. M. Mixed Lubrication of Steel by C18 Fatty Acids Revisited. Part II: Influence of Some Key Parameters. *Tribol. Int.* **2016**, *94*, 207–216.

[133] Jaishankar, A.; Jusufi, A.; Vreeland, J. L.; Deighton, S.; Pellettiere, J.; Schilowitz, A. M. Adsorption of Stearic Acid at the Iron Oxide/Oil Interface: Theory, Experiments, and Modeling. *Langmuir* **2019**, *35*, 2033–2046.

[134] Askwith, T. C.; Cameron, A.; Crouch, R. F.; Saunders, O. A. Chain Length of Additives in Relation to Lubricants in Thin Film and Boundary Lubrication. *Proc. R. Soc. London, Ser. A* **1966**, *291*, 500–519.

[135] Konishi, M.; Washizu, H. Understanding the Effect of the Base Oil on the Physical Adsorption Process of Organic Additives Using Molecular Dynamics. *Tribol. Int.* **2020**, *149*, 105568.

[136] Acero, P. N.; Mohr, S.; Bernabei, M.; Fernández, C.; Domínguez, B.; Ewen, J. P. Molecular Simulations of Surfactant Adsorption on Iron Oxide from Hydrocarbon Solvents. *Langmuir* **2021**, *37*, 14582–14596.

[137] Cyriac, F.; Yi, T. X.; Poornachary, S. K.; Chow, P. S. Influence of Base Oil Polarity on the Tribological Performance of Surface-Active Engine Oil Additives. *Tribol. Lett.* **2021**, *69*, 87.

[138] Zhang, X.; Tsukamoto, M.; Zhang, H.; Mitsuya, Y.; Itoh, S.; Fukuzawa, K. Experimental Study of Application of Molecules with a Cyclic Head Group Containing a Free Radical as Organic Friction Modifiers. *J. Adv. Mech. Des. Syst.* **2020**, *14*, JAMDSM0044.

[139] Hou, J.; Tsukamoto, M.; Hor, S.; Chen, X.; Yang, J.; Zhang, H.; Koga, N.; Yasuda, K.; Fukuzawa, K.; Itoh, S.; Azuma, N. Molecules with a TEMPO-Based Head Group as High-Performance Organic Friction Modifiers. *Friction* **2023**, *11*, 316–332.

[140] Lahtela, M.; Pakkanen, T. A.; Nissfolk, F. Molecular Modeling of Poly-α-Olefin Synthetic Oils. *J. Phys. Chem.* **1995**, *99*, 10267–10271.

[141] Zolper, T.; Li, Z.; Chen, C.; Jungk, M.; Marks, T.; Chung, Y.-W.; Wang, Q. Lubrication Properties of Polyalphaolefin and Polysiloxane Lubricants: Molecular Structure–Tribology Relationships. *Tribol. Lett.* **2012**, *48*, 355–365.

[142] Parkinson, G. S. Iron Oxide Surfaces. *Surf. Sci. Rep.* **2016**, *71*, 272–365.

[143] Dwivedi, D.; Lepková, K.; Becker, T. Carbon Steel Corrosion: A Review of Key Surface Properties and Characterization Methods. *RSC Adv.* **2017**, *7*, 4580–4610.

[144] Washizu, H.; Ohmori, T. Molecular Dynamics Simulations of Elastohydrodynamic Lubrication Oil Film. *Lubr. Sci.* **2010**, *22*, 323–340.

[145] Washizu, H.; Ohmori, T.; Suzuki, A. Molecular Origin of Limiting Shear Stress of Elastohydrodynamic Lubrication Oil Film Studied by Molecular Dynamics. *Chem. Phys. Lett.* **2017**, *678*, 1–4.

[146] Lu, T.; Chen, F. Multiwfn: A Multifunctional Wavefunction Analyzer. *J. Comput. Chem.* **2012**, *33*, 580–592.

[147] Lu, T.; Chen, F. Quantitative Analysis of Molecular Surface Based on Improved Marching Tetrahedra Algorithm. *J. Mol. Graphics Modell.* **2012**, *38*, 314–323.

[148] dihedral_style class2, https://docs.lammps.org/dihedral_class2.html (accessed 2021-09-26).

[149] Kresse, G.; Hafner, J. Ab Initio Molecular Dynamics for Liquid Metals. *Phys. Rev. B* **1993**, *47*, 558.

[150] Kresse, G.; Hafner, J. Ab Initio Molecular-Dynamics Simulation of the Liquid-Metal-Amorphous-Semiconductor Transition in Germanium. *Phys. Rev. B* **1994**, *49*, 14251–14269.

[151] Kresse, G.; Furthmüller, J. Efficiency of Ab-Initio Total Energy Calculations for Metals and Semiconductors Using a Plane-Wave Basis Set. *Comput. Mater. Sci.* **1996**, *6*, 15–50.

[152] Kresse, G.; Furthmüller, J. Efficient Iterative Schemes for Ab Initio Total-Energy Calculations Using a Plane-Wave Basis Set. *Phys. Rev. B* **1996**, *54*, 11169–11186.

[153] Finger, L. W.; Hazen, R. M. Crystal Structure and Isothermal Compression of Fe_2O_3, Cr_2O_3, and V_2O_3 to 50 Kbars. *J. Appl. Phys.* **1980**, *51*, 5362–5367.

[154] Dudarev, S. L.; Botton, G. A.; Savrasov, S. Y.; Humphreys, C. J.; Sutton, A. P. Electron-Energy-Loss Spectra and the Structural Stability of Nickel Oxide: An LSDA+U Study. *Phys. Rev. B* **1998**, *57*, 1505–1509.

[155] Al-Kuhaili, M. F.; Saleem, M.; Durrani, S. M. A. Optical Properties of Iron Oxide (α-Fe_2O_3) Thin Films Deposited by the Reactive Evaporation of Iron. *J. Alloys Compd.* **2012**, *521*, 178–182.

[156] Huang, Y.; Zhao, K.; Liu, Y.; Zhang, X.; Du, H.; Ren, X. Investigation on Adsorption of Ar and N_2 on α-Al_2O_3(0001) Surface from First-Principles Calculations. *Vacuum* **2020**, *176*, 109344.

[157] Latorre, C. A.; Ewen, J. P.; Gattinoni, C.; Dini, D. Simulating Surfactant–Iron Oxide Interfaces: From Density Functional Theory to Molecular Dynamics. *J. Phys. Chem. B*

2019, *123*, 6870–6881.

[158]   Hardy, W. B.; Doubleday, I. Boundary Lubrication. – The Paraffin Series. *Proc. R. Soc. London, Ser. A* **1922**, *100*, 550–574.

[159]   Porter, M. D.; Bright, T. B.; Allara, D. L.; Chidsey, C. E. D. Spontaneously Organized Molecular Assemblies. 4. Structural Characterization of n-Alkyl Thiol Monolayers on Gold by Optical Ellipsometry, Infrared Spectroscopy, and Electrochemistry. *J. Am. Chem. Soc.* **1987**, *109*, 3559–3568.

[160]   Lio, A.; Charych, D. H.; Salmeron, M. Comparative Atomic Force Microscopy Study of the Chain Length Dependence of Frictional Properties of Alkanethiols on Gold and Alkylsilanes on Mica. *J. Phys. Chem. B* **1997**, *101*, 3800–3805.

[161]   Ewen, J. P.; Echeverri Restrepo, S.; Morgan, N.; Dini, D. Nonequilibrium Molecular Dynamics Simulations of Stearic Acid Adsorbed on Iron Surfaces with Nanoscale Roughness. *Tribol. Int.* **2017**, *107*, 264–273.

[162]   Alexander, A. E.; Rideal, E. K. The Role of Hydrogen Bonds in Condensed Monolayers. *Proc. R. Soc. London, Ser. A* **1942**, *179*, 470–485.

Appendix: Results for Different Temperatures and C_{12}TEMPO Concentrations for Chapter 4

A.1. Snapshots at the Final State
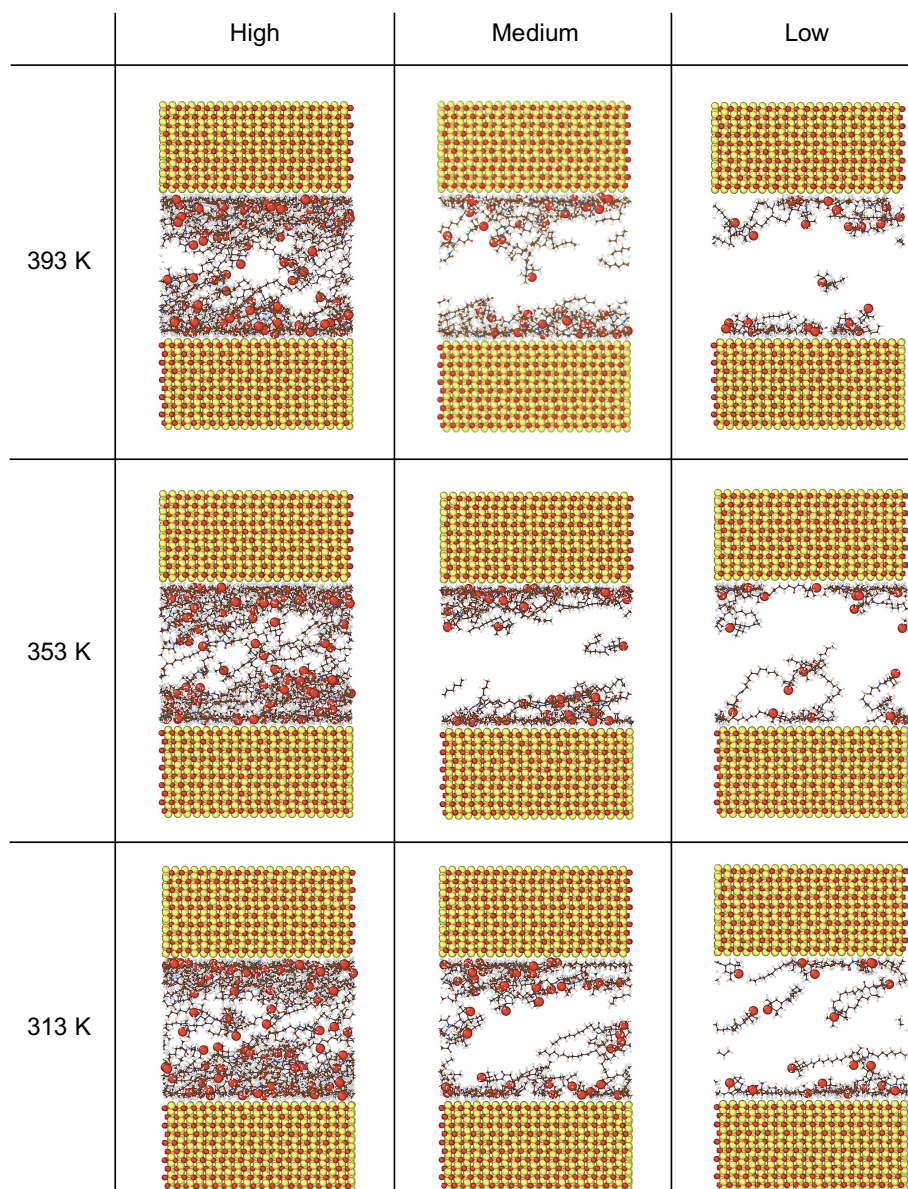
Figure A-1 Front-view snapshots at the final timestep for different temperatures and C_{12}TEMPO concentrations. For easy observation of the structure of the boundary films, only the iron oxide substrates and C_{12}TEMPO molecules are shown. The large red spheres represent the terminal O• atom of C_{12}TEMPO.

A.2. Number Density Profiles of O• Atoms
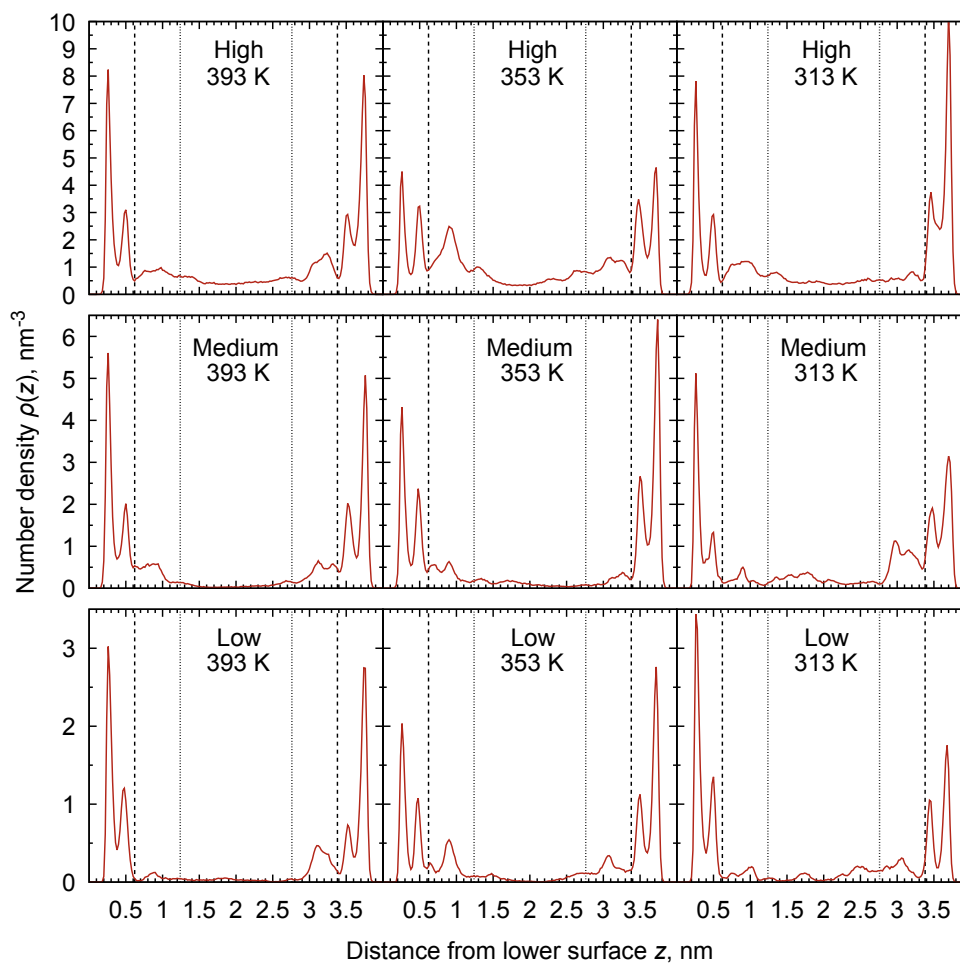
Figure A-2 Number density profiles of O• atoms in $C_{12}TEMPO$ molecules for different temperatures and $C_{12}TEMPO$ concentrations. Broken and dotted lines indicate the boundaries of the first and second layers, respectively. Note that the scale of the vertical axis is different depending on the concentration.

A.3. Number Density Profiles of O_{amide} Atoms
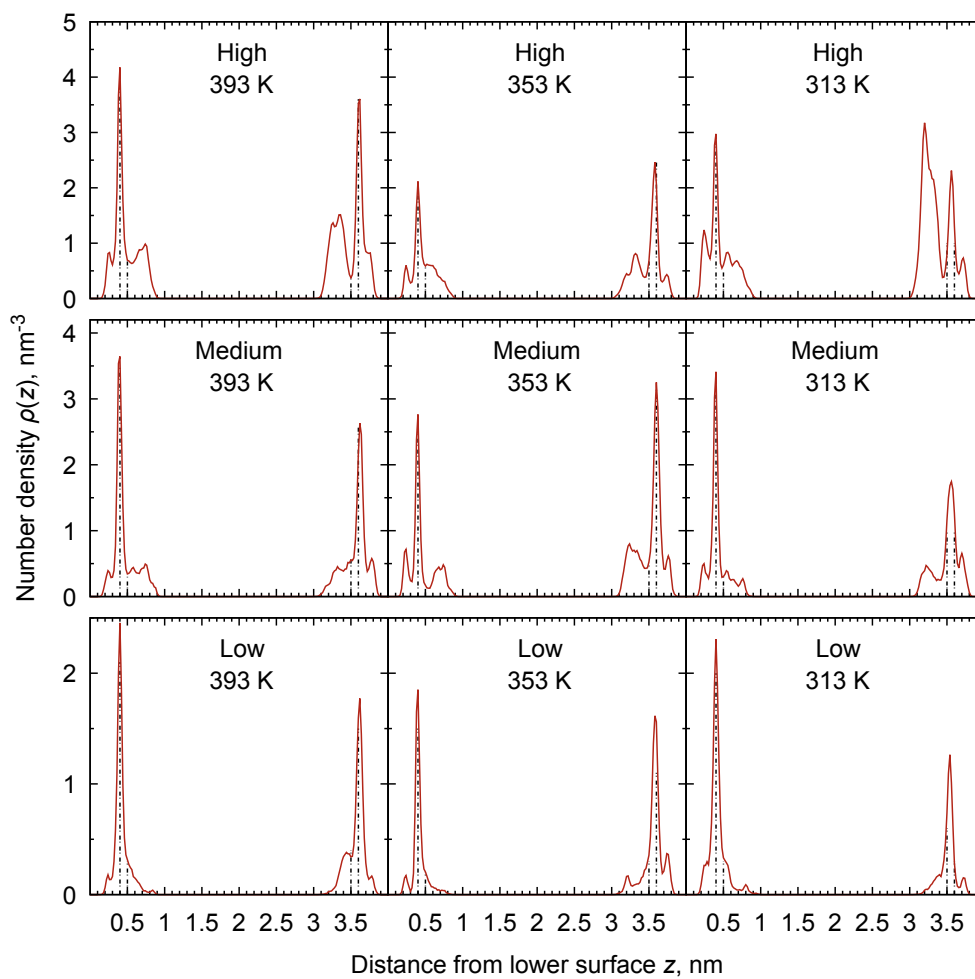
Figure A-3 Number density profiles of O_{amide} atoms in $C_{12}TEMPO$ molecules with strongly adsorbed O•
atoms for different temperatures and $C_{12}TEMPO$ concentrations. Note that the scale of the vertical axis
is different depending on the concentration.
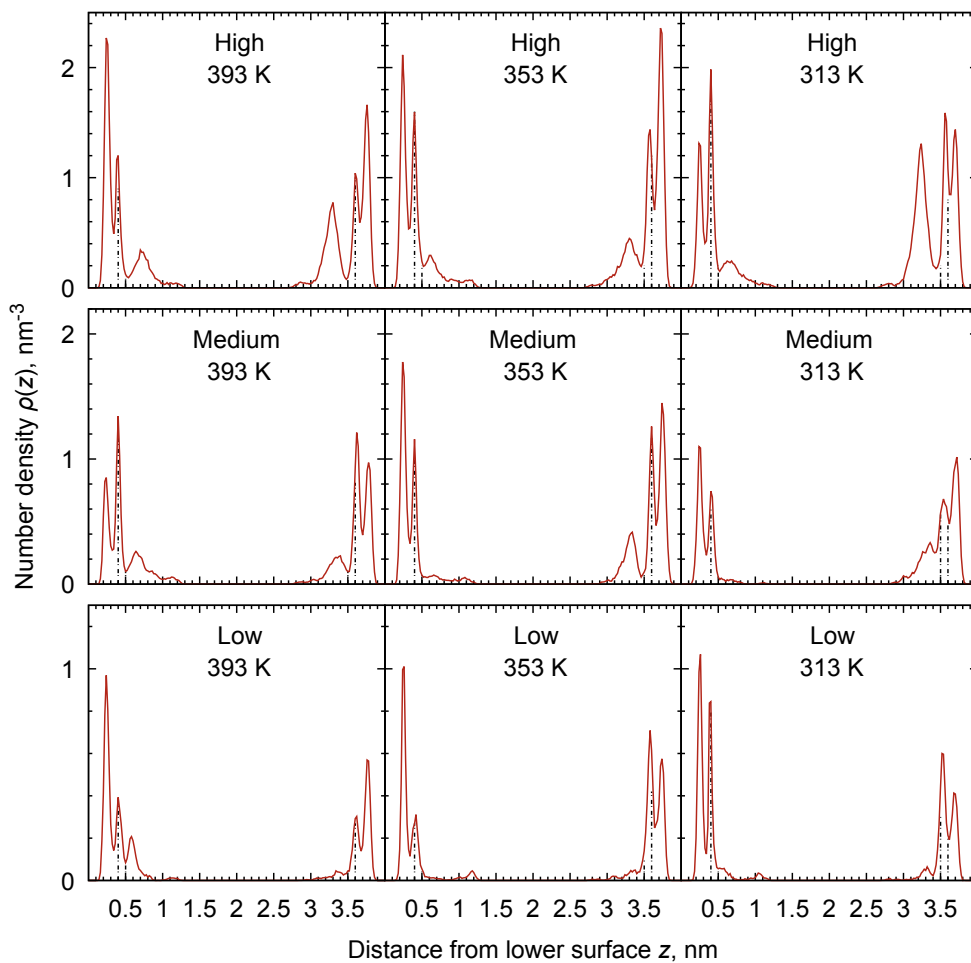
Figure A-4 Number density profiles of O_{amide} atoms in $C_{12}TEMPO$ molecules with weakly adsorbed $O\bullet$ atoms for different temperatures and $C_{12}TEMPO$ concentrations. Note that the scale of the vertical axis is different depending on the concentration.

A.4. Probability of Occurrence for Different Adsorption States in the First Layer
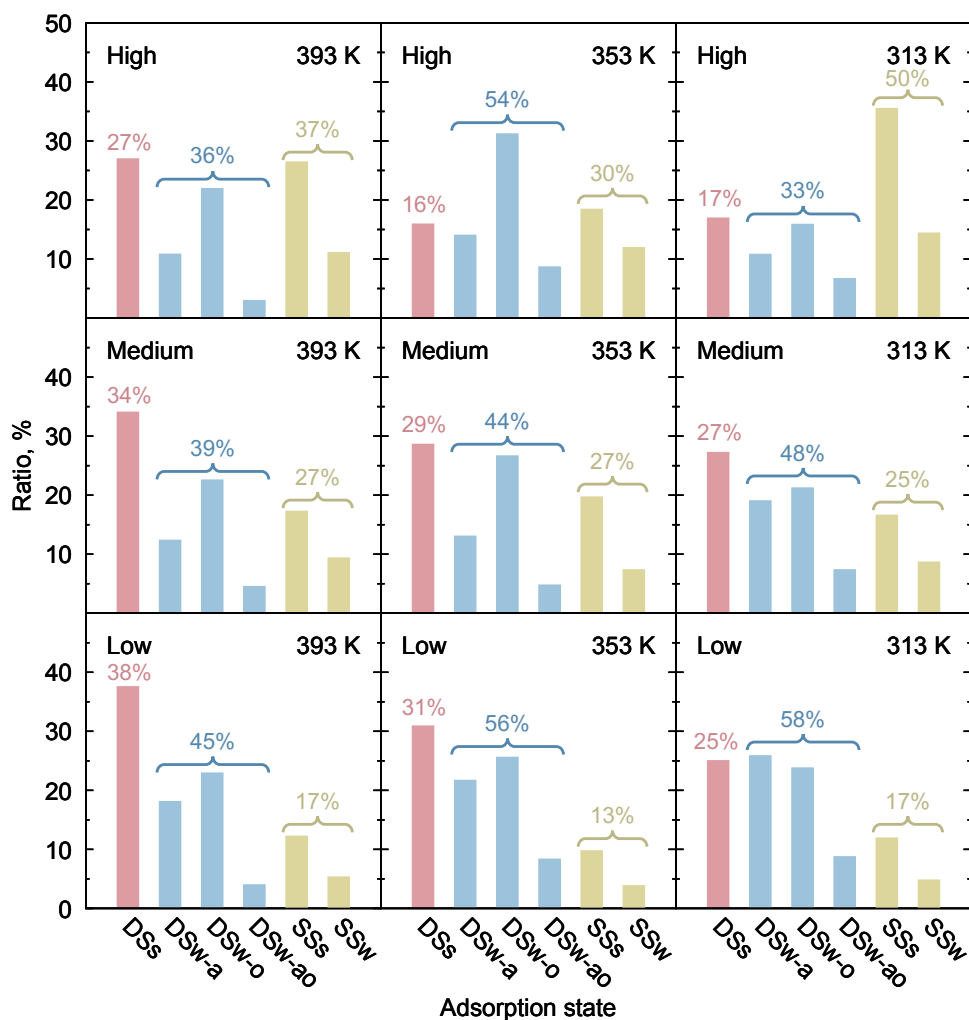
Figure A-5 Probability of occurrence of different adsorption states for C_{12}TEMPO in the first layer for different temperatures and C_{12}TEMPO concentrations.

A.5. Ratios of Interlayer and Intralayer Hydrogen-Bonded Molecules
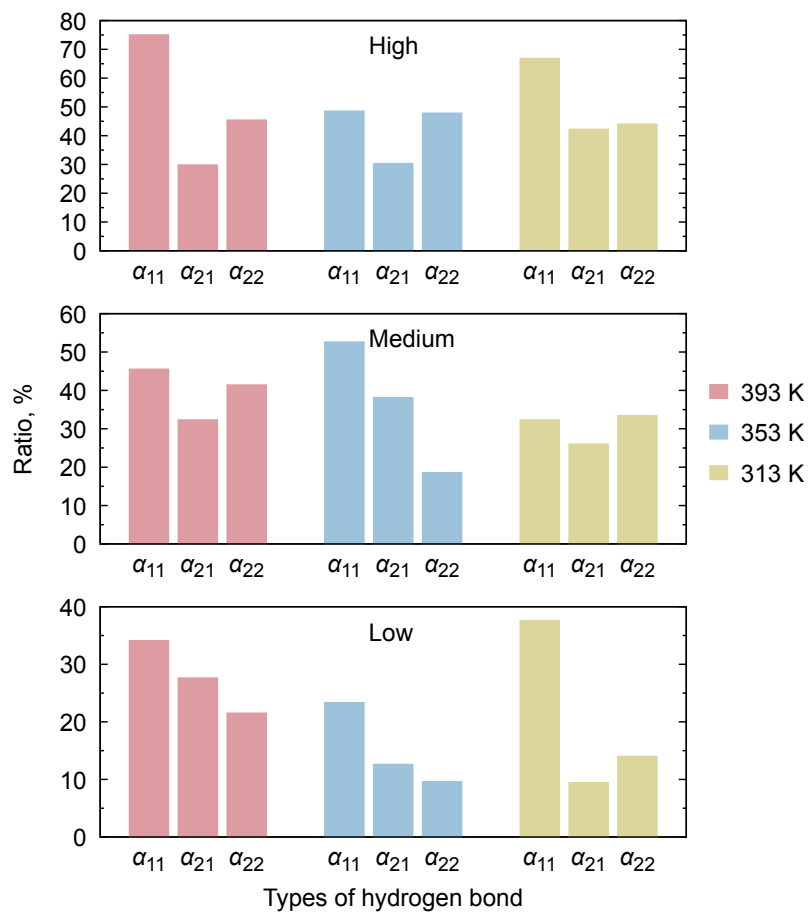
Figure A-6 Ratios of molecules forming interlayer (α_{21}) and intralayer (α_{11}, α_{22}) hydrogen bonds for different temperatures and C_{12}TEMPO concentrations.

A.6. Ratios of Two Types of Stable Adsorption
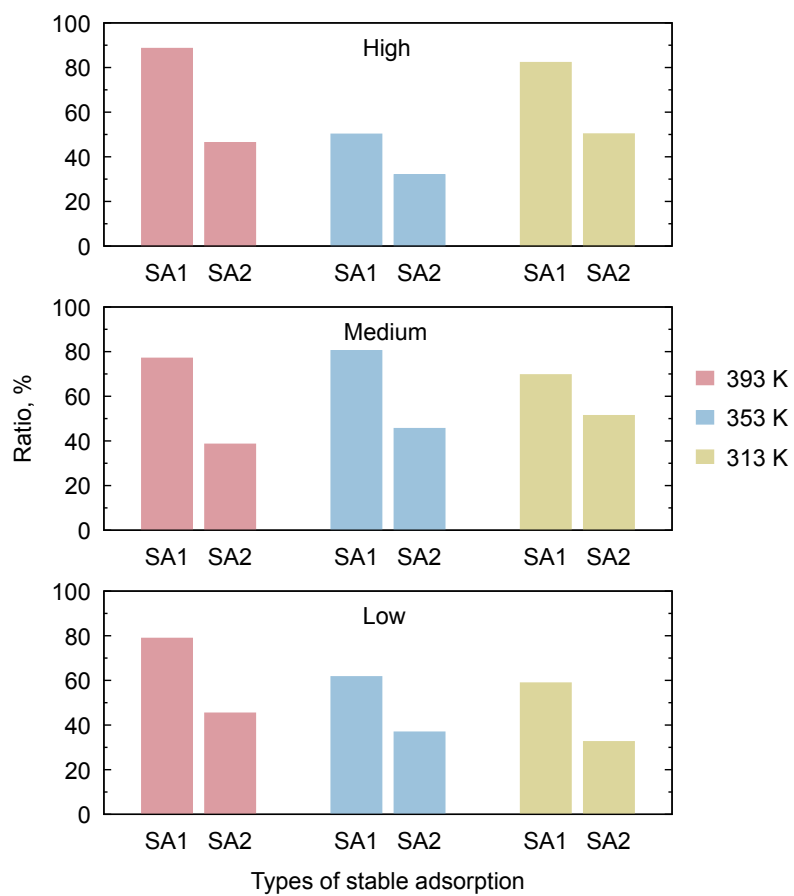
Figure A-7 Ratios of two types of stable adsorption for different temperatures and C_{12}TEMPO concentrations.

A.7. Velocity Profiles
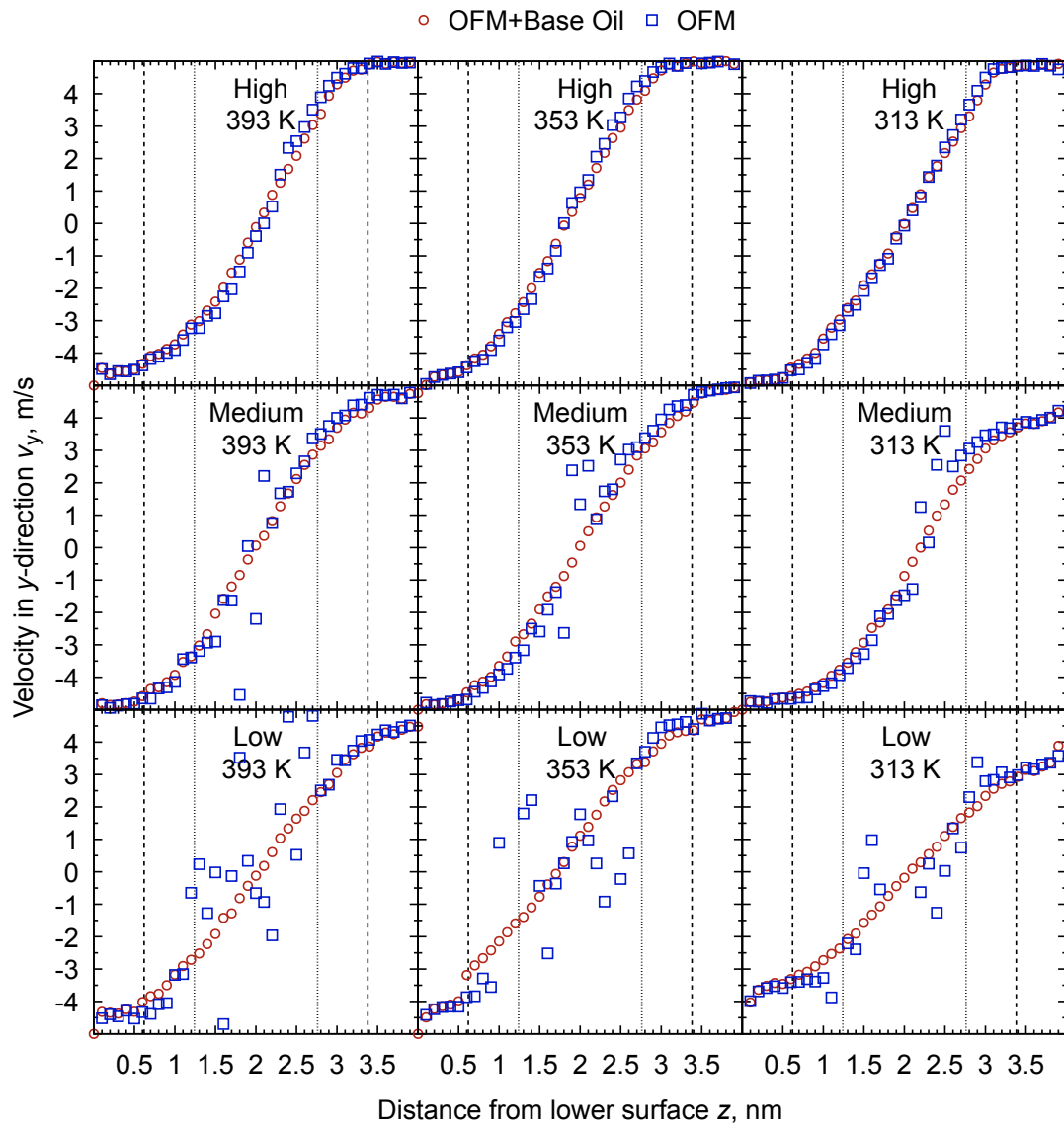
Figure A-8 Velocity profiles for different temperatures and C_{12}TEMPO concentrations. Broken and dotted lines indicate the boundaries of the first and second layers, respectively.

Publication List

Journal Paper

[1] **Xingyu Chen**, Koya Inayoshi, Hedong Zhang, Nobuaki Koga, Kenji Fukuzawa, Shintaro Itoh, Naoki Azuma. Effect of water on mechano-chemical reactions of perfluoropolyether lubricant films in heat-assisted magnetic recording: a reactive molecular dynamics study, *Tribology International*, 2023, 187: 108674. DOI: 10.1016/j.triboint.2023.108674.

[2] **Xingyu Chen**, Juntao Yang, Koji Yasuda, Nobuaki Koga, Hedong Zhang. Adsorption behavior of TEMPO-based organic friction modifiers during sliding between iron oxide surfaces: a molecular dynamics study, *Langmuir*, 2022, 38(10): 3170–3179. DOI: 10.1021/acs.langmuir.1c03203.

[3] **Xingyu Chen**, Kento Kawai, Hedong Zhang, Kenji Fukuzawa, Nobuaki Koga, Shintaro Itoh, Naoki Azuma. Reaxff reactive molecular dynamics simulations of mechano-chemical decomposition of perfluoropolyether lubricants in heat-assisted magnetic recording, *The Journal of Physical Chemistry C*, 2020, 124(41): 22496–22505. DOI: 10.1021/acs.jpcc.0c06486.

Conference Paper

[1] **Xingyu Chen**, Koya Inayoshi, Hedong Zhang, Kenji Fukuzawa, Shintaro Itoh, Naoki Azuma. Effect of water on mechanochemical reactions of PFPE lubricant films: a reactive molecular dynamics study. *2023 JSME Information, Intelligence and Precision Equipment Division (IIP2023)*, IIPA-1-10, 2023.3.6-7, Kyushu Institute of Technology, Japan.
陳 星宇, 稲吉 宏哉, 張 賀東, 福澤 健二, 伊藤 伸太郎, 東 直輝. PFPE 潤滑膜のメカノケミカル反応に及ぼす水の影響に関する反応分子動力学解析. IIP2023 情報・知能・精密機器部門(IIP 部門)講演会, IIPA-1-10, 2023.3.6-7, 九州工業大学.

[2] **Xingyu Chen**, Juntao Yang, Koji Yasuda, Nobuaki Koga, Hedong Zhang. Molecular dynamics study of adsorption behavior of TEMPO-based organic friction modifiers on iron oxide surfaces. *Tribology Conference 2022 Spring in Tokyo*, C13, 2022.5.23-25, online.
陳 星宇, 楊 俊韜, 安田 耕二, 古賀 伸明, 張 賀東. TEMPO 系有機摩擦調整剤の酸化鉄表面への吸着挙動に関する分子動力学解析. トライボロジー会議 2022 春 東京, C13, 2022.5.23-25, オンライン.

[3] Juntao Yang, **Xingyu Chen**, Koji Yasuda, Hedong Zhang, Kenji Fukuzawa. Adsorption of organic friction modifiers with a cyclic structure and radical onto iron oxide surfaces: a quantum mechanical and molecular dynamics study. *Tribology Conference 2021 Spring in Tokyo*, E16, 2021.5.24-26, online.
楊 俊韜, 陳 星宇, 安田 耕二, 張 賀東, 福澤 健二. 環状構造とラジカルをもつ有機摩擦調整剤の酸化鉄表面への吸着：量子力学計算と分子動力学解析. トライボロジー会議

2021 春 東京, E16, 2021.5.24-26, オンライン.

[4] **Xingyu Chen**, Hedong Zhang, Kenji Fukuzawa, Shintaro Itoh, Naoki Azuma. Reactive molecular dynamics study of thermal decomposition and transfer of perfluoropolyether lubricant in heat-assisted magnetic recording. *Mechanical Engineering Congress, 2020*, S16102, 2020.9.13-16, online.
陳 星宇, 張 賀東, 福澤 健二, 伊藤 伸太郎, 東 直輝. 反応分子動力学による熱アシスト磁気記録における PFPE 潤滑膜の熱分解と移着の解析. 日本機械学会 2020 年度年次大会, S16102, 2020.9.13-16, オンライン.

[5] **Xingyu Chen**, Kento Kawai, Hedong Zhang, Kenji Fukuzawa, Shintaro Itoh, Naoki Azuma. Reactive molecular dynamics study of mechano-chemical decomposition of perfluoropolyether lubricants in heat assisted magnetic recording. *Conference on Information, Intelligence, and Precision Equipment 2020*, 1A06, 2020.3.26-27, online.
陳 星宇, 川合 健斗, 張 賀東, 福澤 健二, 伊藤 伸太郎, 東 直輝. 反応分子動力学による熱アシスト磁気記録における PFPE 潤滑膜のメカノケミカル分解解析. IIP2020 情報・知能・精密機器部門(IIP 部門)講演会, 1A06, 2020.3.26-27, オンライン.

Acknowledgements